

RESEARCH ARTICLE

ENERGY HARVESTING

Harvesting electrical energy from carbon nanotube yarn twist

Shi Hyeong Kim,^{1,2*} Carter S. Haines,^{2*} Na Li,^{2*} Keon Jung Kim,¹ Tae Jin Mun,¹ Changsoon Choi,¹ Jiangtao Di,² Young Jun Oh,³ Juan Pablo Oviedo,³ Julia Bykova,⁴ Shaoli Fang,² Nan Jiang,⁵ Zunfeng Liu,^{5,6} Run Wang,^{5,6} Prashant Kumar,⁷ Rui Qiao,⁷ Shashank Priya,⁷ Kyeongjae Cho,³ Moon Kim,³ Matthew Steven Lucas,⁸ Lawrence F. Drummy,⁸ Benji Maruyama,⁸ Dong Youn Lee,¹ Xavier Lepro,² Enlai Gao,² Dawood Albarq,² Raquel Ovalle-Robles,⁴ Seon Jeong Kim,^{1†} Ray H. Baughman^{2†}

Mechanical energy harvesters are needed for diverse applications, including self-powered wireless sensors, structural and human health monitoring systems, and the extraction of energy from ocean waves. We report carbon nanotube yarn harvesters that electrochemically convert tensile or torsional mechanical energy into electrical energy without requiring an external bias voltage. Stretching coiled yarns generated 250 watts per kilogram of peak electrical power when cycled up to 30 hertz, as well as up to 41.2 joules per kilogram of electrical energy per mechanical cycle, when normalized to harvester yarn weight. These energy harvesters were used in the ocean to harvest wave energy, combined with thermally driven artificial muscles to convert temperature fluctuations to electrical energy, sewn into textiles for use as self-powered respiration sensors, and used to power a light-emitting diode and to charge a storage capacitor.

The importance of harvesting mechanical energy as electrical energy motivates the search for new technologies. Electromagnetic electric energy generators suffer from low power densities and high cost per watt when scaled to the millimeter and smaller dimensions needed for emerging applications (1). Piezoelectric and ferroelectric harvesters work well for high-frequency, low-strain deformations (2), especially when individual nanofibers are driven at ultrahigh resonant frequencies (3), but they lack the elasticity needed for harvesting large strains. Triboelectric harvesters (4, 5) perform well and are promising for future applications. Harvesters that use the coupling between flowing fluids and electronic charge are appealing (6–8) but need improvements in output power. Diverse electrochemical harvesters are known—including conducting polymer harvesters (9), lith-

ium battery-based bending harvesters (10), and ionic polymer-metal composite harvesters (11)—but have not yet provided competitive performance. The capacitance change caused by mechanically altering the area of liquid contact with two charged or self-charged capacitor electrodes has been used for dielectric (12) and electrochemical (13) energy harvesting, but these technologies are still in early development.

Rubber-based dielectric capacitors are attractive for converting large-stroke mechanical energy into electricity. A thin elastomeric sheet is sandwiched between two deformable electrodes (14, 15). An applied voltage (V), typically ~1000 V, is used to inject charge (Q) into this elastomeric capacitor. When stretched, the rubber dielectric decreases thickness, increasing capacitance (C) and thereby producing a voltage change according to $Q = CV$, which enables electrical energy generation.

To avoid these high voltages and associated circuits, we previously tried to manufacture a twisted carbon nanotube (CNT) yarn mechanical energy harvester that electrochemically generated electrical energy when stretched. However, even when volt-scale positive or negative bias voltages were applied, tensile stresses of up to 45 MPa resulted in such small short circuit currents that the only possible application was as an externally powered strain sensor (16).

Fabrication and performance of CNT yarn harvesters

We demonstrate CNT yarns that can be stretched to generate a peak electrical power of 250 W per kilogram of yarn, without needing an external bias voltage. This advance resulted in part from our

transitioning from CNT yarns that are twisted but not coiled to yarns that are so highly twisted that they completely coil, which we hereafter refer to as twisted and coiled yarns, respectively.

Harvesters were produced by spinning sheets of forest-drawn carbon multiwalled nanotubes (MWNTs) into high-strength yarns (17, 18). Due to large MWNT diameters, MWNT bundling, and the absence of pseudo-capacitive redox groups, these yarns have a capacitance of <15 F/g (19). By inserting extreme twist into a CNT yarn that supports a weight, coils initiate and propagate, producing a highly elastic, uniformly coiled structure. Figure 1A illustrates the spinning methods and resulting yarn topologies before the onset of coiling. Unless otherwise noted, the harvester yarns had a diameter of 50 to 70 μm when twisted to just before coiling and were made by the cone-spinning process depicted in Fig. 1A.

Figure 1B illustrates the electrochemical cell used for the initial characterization of harvester yarns; this cell comprises a coiled MWNT yarn working electrode, a high-surface-area counter electrode, and a reference electrode, all of which are immersed in aqueous electrolyte. Figure 1C shows the time dependence of open-circuit voltage (OCV) and short-circuit current (SCC) generated by a coiled cone-spun harvester during 1-Hz sinusoidal stretch to 30% strain in 0.1 M HCl electrolyte. This sinusoidal stretch does not produce sinusoidal variation in OCV or SCC if the applied tension is so low that the yarn is not in an extended configuration, because the input mechanical energy per change in strain (and corresponding output voltage and electrical energy change) is reduced by a low effective yarn stiffness. Because the voltage peaks most sharply when the yarn is fully stretched, peak power can exceed average power by an observed factor as high as 3.34, as compared with the factor of 2 expected for a purely sinusoidal voltage profile.

When stretched to 30% strain, the harvester's capacitance decreased 30.7%, and its OCV increased by 140 mV (Fig. 1D). Unless otherwise noted herein, the electrolyte is 0.1 M HCl, the reference electrode is Ag/AgCl, and the applied strain is sinusoidal. Applied tensile stresses are normalized to the cross-sectional area of the twisted, noncoiled yarn.

Harvester performance has been improved by using the hysteretic nature of twist insertion and removal (fig. S23): Untwisting a coiled yarn by a small amount does not result in coil loss but instead increases coil diameter and reduces twist-induced densification. As shown in Fig. 1, E and F, and fig. S6, untwisting by 500 turns/m (8.5% of the twist inserted to fully coil) increased the reversible tensile strain range from 30 to 50% and increased the tensile strain-induced capacitance change from 30 to 36%. The capacitance at 0% strain increased from 3.97 to 6.50 F/g, due to the reduced compressive forces and decreased yarn density resulting from twist removal. Most importantly, this twist removal increased peak power at 12 Hz by a factor of 1.4 (peak power increased to 179 W/kg, which is 30.97 μW for this 0.173-mg harvester) (fig. S11) and increased maximum output energy per cycle at 0.25 Hz

¹Center for Self-Powered Actuation, Department of Biomedical Engineering, Hanyang University, Seoul 04763, South Korea. ²Alan G. MacDiarmid NanoTech Institute, University of Texas at Dallas, Richardson, TX 75080, USA.

³Department of Materials Science and Engineering, University of Texas at Dallas, Richardson, TX 75080, USA.

⁴Linter of America, Nano-Science & Technology Center, Richardson, TX 75081, USA. ⁵Jiangnan Graphene Research Institute, Changzhou 213149, China. ⁶State Key Laboratory of Medicinal Chemical Biology, College of Pharmacy, Nankai University, Tianjin, 300071, China. ⁷Department of Mechanical Engineering, Virginia Polytechnic Institute and State University, Blacksburg, VA 24061, USA. ⁸Air Force Research Laboratory, Materials and Manufacturing Directorate, Wright-Patterson Air Force Base, Dayton, OH 45433, USA.

*These authors contributed equally to this work. †Corresponding author. Email: sjk@hanyang.ac.kr (S.J.K.); ray.baughman@utdallas.edu (R.H.B.)

by a factor of 2.9 (per-cycle energy increased to 41.2 J/kg, which is 7.13 μ J) (Fig. 1E). The existence of a long plateau in frequencies that maximize power (from 12 Hz to >25 Hz in Fig. 1E) provides a major advantage compared with resonant harvesters, whose power output rapidly degrades as mechanical deformation frequencies deviate from resonance (20).

The above performance was obtained for CNT yarn electrodes produced by a twist-insertion process called cone spinning; this process optimizes harvester performance. Unlike for conven-

tional “dual-Archimedean” yarn fabrication, in which twisting a rectangular stack of CNT sheets between fixed supports causes a gradient of tension along the sheet width (21), cone spinning (Fig. 1A and fig. S1) maintains quasi-uniform tension across the CNT array. This stress nonuniformity was avoided by rolling a CNT sheet stack about the CNT alignment direction to make a cylinder (22) and then twisting this cylinder around its central axis to produce two cones, which densify to a yarn. These quasi-uniformly twisted yarns produced roughly four

times the peak power and average power generated by dual-Archimedean yarns (Fig. 2A, table S1, and fig. S25). Similarly, methods such as tow spinning, funnel spinning, and Fermat spinning (Fig. 1A) (22) also reduced nonuniform tension during twisting and provided comparably high-performance yarns.

For a given inserted twist, the mechanical load applied during twisting determines the coil spring index (22), which affects harvester performance. The peak power and change in capacitance for a given percent strain are optimized for a spring index of ~0.43 (measured after coiling, with the coiling load still applied), which yielded a peak power of 41.3 W/kg for 30% strain at 1 Hz (fig. S2). However, as the spring index increases, the maximum reversible coil deformation increases (and the coil stiffness decreases), enabling energy harvesting over a larger strain range. This tunability allows the harvester to be customized for the stroke range needed for a particular application. Unless otherwise indicated, a spring index of ~0.43 was used for all experiments.

For potential use in harvesting the energy in ocean waves, CNT yarn harvesters were tested in 0.6 M NaCl, a concentration similar to that found in seawater. For 30% stretch and deformation frequencies of 0.25 to 12 Hz, a plateau in peak power (at ~94 W/kg) was observed above 6 Hz (fig. S10). As needed for ocean-wave harvesting, harvester performance in 0.6 M NaCl (and in 0.1 M HCl) varies little with temperature (figs. S13 and S24). Also, the peak power and the load resistance that optimizes peak power depend little on NaCl concentrations between 0.6 and 5 M, and the peak power decreases by less than 20% for concentrations down to 0.1 M (fig. S9), which means that these harvesters can be used for ocean environments of varying salinity. Figure 2B shows that the peak power and average power at 0°C (46.3 and 15.3 W/kg) were maintained for more than 30,000 cycles at 1 Hz to 30% strain in 0.6 M NaCl.

Important for many applications, gravimetric energy output per cycle is scale-invariant, as shown for coiled harvester yarns in fig. S7. The amount of inserted twist (T , in turns per meter) was scaled inversely with yarn diameter D to keep TD constant. This structural scaling automatically occurred because yarns were twisted under the same stress until fully coiled, and TD was scale-invariant for this degree of inserted twist. Likewise, the obtained spring index (presently 0.43) was scale-invariant. The per-cycle gravimetric energy, peak-to-peak OCV, and frequency dependence of gravimetric peak power were constant for yarn diameters between 40 and 110 μ m (fig. S7). Also, a similar peak power density was obtained at 1 Hz for a coiled yarn and a four-ply yarn made from this coiled yarn (fig. S18).

We call our devices “twistron” harvesters—“twist” denotes the harvester mechanism, and “tron” is the Greek suffix for device. The twist mechanism for energy harvesting by stretching a coiled yarn was first suggested by our observation that twisting a noncoiled yarn generated electrical

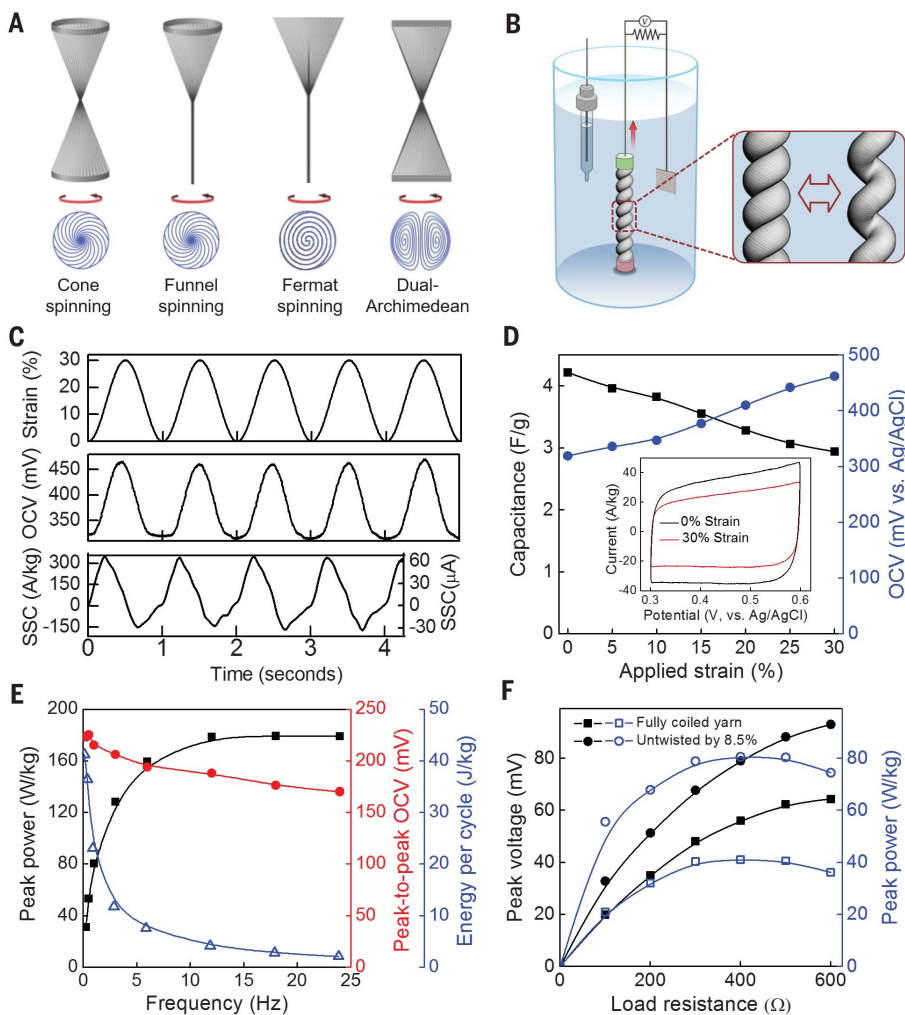


Fig. 1. Twistrion harvester configuration, structure, and performance for tensile energy harvesting in 0.1 M HCl. (A) Illustrations of cone, funnel, Fermat, and dual-Archimedean spinning (top) and resulting yarn cross sections (bottom). (B) Illustration of a torsionally tethered coiled harvester electrode and counter and reference electrodes in an electrochemical bath, showing the coiled yarn before and after stretch. (C) Sinusoidal applied tensile strain and resulting change in open-circuit voltage (OCV) and short-circuit current (SCC) before (right) and after (left) normalization for a cone-spun coiled harvester. (D) Capacitance and OCV versus applied strain for the harvester of (C). (Inset) Cyclic voltammetry curves for 0 and 30% strain. (E) Frequency dependence of peak power (solid black squares), peak-to-peak OCV (solid red circles), and energy per cycle (open blue triangles) for 50% stretch of an 8.5%-untwisted coiled harvester. The output electrical power from this 0.173-mg twistrion harvester electrode is 31.0 μ W above 10 Hz. (F) Generated peak power (solid black symbols) and peak voltage (open blue symbols) versus load resistance for a coiled yarn (squares) and a partially untwisted coiled yarn (circles) when stretched at 1 Hz to the maximum reversible elongation.

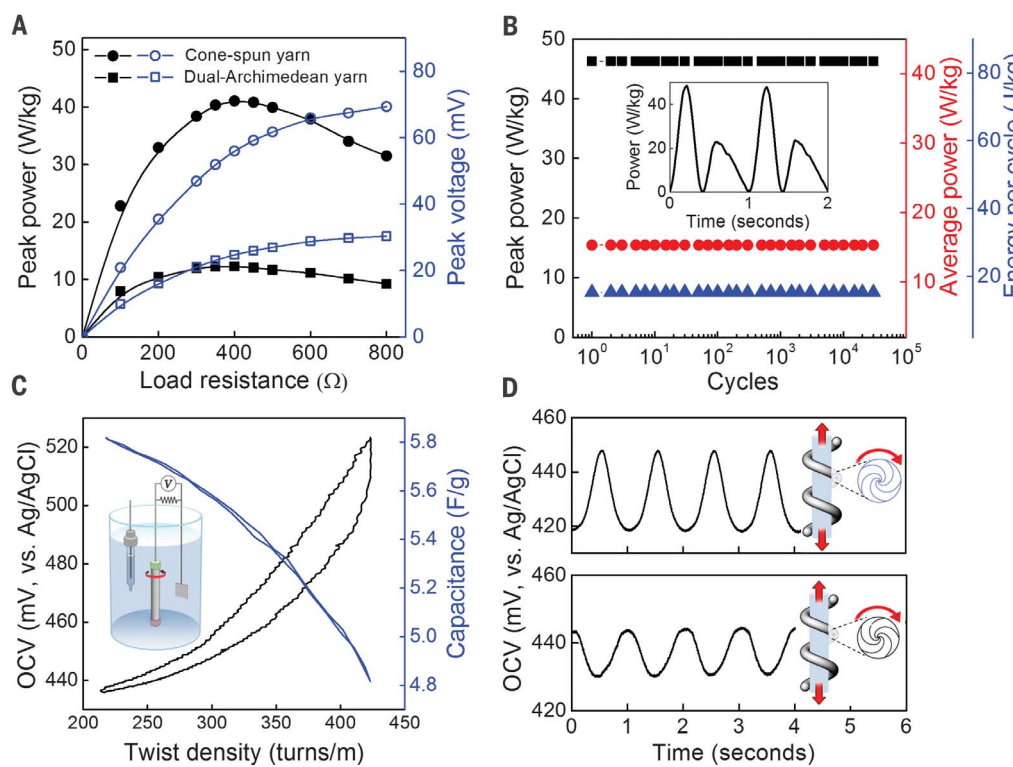


Fig. 2. Torsional and tensile performance of twistron harvesters. (A) Peak power (solid black symbols) and peak voltage (open blue symbols) versus load resistance for a 1-Hz stretch to 30% strain for the coiled harvester of Fig. 1C and for an otherwise identical dual-Archimedean-spun harvester. (B) Peak power, average power, and electrical energy per cycle during 30,000 stretch-and-release cycles to 30% strain at 1 Hz for the above twistron yarn in 0°C 0.6 M NaCl. (Inset) Output power versus time during typical cycles. (C) Dependence of capacitance and voltage on isometric twist and untwist for a noncoiled, 47-mm-long, 360-μm-diameter yarn in 0.1 M HCl. (Inset) Experimental apparatus. (D) OCV versus time during 60% stretch in 0.1 M HCl for homochiral (top) and heterochiral (bottom) yarns produced by mandrel coiling on a 300%-elongated, 0.5-mm-diameter rubber core, showing opposite changes in yarn twist during stretch of homochiral and heterochiral coils.

Downloaded from <http://science.sciencemag.org/> on January 18, 2019

energy. As shown in Fig. 2C and figs. S20 to S22 for isometric (constant-length) and isobaric (constant-force) twist insertion, respectively, twist insertion reversibly decreases the electrochemical capacitance and increases the OCV. The change in OCV is larger for isometric twist insertion (86.8 mV) than for isobaric twist insertion (43.6 mV), likely reflecting yarn densification and associated capacitance decrease during isobaric loading.

Inserting twist into a yarn until complete coiling occurs produces a “homochiral” yarn, because the twist to produce the noncoiled yarn and the subsequent yarn coiling are in identical directions. On the other hand, wrapping a twisted yarn around a mandrel can result in either homochiral or heterochiral coiled yarns, depending upon whether twist and coiling are in the same or opposite directions (23, 24). When a homochiral coiled yarn is stretched, yarn coiling (called writhe) is partially converted to increased yarn twist, which increases yarn density (fig. S36), decreases yarn capacitance, and thereby increases the OCV. Opposite changes occur when stretching a heterochiral yarn. Although mechanical jigs can convert motion into an out-of-phase tensile deformation of two otherwise identical yarn electrodes, thereby doubling harvester voltage (figs. S26 to S28), we can avoid this mechanical complexity by using heterochiral and homochiral yarns as opposite twistron harvester electrodes.

Yarn coiling and twist can irreversibly cancel when stretching an unsupported heterochiral yarn. Consequently, dual-harvesting-electrode twistron harvesters utilized harvester yarns wrapped around a rubber fiber core, which acts as a return

spring to prevent this irreversibility (22). Figure 2D shows the oppositely directed potential changes when stretching homochiral and heterochiral yarns, which further demonstrates that twist change is responsible for tensile energy harvesting by coiled yarns.

Harvesting without the need for an external bias voltage

Because a chemical potential difference exists between the harvester electrode and the surrounding electrolyte, immersing an electrode into an electrolyte generates an equilibrium charge on the electrode, which can be used for energy harvesting. The potential of zero charge (PZC) is needed for evaluating the equilibrium charge state of a twistron harvester. Because PZC measurements have been difficult and often inaccurate (25–27), we developed a method for measuring PZC, piezoelectrochemical spectroscopy (PECS). This method utilizes the charge-state-dependent response of a CNT electrode to mechanical deformation.

PECS involves characterizing an electrode by cyclic voltammetry (CV) while simultaneously stretching the electrode sinusoidally. Comparing CV scans with and without deformation, the dependence of the magnitude and phase of the stretch-induced ac current are determined versus applied potential (Fig. 3, A and B). From this plot, the PZC corresponds to the potential at which the ac current is minimized and the current's phase inverts by 180° (Fig. 3B). PECS showed that the PZC changes by less than ± 7 mV from 3° to 60°C, which is important for harvesting energy

from the ocean (Fig. 4C), and that the PZC changes by less than ± 5 mV when a coiled twistron harvester is stretched by 20%. This result indicates that the charge injected by the electrolyte is largely independent of strain (Fig. 3D).

For twistron yarns, the intrinsic bias voltage (the difference between the PZC and the OCV at 0% strain) decreases with increasing pH (Fig. 3C). Hence, a low-pH electrolyte is hole-injecting, and a high-pH electrolyte is electron-injecting. Although the bias voltage depends on the specific electrolyte, even at the same pH, a linear dependence of bias voltage on pH was obtained (-47 mV per pH unit for aqueous HCl) (fig. S15, inset), consistent with the -59 mV per pH unit predicted by the Nernst equation (28). The direction of OCV change with applied tensile strain depends on whether the electrolyte provides a positive or negative bias potential (Fig. 3C). The OCV and peak power were maximized for 0.1 M HCl and 0.6 M NaCl concentrations (figs. S8 and S9).

Of the electrolytes investigated, 0.1 M HCl provides the highest chemically generated intrinsic bias voltage, ~ 0.4 V, and the greatest increase in yarn potential with stretch (150 mV for 30% strain) (Fig. 3C). This peak potential (550 mV) is close to that which causes hydrolysis of aqueous electrolytes, leaving little opportunity to increase power by providing an external bias voltage. Applying a 300-mV bias voltage during tensile energy harvesting in 0.1 M HCl (using 0.2-Hz square wave deformation to 20%), the net energy harvested per cycle increased from 17.9 to 27.1 J·kg⁻¹ per cycle (fig. S14). Higher bias potentials decreased

the net harvested energy as electrolytic losses began to predominate.

The influence of yarn structure on electrochemical capacitance

Transmission electron microscopy (TEM) and scanning transmission electron microscopy (STEM) were used to assess the size, shape, and accessible surface area of individual CNTs and the bundles they form (22). Capacitances were calculated using the measured (29, 30) areal capacitance of the basal plane of graphite ($\sim 4 \mu\text{F}/\text{cm}^2$), which is close to that measured (31) for single-walled CNTs ($\sim 5 \mu\text{F}/\text{cm}^2$) (22). Although Chmiola *et al.* have demonstrated that pore sizes with a radius smaller than the solvated ion can have an enhanced areal capacitance (32), the present calculations approximate the areal capacitance to be independent of pore size.

Even though TEM and STEM images show that most nanotubes are bundled (Fig. 5, A and B), the measured capacitances in Fig. 2C and fig. S20 (5.8 F/g and 8.3 F/g for the partially twisted and nontwisted torsional harvesters, respectively) are close to those theoretically estimated for fully nonbundled MWNTs (9.7 F/g) (fig. S32) (22). This is explained by our observation that bundled MWNTs are far from cylindrical (Fig. 5, A and B, and fig. S35) (22) and that bundles have sufficiently large pores to accommodate electrolyte ions such as hydrated Na^+ and Cl^- (figs. S33 and S34). This electrolyte penetration occurs despite the fact that the investigated MWNTs are partially collapsed to gain internanotube van der Waals energy (Fig. 5A) instead of being noncollapsed or

fully collapsed (33, 34) to gain the van der Waals energy of the innermost nanotube wall.

To investigate how increasing twist causes reversible changes in yarn capacitance, we performed empirical-force-field molecular dynamics simulations on a typical observed bundled structure to predict the effect of twist-induced pressure on intrabundle void space (22). Using biaxial pressures up to 50 MPa, which agree with the measured torques required for twisting, a reversible 26% change in intrabundle capacitance (from 2.6 to 1.9 F/g) was calculated (figs. S37 to S39) (22), which is similar to the percent capacitance change seen experimentally during energy harvesting.

Twistron applications and comparisons to other harvesters

Transitioning from electrolyte-bath-operated harvesters to harvesters that operate in air is important. We fabricated one such device by first overcoating a coiled CNT yarn with a gel electrolyte [including 10 weight % (wt %) polyvinyl alcohol (PVA) in 0.1 M HCl], which did not degrade output power (fig. S29). Then a noncoiled, twisted, CNT yarn counter electrode, coated with an ionically conducting hydrogel to prevent shorting, was helically wrapped around the energy-harvesting electrode (i.e., fig. S30). Finally, this combined two-electrode assembly was overcoated with the PVA/HCl gel electrolyte to yield the peak voltage and peak harvested power shown in Fig. 4A.

To produce liquid-electrolyte-free harvesters that generate energy from both electrodes, we used the homochiral and heterochiral yarns of Fig. 2D. Three pairs of these homochiral and heterochiral

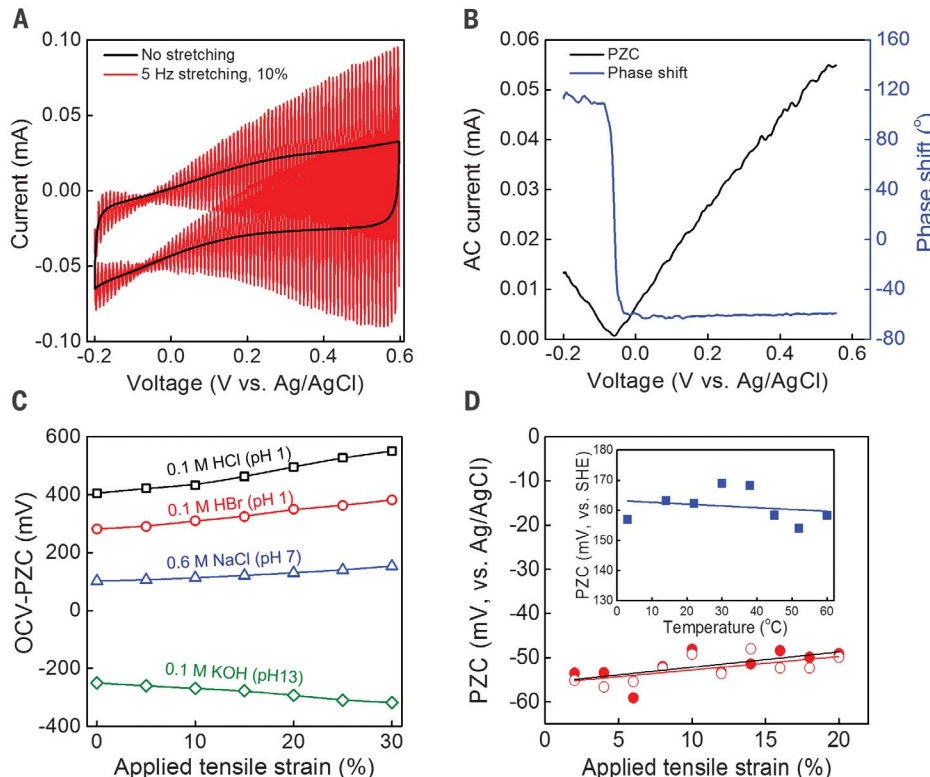
yarns were separately sewn into a knitted cotton glove, with a 1.5-mm interelectrode separation that matched the periodicity of the knit, and each electrode pair was then separately overcoated with a PVA/LiCl gel electrolyte. Figure 4B shows their performance when connected in parallel and in series when the textile is stretched by 50%. We demonstrated application of the twistron harvester of Fig. 4B as a self-powered solid-state strain sensor that is sewn into a shirt and used for monitoring breathing (fig. S31 and movie S1).

Figure 4C shows the results of an initial effort to harvest the energy of near-shore ocean waves. Both an energy harvesting coiled twistron yarn and a Pt mesh/CNT counter electrode were directly immersed in the Gyeonpo Sea off South Korea, where the ocean temperature was 13°C, the NaCl content was 0.31 M, and the wave frequency during the study ranged from 0.9 to 1.2 Hz. The yarn was attached between a balloon and a sinker on the seabed. Using a 10-cm-long twistron harvester electrode weighing 1.08 mg, whose deformation was mechanically limited to 25%, a peak-to-peak open-circuit voltage of 46 mV and an average output power of 1.79 μW were measured during ocean-wave harvesting. The average output power through a 25-ohm load resistor (normalized to the harvester electrode weight) was 1.66 W/kg.

Our harvester yarns can provide arbitrarily high voltages if multiple harvesters are combined in series, as in Fig. 4B, or commercially available circuits are used to increase harvester voltage. For instance, the ~80-mV output voltage of a single coiled harvester electrode (weighing 19.2 mg)

Fig. 3. Piezoelectrochemical spectroscopy and its application for twistron harvesters.

(A) Cyclic voltammograms (50-mV/s scan rate) of a coiled twistron electrode in 0.1 M HCl during a 5-Hz sinusoidal stretch to 10% (red) and without deformation (black). (B) Magnitude and phase of current fluctuations relative to the applied mechanical stretch. The potential of both the minimum current amplitude and the 180° phase shift correspond to the potential of zero charge (PZC) (~58 mV versus Ag/AgCl). (C) OCV (versus PZC) in different electrolytes for 1-Hz strain, indicating the combined effects of chemically induced charge injection and stretch-induced capacitance change. (D) Negligible dependence of PZC on applied strain for increasing (solid) and decreasing (open) strain and temperature (inset). SHE, standard hydrogen electrode.



charged a 5- μ F capacitor to 2.8 V using a voltage step-up converter (fig. S40 and Fig. 4D). Movie S2 shows this harvester powering a green light-emitting diode, which lights up to indicate each time the harvester yarn is stretched.

We previously used polymer artificial muscles to convert temperature fluctuations into mechanical energy, which was harvested as electrical energy using an electromagnetic generator (35). Unfortunately, the large weight and volume of the electromagnetic generator dwarfs the polymer muscle, and these electromagnetic generators suffer from low gravimetric and volumetric power output when downsized (36). Twisted harvesters can be used to solve this problem because they can be smaller in diameter than a human hair and have much smaller weight and volume than the polymer muscle used to convert thermal energy to mechanical energy. A thermally annealed coiled-nylon-fiber artificial muscle was attached to a coiled twisted harvester with the same twist direction. Heating the nylon muscle both up-twists and stretches the twisted harvester, additively contributing to energy generation. Upon heating from room temperature to 170°C in 1 s, followed by air cooling for 2 s, actuation of a 10-cm-long coiled-nylon muscle drove the 2-cm-long twisted yarn to deliver a peak electrical power of 40.7 W/kg, relative to twisted weight (Fig. 4E). Considering the entire system weight, including both the weight of the actuating nylon yarn and the 28-fold lower weight of the twisted energy harvester, this corresponds to 1.41 W/kg of peak electrical power and 0.86 W/kg of average power during heating and a full-cycle average electrical power of 0.29 W/kg, compared with 0.015 W/kg for a polymer muscle connected to an electromagnetic generator (36). Small temperature fluctuations can be harvested by increasing the polymer muscle length, such as by using pulleys to minimize total package size or by using large-spring-index polymer muscle coils to maximize stroke (37).

A twisted harvester's output power is limited by its electrical impedance. Although the full equivalent harvester circuit is complex, a simple R - C model can qualitatively describe the main observed features. In this approximation, the harvester impedance is $Z_{\text{harvester}} = R_{\text{internal}} + 1/(j\omega C)$, where j is $\sqrt{-1}$ and ω is the angular frequency. At low stretch frequencies, this impedance is dominated by the double-layer capacitance ($Z_c = 1/j\omega C$), leading to the observed rise in power with increasing frequency (Fig. 1E and fig. S10). At higher frequencies, where capacitor impedance is minimal, internal resistance (R_{internal}) dominates, and power output versus frequency reaches a plateau.

A major performance increase resulted from our discovery that yarn resistance was contributing to twisted impedance (fig. S12). Peak power for 50% stretch at 12 Hz was increased from 179 W/kg (Fig. 1E) to 250 W/kg (Fig. 4D and fig. S16) by coiling a 23- μ m-diameter Pt wire within the coiled twisted yarn. Though it did not substantially affect the stress-strain curve of the elastically stretched harvester (fig. S17), the presence of the conducting wire also increased the average output

electrical power for 12-Hz sinusoidal deformation from 39 to 56 W/kg. On the basis of this average power output, just 31 mg of CNT yarn harvester could provide the average power needed to transmit a 2-kB packet of data over a 100-m radius

every 10 s (38) for the Internet of Things.

Figure 5, C and D, and table S2 compare the gravimetric power densities of our tensile twisted harvesters to alternative microscale or macroscale technologies, some of which have had decades

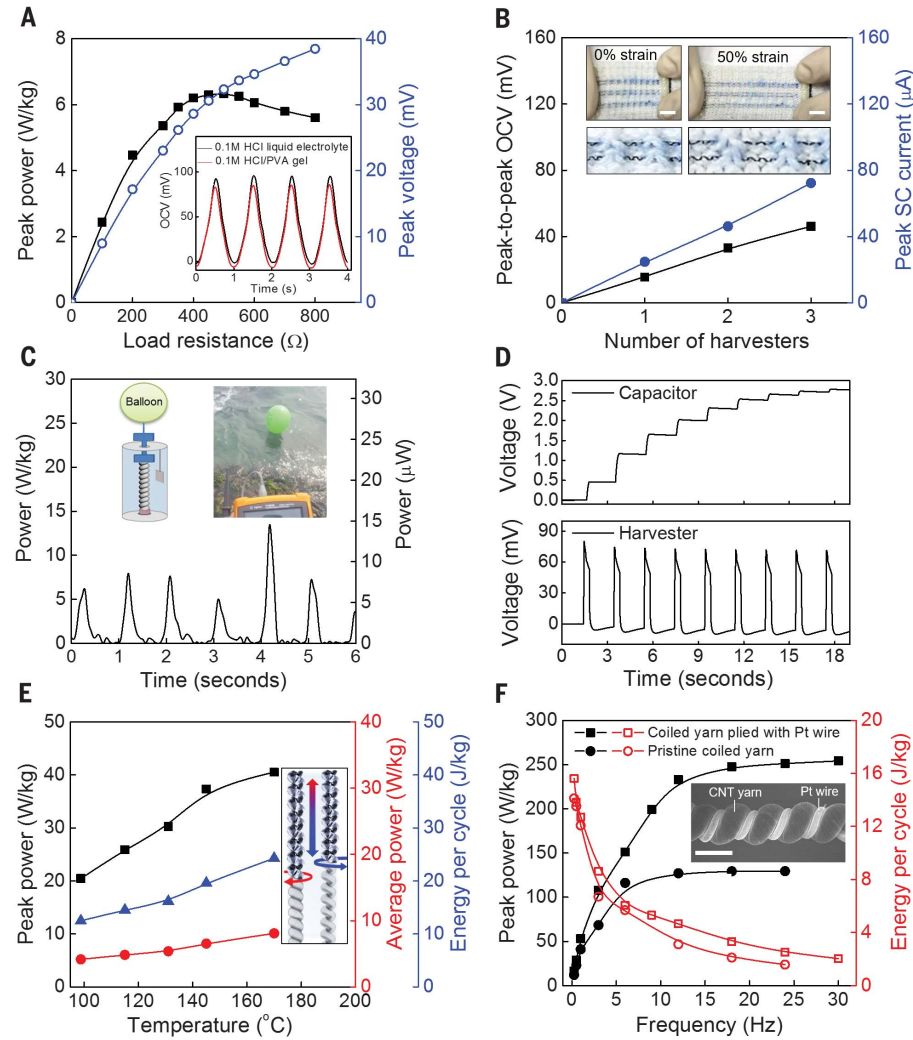


Fig. 4. Alternative harvester geometries. (A) Peak power per device weight and peak voltage versus load resistance for 1-Hz, 30% stretch of a harvesting coiled CNT yarn working electrode that is coated with 0.1 M HCl-containing polyvinyl alcohol (PVA) gel and wrapped with a nonharvesting, PVA/HCl-coated, noncoiled CNT yarn counter electrode. (Inset) OCV versus time, before and after PVA coating. (B) Peak-to-peak OCV and peak SCC at 1 Hz and 50% strain for series (black squares) and parallel (blue circles) connected harvesters using homochiral and heterochiral yarn pairs. The yarns were coated with a 10-wt % PVA/4.5 M LiCl gel electrolyte after being sewn into a textile. (Inset) Photographs of the textile at 0 and 50% strain (scale bars, 1 cm). (C) Gravimetric and absolute power output of a 1.08-mg twisted ocean-wave harvester for wave frequencies of 0.9 to 1.2 Hz. The average power was 1.79 μ W. (Inset) The harvester configuration, which was tethered to the ocean floor and mechanically limited to <25% stretch, and a photograph taken during harvesting. (D) Data from charging a 5- μ F capacitor to 2.8 V using a CNT yarn harvester (weighing 19.2 mg) and a boost converter circuit. The capacitor voltage and the harvester voltage are shown during a 0.5-Hz square wave stretch to 14% strain at 20% duty. The boost converter output was rectified through a Schottky diode before charging the capacitor. (E) Peak power (black squares), average power (red circles), and energy per cycle (blue triangles) generated by a coiled twisted harvester when stretched and twisted by an in-series, coiled, 127- μ m-fiber-diameter nylon artificial muscle (above the electrolyte) that converts thermal energy into mechanical energy. (Inset) Illustration of twisted up-twist and stretch during muscle heating and the reverse processes during muscle cooling. (F) Frequency dependence of peak power (black symbols) and energy per cycle (red symbols) before and after incorporating a Pt wire current collector into a coiled twisted yarn. (Inset) Scanning electron microscopy image of this harvester (scale bar, 100 μ m).

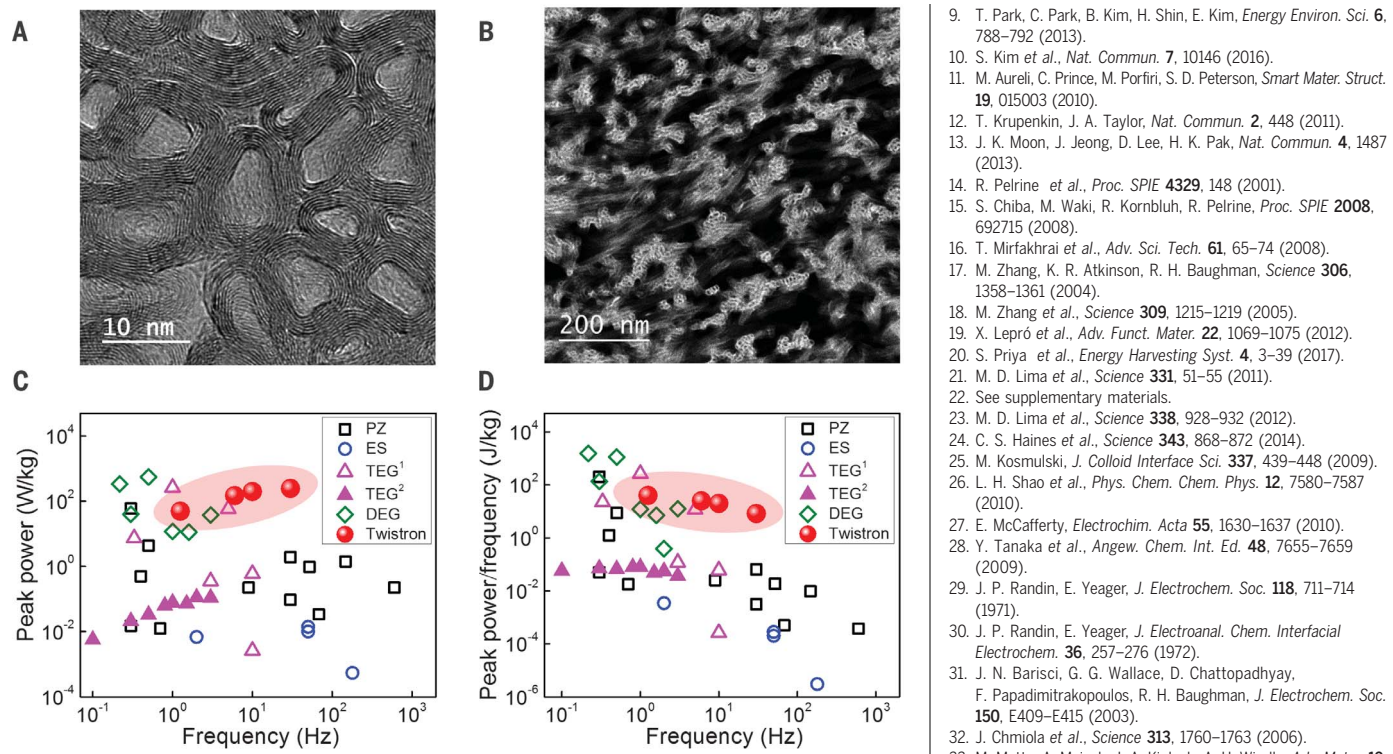


Fig. 5. Structural origin of twistron performance and comparisons with previously known material-based harvesters. (A) TEM image showing multiwalled nanotube (MWNT) collapse to increase internanotube van der Waals energy in a MWNT bundle. (B) STEM image showing the high surface area of MWNT bundles. (C and D) Peak power (C) and frequency-normalized peak power (D) versus the frequency at which this peak power was obtained for present and prior-art technologies for piezoelectric (PZ), electrostatic (ES), triboelectric (TEG¹), and dielectric elastomer (DEG) generators (22). The solid triangles represent the low-frequency triboelectric data (TEG²) of Zi et al. (36).

or centuries to mature. For stretch frequencies between a few hertz and 600 Hz, we could find no other material-based harvesting technology that provides a higher reported peak power or frequency-normalized peak power than our twistron harvesters. At very high frequencies, Zhu et al. (39) have reported that triboelectric harvesters can generate noteworthy average power outputs (1.27 kW/kg at 1 kHz and 5 kW/kg at 5 kHz, which correspond to frequency-normalized average power values of 1.27 and 1.00 J/kg, respectively). Extrapolation to lower frequencies, using the reported approximately linear dependence of average power on frequency for these triboelectric harvesters, suggests that they should provide a higher average power density than twistron harvesters for frequencies >100 Hz (37).

The high gravimetric output power of twistron harvesters reflects the high gravimetric mechanical energy that can be input during stretch (1.67 kJ/kg for 20% strain), rather than a high mechanical-to-electrical energy conversion efficiency. In fact, simultaneous measurement of tensile mechanical energy input and electric energy output during cycling of a coiled twistron yarn at 1 Hz to 20% strain in 0.1 M HCl resulted in an energy conversion efficiency of only 1.05% for this first generation of twistron harvesters (fig. S19).

Future application of the twistron harvesters might result from their high gravimetric power densities, the giant stroke range over which mechanical energy can be harvested, the broad frequency range over which these harvesters provide high power, their operation in seawater and other electrolytes without the need for an external bias potential, and their scalability from micrometer-scale-diameter harvesters in textiles to parallel devices that harvest ocean energy. The low mechanical-to-electrical conversion efficiency of the twistron harvesters is a present problem for applications in which high gravimetric output power is less important than energy conversion efficiency.

REFERENCES AND NOTES

- S. Beeby, T. O'Donnell, "Electromagnetic energy harvesting" in *Energy Harvesting Technologies*, S. Priya, D. Inman, Eds. (Springer, 2009).
- L. Persano et al., *Nat. Commun.* **4**, 1633 (2013).
- Z. L. Wang, J. Song, *Science* **312**, 242–246 (2006).
- S. Niu, X. Wang, F. Yi, Y. S. Zhou, Z. L. Wang, *Nat. Commun.* **6**, 8975 (2015).
- W. Tang et al., *ACS Nano* **9**, 7867–7873 (2015).
- J. Yin et al., *Nat. Nanotechnol.* **9**, 378–383 (2014).
- S. Ghosh, A. K. Sood, N. Kumar, *Science* **299**, 1042–1044 (2003).
- J. W. Liu, L. M. Dai, J. W. Baur, *J. Appl. Phys.* **101**, 064312 (2007).
- T. Park, C. Park, B. Kim, H. Shin, E. Kim, *Energy Environ. Sci.* **6**, 788–792 (2013).
- S. Kim et al., *Nat. Commun.* **7**, 10146 (2016).
- M. Aureli, C. Prince, M. Porfiri, S. D. Peterson, *Smart Mater. Struct.* **19**, 015003 (2010).
- T. Krupenkin, J. A. Taylor, *Nat. Commun.* **2**, 448 (2011).
- J. K. Moon, J. Jeong, D. Lee, H. K. Pak, *Nat. Commun.* **4**, 1487 (2013).
- R. Peirine et al., *Proc. SPIE* **4329**, 148 (2001).
- S. Chiba, M. Waki, R. Kornbluh, R. Peirine, *Proc. SPIE* **2008**, 692715 (2008).
- T. Mirfakhrai et al., *Adv. Sci. Tech.* **61**, 65–74 (2008).
- M. Zhang, K. R. Atkinson, R. H. Baughman, *Science* **306**, 1358–1361 (2004).
- M. Zhang et al., *Science* **309**, 1215–1219 (2005).
- X. Lepró et al., *Adv. Funct. Mater.* **22**, 1069–1075 (2012).
- S. Priya et al., *Energy Harvesting Syst.* **4**, 3–39 (2017).
- M. D. Lima et al., *Science* **331**, 51–55 (2011).
- See supplementary materials.
- M. D. Lima et al., *Science* **338**, 928–932 (2012).
- C. S. Haines et al., *Science* **343**, 868–872 (2014).
- M. Kosmulski, *J. Colloid Interface Sci.* **337**, 439–448 (2009).
- L. H. Shao et al., *Phys. Chem. Chem. Phys.* **12**, 7580–7587 (2010).
- E. McCafferty, *Electrochim. Acta* **55**, 1630–1637 (2010).
- Y. Tanaka et al., *Angew. Chem. Int. Ed.* **48**, 7655–7659 (2009).
- J. P. Randin, E. Yeager, *J. Electrochem. Soc.* **118**, 711–714 (1971).
- J. P. Randin, E. Yeager, *J. Electroanal. Chem. Interfacial Electrochem.* **36**, 257–276 (1972).
- J. N. Barisci, G. G. Wallace, D. Chatopadhyay, F. Papadimitrakopoulos, R. H. Baughman, *J. Electrochem. Soc.* **150**, E409–E415 (2003).
- J. Chmiola et al., *Science* **313**, 1760–1763 (2006).
- M. Motta, A. Moisala, I. A. Kinloch, A. H. Windle, *Adv. Mater.* **19**, 3721–3726 (2007).
- M. F. Yu, M. J. Dyer, R. S. Ruoff, *J. Appl. Phys.* **89**, 4554–4557 (2001).
- S. H. Kim et al., *Energy Environ. Sci.* **8**, 3336–3344 (2015).
- Y. Zi et al., *ACS Nano* **10**, 4797–4805 (2016).
- C. S. Haines et al., *Proc. Natl. Acad. Sci. U.S.A.* **113**, 11709–11716 (2016).
- W. R. Heinzelman, A. Chandrakasan, H. Balakrishnan, "Energy-efficient communication protocol for wireless microsensor networks," in *Proceedings of the 33rd Hawaii International Conference on System Sciences* (IEEE, 2000), p. 8020.
- G. Zhu et al., *Adv. Mater.* **26**, 3788–3796 (2014).

ACKNOWLEDGMENTS

We thank B. Buckenham, A. M. Baughman, and N. K. Mayo for preparing samples and performing measurements. This work was supported in Korea by the Creative Research Initiative Center for Self-Powered Actuation of the National Research Foundation of Korea and the Ministry of Science, ICT & Future Planning, the Korea-U.S. Air Force Cooperation Program (grant 2013K1A3A1A32035592), and a KETEP grant (20168510011350) grant of the Ministry of Knowledge Economy. In the United States, this work was supported by Air Force Office of Scientific Research grants (FA9550-15-1-0089 and FA9550-12-1-0035), an Air Force grant (AOARD-FA2386-13-4119), a NASA project (NNX15CS05C), a Robert A. Welch Foundation grant (AT-0029), and an Office of Naval Research grant (N00014-14-1-0158). S.H.K., C.S.H., N.L., S.F., J.D., K.J.K., T.J.M., C.C., S.J.K., and R.H.B. are the inventors of provisional U.S. patent application no. 62/526,188, submitted jointly by the Board of Regents, the University of Texas System (for the University of Texas at Dallas), and the Industry-University Cooperation Foundation of Hanyang University, that covers the design, fabrication, performance, and applications of twistron mechanical energy harvesters.

SUPPLEMENTARY MATERIALS

www.sciencemag.org/content/357/6353/773/suppl/DC1
Materials and Methods
Supplementary Text
Figs. S1 to S40
Tables S1 and S2
References (40–79)
Movies S1 and S2

3 February 2017; accepted 21 July 2017
10.1126/science.aam8771

Harvesting electrical energy from carbon nanotube yarn twist

Shi Hyeong Kim, Carter S. Haines, Na Li, Keon Jung Kim, Tae Jin Mun, Changsoon Choi, Jiangtao Di, Young Jun Oh, Juan Pablo Oviedo, Julia Bykova, Shaoli Fang, Nan Jiang, Zunfeng Liu, Run Wang, Prashant Kumar, Rui Qiao, Shashank Priya, Kyeongjae Cho, Moon Kim, Matthew Steven Lucas, Lawrence F. Drummy, Benji Maruyama, Dong Youn Lee, Xavier Lepro, Enlai Gao, Dawood Albarq, Raquel Ovalle-Robles, Seon Jeong Kim and Ray H. Baughman

Science 357 (6353), 773-778.
DOI: 10.1126/science.aam8771

Making the most of twists and turns

The rise of small-scale, portable electronics and wearable devices has boosted the desire for ways to harvest energy from mechanical motion. Such approaches could be used to provide battery-free power with a small footprint. Kim *et al.* present an energy harvester made from carbon nanotube yarn that converts mechanical energy into electrical energy from both torsional and tensile motion. Their findings reveal how the extent of yarn twisting and the combination of homochiral and heterochiral coiled yarns can maximize energy generation.

Science, this issue p. 773

ARTICLE TOOLS

<http://science.scienmag.org/content/357/6353/773>

SUPPLEMENTARY MATERIALS

<http://science.scienmag.org/content/suppl/2017/08/24/357.6353.773.DC1>

REFERENCES

This article cites 69 articles, 11 of which you can access for free
<http://science.scienmag.org/content/357/6353/773#BIBL>

PERMISSIONS

<http://www.scienmag.org/help/reprints-and-permissions>

Use of this article is subject to the [Terms of Service](#)

Originally published 25 August 2017; corrected 28 September 2017



www.sciencemag.org/content/357/6353/773/suppl/DC1

Supplementary Materials for

Harvesting electrical energy from carbon nanotube yarn twist

Shi Hyeong Kim,* Carter S. Haines,* Na Li,* Keon Jung Kim, Tae Jin Mun, Changsoon Choi, Jiangtao Di, Young Jun Oh, Juan Pablo Oviedo, Julia Bykova, Shaoli Fang, Nan Jiang, Zunfeng Liu, Run Wang, Prashant Kumar, Rui Qiao, Shashank Priya, Kyeongjae Cho, Moon Kim, Matthew Steven Lucas, Lawrence F. Drummy, Benji Maruyama, Dong Youn Lee, Xavier Lepró, Enlai Gao, Dawood Albarq, Raquel Ovalle-Robles, Seon Jeong Kim,† Ray H. Baughman†

*These authors contributed equally to this work.

†Corresponding author. Email: skj@hanyang.ac.kr (S.J.K.); ray.baughman@utdallas.edu (R.H.B.)

Published 25 August 2017, *Science* **357**, 773 (2017)
DOI: 10.1126/science.aam8771

This PDF file includes:

Materials and Methods
Supplementary Text
Figs. S1 to S40
Tables S1 and S2
Captions for Movies S1 and S2
References

Other Supplementary Material for this manuscript includes the following:

(available at www.sciencemag.org/content/357/6353/773/suppl/DC1)

Movies S1 to S2

Correction: In the original file, fig. S18 was a duplicate of fig. S3. This updated file contains the correct fig. S18.

Materials and Methods

1. Twistron Harvester Fabrication

Our twistron harvesters were fabricated from carbon multiwalled nanotubes (MWNTs) that were drawn from MWNT forests. Using acetylene (C_2H_2) gas as the carbon precursor, these MWNT forests were grown by chemical vapor deposition (CVD) at 680 °C on silicon wafers that were coated by 3-nm-thick iron catalyst (17, 18). Although there is considerable polydispersity in MWNT radius and number of walls, transmission electron microscope (TEM) and scanning electron microscope (SEM) images of the ~300 μm high forests indicate that the MWNTs have an outer diameter of ~10 nm, contain ~7 walls, and form irregularly shaped bundles. Thermogravimetric analysis indicates that the amount of non-combustible material in the drawn nanotubes is below 1 wt%, which places an upper limit on the amount of residual catalyst.

To make cone-spun and dual-Archimedean twistron yarns, MWNT sheets drawn from a MWNT forest were assembled into a ~4-cm-wide, ~30-cm-long sheet stack in which the MWNTs were aligned along the sheet length direction. Since the areal density of the as-drawn MWNT sheets varied between 1.7 and 2.2 μg/cm², the typical number of sheets in the sheet stack was 5 for the lower density sheets and 4 for the higher density sheets.

For cone spinning, two 4-cm-long, 1-cm-wide pieces of adhesive carbon tape were attached to each end of a MWNT sheet stack, and then the flat MWNT sheet stack was manually rolled into a ~1.3-cm-diameter cylinder (Fig. S1). The MWNT cylinder was then suspended vertically (by attachment to a motor at its top end), with an ~11.2 g load attached at the bottom (that provided ~31 MPa of stress, when normalized to the final diameter of the twisted yarn). Twist was inserted about the central axis of this cylinder, while prohibiting the rotation of its bottom end. The sheet stack deformed into two cones during this process, forming a dense yarn between these cones. The amount of twist typically used to make the twisted yarns was 3,800 turns/m, when normalized to the length of the original sheet stack.

To produce dual-Archimedean-spun yarns, the same initial sheet stack was used, and the same mechanical load was applied as for the cone-spun process. However, in this case, the sheet stack was kept flat, by attaching each end of the sheet stack to a rigid support. Spinning was then performed by inserting twist into this flat sheet stack. Due to the stress gradient created during this process, yarn cores formed along both sheet edges of the spinning wedges, and these cores were then twisted together to form a dual-Archimedean-spun yarn (21).

Fermat yarns were fabricated by symmetrically drawing CNTs from a CNT forest while twist was simultaneously inserted into the yarn, so that the base of the spinning wedge is the CNT forest and the yarn core arises from the center of this spinning wedge. Since CNT draw from the forest can occur non-uniformly over the forest's width, the highly non-uniform stress encountered in dual-Archimedean spinning was avoided.

Similarly, highly non-uniform stresses do not arise during funnel spinning, where the spinning wedge is generated from a funnel-shaped array of MWNT forests. In this funnel spinning process, three or more CNT forests were arrayed as the base of the spinning funnel. Simultaneous draw from these forests produced a funnel-shaped CNT array that was twist spun into yarn as the CNTs were drawn from the CNT forests. As is the case for the Fermat spinning process, the effective load applied during spinning was determined by the force needed to draw the CNTs from the forest.

As a final method for producing harvester yarns, called “tow spinning”, a stack of 4-5 CNTs sheets (having the same dimensions as described for dual-Archimedean yarn spinning and cone spinning) was formed into an oriented, non-twisted CNT yarn (called a tow, like for conventional yarns). This was accomplished by stacking the CNT sheets on a glass substrate, absorbing ethanol into the CNT sheet stack, and removing the sheet stack from the glass substrate before the ethanol evaporated. After the sheet stack was removed from the glass substrate, the sheet stack was attached to the load used for twist insertion. Upon subsequent evaporation of the ethanol, the thereby generated surface-tension-derived forces collapse the sheet stack into yarn shape. The load applied during this process and the amount of inserted twist was the same as used for dual-Archimedean and cone spinning. This use of the same sheet stack for this process and for the dual-Archimedean and cone spinning processes enabled us to keep the yarn diameter obtained by all three processes roughly constant (~50-70 μm). Unless otherwise indicated for both twisted and coiled yarns, the yarn diameter is defined as the diameter of the twisted yarn immediately before the onset of coiling.

Homochiral coiled yarns (in which yarn twist and yarn coiling had the same chirality) were made for dual-Archimedean yarns, cone-spun yarns, and tow-spun yarns by continuing the twist insertion process (without changing the isobaric load) until complete yarn coiling resulted. This coiling method is called “self-coiling”. Heterochiral yarns (where yarn twist and yarn coiling have opposite chiralities) were made by wrapping a highly twisted yarn (which had been twisted to just before the onset of coiling) around a 500 μm diameter silicone rubber mandrel, which was stretched by 300% before the wrapping process (thereby reducing the mandrel diameter to 250 μm) (Fig. 2D). The twisted yarn was close-packed on the mandrel during this wrapping process and the ends of the highly twisted yarn were attached to the silicone rubber using epoxy. Since the rubber mandrel has a Poisson’s ratio of close to 0.5, mandrel volume is conserved during stretch, which explains why quadrupling the mandrel length halves the mandrel diameter. This use of a rubber fiber mandrel during energy harvesting provided a lower bound on coil diameter, which prevented coil collapse and cancellation of the oppositely directed yarn twist and yarn coiling for the heterochiral yarn. However, unlike the case of a mandrel-free homochiral yarn made by self-coiling, mandrel coils supported on a rubber fiber must change diameter according to the rubber fiber’s Poisson’s ratio, which caused increased stretch-torsional coupling for heterochiral coils, but decreased this coupling for homochiral coils that are supported on a rubber fiber. To produce these homochiral and heterochiral yarns, two CNT sheet stacks were cone-spun in opposite twist directions until just before the onset of coiling, which was determined by twisting until the first coil appears, and then using the remaining highly-twisted, but not coiled yarn. Both electrodes were then coiled in identical directions around 300%-elongated, 0.5-mm-diameter rubber mandrels.

2. Electrochemical Methods for Characterizing Twistron Harvesters

Unless otherwise stated, three-electrode experiments were conducted using a twistron yarn as the working electrode, a counter electrode made from Pt mesh and high-surface-area carbon (CNTs or graphene), and a Ag/AgCl reference electrode. This counter electrode had a sufficiently high capacitance, relative to the twistron electrode, that the cell capacitance was largely determined by the capacitance of the twistron electrode. The open circuit voltage (OCV) between the twistron electrode and the counter electrode, the

potential of the twistron electrode relative to the reference electrode, the short circuit current (SCC), and the capacitance were measured using a Gamry potentiostat. Using this potentiostat, the short-circuit current was measured between the two electrodes by holding the inter-electrode voltage at zero volts (i.e. short circuiting the electrodes) and recording the resulting current. When a resistive load was applied to measure the power output of the harvester, current was measured either by in-line current measurement through a potentiostat or by measuring the voltage under load and calculating the current as $I=V/R$. Unless otherwise indicated, electrode capacitances were measured by cyclic voltammetry (CV) across small potential ranges which do not cause redox processes (0.3 to 0.6 V versus Ag/AgCl) and the potential scan rate was 50 mV/s. Average and peak electrical power, and output per-cycle energy were measured by connecting an external load resistor between the twistron harvester electrode and the counter electrode, and recording the resulting voltage during mechanical deformation. Average output power and peak output power were simultaneously optimized by varying the load resistor.

Regarding measurement error, Fig. 2B shows the results obtained for 30,000 consecutive cycles. For the 27 cycles plotted (which we did not in any way preferentially select), the standard deviation of the average power, peak power, and energy per cycle were 0.0280 W/kg, 0.0275 W/kg, and 0.0280 J/kg, respectively, which correspond to relative standard deviations (standard deviation divided by the mean) of 0.00183, 0.000594 and 0.00183, respectively. To evaluate, the reproducibility of property measurements for nominally identically fabricated harvesters, we fabricated five separate harvesters from a cone spun yarn and then characterized their individual performance for sinusoidal stretch to 15% strain at 1 Hz in 0.1 M HCl. For these five harvester yarns, the average values of average power, peak power, and energy per cycle were 4.39 W/kg, 11.46 W/kg, and 4.39 J/kg, respectively, and the standard deviation of the average power, peak power, and energy per cycle were 0.199 W/kg, 0.250 W/kg, and 0.199 J/kg, respectively, which correspond to relative standard deviations of 0.0453, 0.0218, and 0.0453, respectively. (Note that average power in W/kg and the electric energy per cycle in J/kg have identical values for the trivial reason that the frequency of stretch was 1 Hz.) Although yarn capacitance and harvester performance is sensitive to the structural nature of the MWNT forest used as precursor for the cone spun yarns, the above results for identically grown forests show that measurement errors are small and that harvesters fabricated from the same forest type provide essentially identical performance.

Three kinds of mechanical deformation were applied to a twistron electrode in order to characterize mechanical energy harvesting: 1) stretch and release of a coiled yarn that was torsionally tethered to prohibit irreversible yarn untwist; 2) isobaric (constant load) twist and untwist; and 3) isometric (constant length) twist and untwist.

3. Equipment and Sample Preparation Methods for Microscopy on Twistron Yarns and Precursor Nanotube Sheets

Transmission electron microscope (TEM), scanning transmission electron microscope (STEM), and scanning electron microscope (SEM) images, and x-ray tomography were used to improve understanding of the structural nature of the MWNT twistron harvesters. A JEOL 2100F TEM equipped with GIF – Tridiem (for mapping of elements by electron energy loss spectroscopy, EELS) was used at 200 kV. A JEOL JEM-ARM 200F STEM equipped with a CEOS Cs probe corrector and an Oxford Instruments SDD EDS detector

were used at 200 kV. A Zeiss SUPRA 40 SEM was used for SEM imaging. X-ray tomography images were obtained for torsionally-tethered twisted and coiled yarns using a Zeiss XRadia 810 Ultra, utilizing a Cr source with incident x-ray energy of 5.4 keV.

Approximately 150-nm-thick CNT yarn cross-sections suitable for TEM imaging (along the yarn axis direction) were made using a FEI Nova Nanolab 200 Dualbeam, using the FIB (focused ion beam) lift-out procedure and FIB deposited Pt for final polishing to electron transparency. To obtain a cross-section of a twistron yarn having a distribution of NaCl ions as close as possible to that of the experimental twistron testing conditions, the yarn was freeze-dried from a 0.6 M NaCl solution using liquid nitrogen.

Supplementary Text

4. Coiled Twistron Harvesters for Tensile Energy Harvesting

4.1. The spring index and spinning methods that maximize tensile energy harvesting for coiled twistron yarns

To evaluate the effect of spring index on tensile harvester performance, the load applied during twist insertion and coiling was varied between 6.3 and 40.8 MPa for cone-spun yarns, which caused the spring index to decrease from 0.56 to 0.38. Using 0.1 M HCl electrolyte, we found that a spring index of ~0.43 optimized the output power obtainable by deformation over the full available tensile stroke range, which increased with increasing spring index (Fig. S2). For the above described sheet stack used for cone spinning (which provides a yarn diameter at the onset of coiling of ~58 μm) the total amount of inserted twist (relative to the initial length of the sheet stack) to obtain complete coiling was about 6,700 turns/m, and the spring index was about 0.43 when the applied load was 32.7 MPa. When the twisted yarn diameter before the onset of coiling was kept approximately constant for the different spinning methods that use sheet stacks, the total amount of inserted twist to obtain complete coiling and the resulting spring index were essentially unchanged when the engineering stress during twist insertion was held constant.

Using the 0.1 M HCl electrolyte, similar performance results as coiled-yarn tensile harvesters (Table S1) were obtained by spinning methods that maintained quasi-uniform tension across the array of CNTs, such as by (1) inserting twist into an oriented yarn obtained by collapsing a sheet stack using lateral pressure (or liquid-based densification) or (2) ‘funnel spinning’, wherein yarn is spun by drawing and twisting from a cylindrically positioned array of CNT forests. The direct spinning of yarn from a CNT forest to produce a Fermat yarn (17, 21) also provided a yarn that had similarly high performance for energy harvesting as the cone-spun, funnel-spun, and tow-spun yarns (Table S1).

Figure S3A shows the time dependence of the open circuit voltage (OCV) of a coiled twistron electrode (versus a Ag/AgCl reference electrode) when yarns spun by different methods are stretched at 1 Hz to 30% strain in 0.1 M HCl. Figure S3B compares, for these different yarns, the peak-to-peak change of OCV and the peak power output for the strain percent and frequency of Fig. 3A. These results for 30% stretch show that the peak power output and generated OCV of the dual-Archimedean coiled yarn is much lower than for coiled yarns spun using other spinning methods.

Figure S4 shows that immersion of the cone-spun yarn in the above 0.1 M HCl electrolyte increases the yarn diameter from 72 μm to 90 μm and decreases the coil bias angle from 46° to 34°. Figure S5 shows the reversible changes in yarn diameter and coil

bias angle upon cycling the above torsionally tethered coiled yarn from 0% strain (90 μm and 34°) to 30% strain (75 μm and 50°), and then back to 0% strain (90 μm and 34°).

4.2. The effect of slightly untwisting a coiled cone-spun yarn on tensile energy harvesting performance

The results in Fig. 2A show that slightly untwisting a coiled twistron yarn (by 500 turns/m of twist, which is 8.5% of the twist inserted to fully coil) improved yarn performance as a tensile twistron energy harvester. This improvement was possible since the twist insertion process to provide complete coiling is hysteretic, meaning the untwisting of a fully coiled yarn does not immediately result in coil loss, but instead increases spring index and reduces twist-induced yarn densification. Fig. 2A shows that untwisting by 500 turns/m increased the reversible tensile strain range from 30% to 50%, increased the zero-tensile-strain capacitance from 3.97 to 6.50 F/g, and increased the tensile-strain-induced capacitance change from 30% to 36%. As a result of this twist removal, the peak output power was approximately doubled.

Figure S6 provides more complete information on the effects of twist removal from a coiled cone-spun MWNT yarn on tensile twistron harvester performance. Removal of 330 and 500 turns/m (1) increases the capacitance at zero strain, (2) increases the tensile strain range where tensile energy harvesting reversibly occurs, (3) increases the capacitance change and the change in OCV over the available strain range, (4) increases the peak output power and output voltage for an impedance matched load, and (5) does not noticeably change the matching impedance. While increasing the removed twist from 0 to 330 and to 500 turns/m provides increasing harvester performance, this benefit disappears for higher amounts of untwist. The reason is that further untwisting initiates coil removal, which is detrimental to harvester performance.

4.3. The effect of twistron yarn diameter and length on tensile energy harvesting using a coiled cone-spun yarn

We next investigate the effects of yarn diameter on the tensile energy harvesting abilities of a coiled twistron yarn when operated in 0.1 M HCl electrolyte. As done elsewhere, unless otherwise mentioned, the yarn diameter indicated is the diameter of the twisted yarn immediately before the onset of coiling. These yarns were coiled analogously by applying a load during twist insertion that was proportional to the square of yarn diameter. Yarn structure was then automatically scaled to produce a spring index of 0.43, since the amount of yarn twist needed to produce complete coiling was inversely proportional to yarn diameter.

Figure S7 shows the scalability of performance with yarn diameter. The per-cycle gravimetric output energy, the open circuit peak-to-peak voltage, the frequency dependence of gravimetric peak output power, and the load conductance that optimized power output (normalized to yarn weight, or equivalently, yarn cross-sectional area) were independent of yarn diameter when yarn length was kept constant. However, for sufficiently large yarn diameters, where the intra-yarn ionic conductivity becomes important, the gravimetric peak output power and the load conductance that optimizes power output (normalized to yarn weight) should decrease with increasing yarn diameter when twistron length is constant.

4.4. The effect of aqueous electrolyte type and molarity on tensile energy harvesting by a coiled cone-spun yarn

Figure S8A shows that the peak power for tensile energy harvesting at 1 Hz is insensitive to HCl concentrations in the range from 0.1 M to 1 M, but rapidly drops for both lower and higher HCl concentrations. The performance drop for lower HCl concentrations likely results mainly from decreased electrolyte conductivity (which results in the indicated increase in the load resistance that maximizes power output at these concentrations). The performance drop at higher HCl concentrations is caused by a drop in the peak-to-peak open circuit voltage of the twistron harvester.

Figure S8B shows that the output energy per cycle (like the peak output power) is maximized for electrolyte concentrations between 0.1 M HCl and 1 M HCl, and that HCl concentrations outside this range have a sharply decreased output energy per cycle. While the percent capacitance change during 30% strain (~32%) is insensitive to HCl concentration, the capacitance of the twistron harvester at zero strain increases approximately linearly with the log of the electrolyte concentration (changing from 1.47 F/g at 10^{-3} M HCl to 5.84 F/g at 3 M HCl). Hence, the capacitance change potentially available for energy harvesting continuously increases with increasing HCl concentration. Figure S8C shows that the peak-to-peak OCV is insensitive to stretch frequency for 0.01 M HCl, slightly decreases with increasing frequency for 0.1 M HCl, and rapidly decreases with increasing frequency for 3 M HCl.

Figure S9 shows that the effect of NaCl electrolyte concentration on twistron performance for tensile energy harvesting is similar to those demonstrated for HCl electrolyte concentration. In this case, a NaCl concentration between ~0.6 M NaCl and ~3 M NaCl maximizes both peak power output and output energy per cycle for 1 Hz deformation to 30% strain. Like for the case of HCl, the percent capacitance decrease with 30% tensile strain increase (~40%) depends little on NaCl concentration, but the increase of capacitance at zero strain on increasing NaCl molarity (from 0.35 F/g at 10^{-3} M to 4.56 F/g at 5 M) means that the capacitance change that is potentially available for energy harvesting monotonically increases with NaCl molarity. Decreasing NaCl concentration results in increased electrolyte resistance, and likely the increased load-matching resistance shown in Fig. S9A. However, this resistance is largely independent of NaCl concentration in the concentration range where both peak power (Fig. S9A) and energy per-cycle (Fig. S9B) are maximized for 1 Hz tensile deformation.

Figure S10 shows the frequency dependence of peak power, average power, and per-cycle energy output for tensile energy harvesting using a coiled twistron yarn in 0.6 M NaCl electrolyte. As the frequency of the applied sinusoidal deformation to 30% strain increased, peak power and average power increased until reaching plateaus at about 6 Hz, where the peak power is 90 W/kg and the average power is 30 W/kg.

Figure S11 shows the time dependence of output voltage, instantaneous power, and integrated output power for harvesting the mechanical energy from a 12 Hz stretch to 50% by using a coiled twistron harvester in 0.1 M HCl. Fig. S12 shows the results of electrochemical impedance spectroscopy for this twistron yarn for applied strains of 0% and 30%.

4.5. The effect of temperature on the tensile harvester performance of a coiled cone-spun yarn

Figure S13 shows the temperature dependence of per-cycle harvested energy, capacitance at zero strain, and fractional capacitance change for tensile energy harvesting in 0.6 M NaCl and in 0.1 M HCl. A 1 Hz sinusoidal stretch to 10% tensile strain was applied to the coiled harvester electrode. A three-electrode system was deployed that comprised the harvester electrode, a Pt mesh/MWNT buckypaper counter electrode, and an Ag/AgCl reference electrode. The reference electrode was in a separate beaker at room temperature, and connected by a KCl salt bridge to a beaker containing the other electrodes. Capacitances were measured using a scan rate of 50 mV/s and a scan range of 0.3 V to 0.6 V with respect to the reference electrode.

Figure S13 shows that the per-cycle harvested energy (and therefore the average power), the capacitance at zero strain, and the fractional capacitance change of a coiled yarn during stretch only weakly depend on temperature. Also, the maximum power and the load that maximizes power varies little with temperature.

4.6. The effect of an external bias potential on the tensile harvester performance of a coiled cone-spun yarn in an aqueous electrolyte

As shown in Fig. 3C, 0.1 M HCl electrolyte provided a higher intrinsic bias voltage than do 0.1 M HBr, 6 M NaCl, or 0.1 M KOH electrolytes. As a result of this high self-bias voltage, the open circuit potential of the coiled nanotube yarn (vs. Ag/AgCl) increased with increasing strain from 0.40 V to 0.55 V during 30% stretch. The question that we want to now address is whether an additional applied bias voltage will increase the net energy (output energy, reduced by the input energy required for electrical biasing) that can be harvested. Figure S14 shows the effect of applying an external bias potential between the counter and working electrode while a 0.2 Hz square-wave stretch of 20% was applied to a coiled twistron harvester. These results show that the per-cycle net output electrical energy increased from 17.9 J/kg with no externally applied bias to 27.1 J/kg when an additional 300 mV was applied. However, the opportunity in aqueous electrolytes to more dramatically improve performance is limited by electrolyte hydrolysis. In fact, even self-biasing (using chemical charge injection in 0.1 M HCl) results in a harvester electrode potential that increases from 0.40 V to 0.55 V (vs. Ag/AgCl) during 30% stretch, which is near the potential at which hydrolysis occurs.

For comparison with these results, Fig. S15 shows the effect of pH on the strain dependence of the difference in OCV and the potential of zero charge. The inset shows that the open circuit voltage of the harvesting electrode decreases linearly with increasing pH. The slope of this voltage dependence is -47 mV per pH unit, which is reasonably close to the -59 mV per pH unit that is predicted by the Nernst equation.

4.7. The effect of decreasing twistron resistance on twistron performance

Figure S16, which complements the results of Fig. 4F, shows that the peak output power can be increased to 250 W/kg (1.91 times that for the pristine yarn) by coiling a 25- μm -diameter Pt wire with a coiled MWNT yarn. This improvement is a consequence of decreasing the resistance of the harvester resistance and, correspondingly, the load resistance that optimizes powput. As shown in Fig. S17, incorporation of a coiled Pt wire

has little effect on the stress-strain curve of a twistron harvester during 0.2 Hz sinusoidal stretch to 15% strain in 0.1 M HCl.

4.8. Comparison of the performance of single-ply and four-ply coiled cone-spun yarns for tensile energy harvesting

Figure S18 compares the performance of a single-ply coiled twistron yarn and a four-ply coiled twistron yarn when operated at 1 Hz in 0.1 M HCl. While the impedance-matching load is four times higher for the single coiled yarn (400 ohm) than for the four times heavier 4-ply coiled yarn (100 ohm), the single ply yarn and the 4-ply yarn provide similar peak voltage changes for an impedance matched load (56 and 50 mV, respectively), similar gravimetric output energy per cycle (12.4 J/kg and 11.0 J/kg, respectively), and similar gravimetric peak output power (41 W/kg and 36 W/kg, respectively).

5. Torsional Twistron Harvesters

5.1. Effect of using isobaric and isometric load during torsional energy harvesting using twisted, cone-spun yarns

Figures 2C and S20 show that twist insertion decreases the electrochemical capacitance, thereby increasing the open circuit voltage of the twistron harvester. These changes in capacitance and OCV fully reverse upon untwist. However, while the twist dependence of capacitance change has little or no hysteresis (for the used 0.004 Hz for both isometric and isobaric measurements), the changes in open-circuit voltage are hysteretic. If the deformation frequency used for the open circuit measurements (0.16 Hz for isometric measurements and 0.088 Hz for isobaric measurements) is decreased, this hysteresis in open circuit voltage largely disappears.

For twist insertion that does not cause coiling, results for a 359- μm -diameter yarn (Fig. 2C) and a 208- μm -diameter yarn (Fig. S20) show that the OCV change for isometric (constant length) twist-untwist processes (86.8 mV) is about twice that for isobaric (constant force) twist processes (43.6 mV), despite the fact that the twist that could be inserted before yarn damage (~425 turns/m) for the isometric process was much smaller than the twist that could be inserted before yarn coiling for the isobaric process (~1,200 turns/m). The smaller diameter for the yarn used for isometric twist explains only part of this twist difference, since the effect of twist on yarn structure scales as the product of yarn diameter and yarn twist and this product is 0.153 and 0.250 for the isometric and isobaric processes, respectively. The above higher OCV change for the isometric process leads to higher torsional energy harvesting per cycle for the isometric process than for the isobaric process.

5.2. Effect of twisting speed, twisting amount, and electrolyte on the energy harvesting of cone-spun yarns

Figure S21 results for an isobaric load show that the speed of untwisting and retwisting has little influence on the generated OC voltage, when the degree of inserted twist was kept constant (from 0 turns/m to 2,000 turns/m for the investigated non-coiled, 170- μm -diameter, MWNT yarn in 0.1 M HCl electrolyte). However, Fig. S21 results show that the hysteresis of the OCV decreases with decreasing twisting speed.

Figure S22 shows that average output power for torsional energy harvesting using non-coiled harvesters is higher for the 0.1 M HCl electrolyte than for the 0.6 M NaCl

electrolyte, which is also the case of energy harvesting using the stretch of a coiled twistron yarn (Fig. S8 and S9). The average output power reached a plateau of 6.3 W/kg when the twisting speed in 0.1 M HCl was 1,680 rpm. For comparison, the average output power for the 0.6 M NaCl electrolyte reached a plateau of 4.3 W/kg for the same twisting speed.

While the above results of Figs. S21 and S22 are for torsional energy harvesting using MWNT yarns that are not coiled or partially coiled during twist insertion, Fig. S23 shows the dependence of capacitance and open-circuit voltage on twist for isobaric twist insertion and removal that goes all the way from the non-twisted yarn to the fully coiled yarn and then back to the non-twisted yarn. These results for capacitance change (top panel) show that capacitance monotonically decreases with twist insertion and monotonically increases with twist removal, and that the dependence of capacitance on twist level is hysteretic for twist levels where coils exist during either twist insertion or twist removal. However, the bottom panel shows that there is little change in open-circuit voltage once coiling starts during twist insertion (and, hence, little opportunity for energy harvesting). On the other hand, the open-circuit voltage monotonically decreases as soon as twist removal begins, so that energy harvesting can be accomplished during the entire twist removal process from the fully coiled yarn.

Twisting beyond the twist which causes complete yarn coiling also increases yarn density, decreasing capacitance and resulting in generated voltage, as seen in Fig. S23 for high degrees of twist. However, this occurs by decreasing coil diameter, thereby decreasing the coil spring index, which will eventually result in yarn failure, and is therefore not very useful for energy harvesting.

5.3. The effect of temperature on the torsional harvester performance of a twisted cone-spun yarn in 0.6 M NaCl

Figure S24A shows, for torsional energy harvesting in 0.6 M NaCl, that the per-cycle harvested energy, the capacitance at zero strain, the peak-to-peak open circuit voltage, and the fractional capacitance change of a coiled yarn during stretch only weakly depend on temperature. Figure S24B provides the analogous results for torsional energy harvesting in 0.1 M HCl. Although the electrical energy harvested per cycle is smaller in 0.6 M NaCl than in 0.1 M HCl (when the twistron type and diameter, and the twist insertion and removal conditions are identical), the HCl and NaCl electrolyte results are similarly insensitive to temperature.

These observations for torsional energy harvesting (and related observations in Fig. S13 for tensile energy harvesting) can be understood, since the PZC is essentially independent of temperature (Fig. 3D), and the open-circuit voltage at zero strain only depends on the pH of the electrolyte. Using empirical correlation developed by Fujishiro *et al.* (40), the pH of the 0.1 M HCl electrolyte should only change from 1.10 at 0 °C to 1.13 at 50 °C, which (according to the Nernst equation) would only produce a 1.8 mV change in the open-circuit voltage at zero strain. In addition, it is known that the capacitance of porous electrodes wetted by aqueous electrolytes typically varies modestly with temperature (40), which is consistent with the present measurement results. Finally, electrochemical impedance spectroscopy in 0.1 M HCl (between 100,000 and 0.1 Hz) show that the cell resistance at 100,000 Hz varies little with temperature (from 9.9 ohm at 0 °C to 5.8 ohm at 50 °C).

5.4. Performance comparisons for torsional energy harvester yarns that are cone spun and dual-Archimedean

Figure S25 compares the torsional harvester performance (in 0.1 M HCl) of twisted yarns made using the cone-spinning and dual-Archimedean-spinning processes, when twisted and untwisted under an isobaric load of 43 g. Despite using the same number of sheets in the sheet stacks, identical width and length sheets ($4.5 \times 30.7 \text{ cm}^2$), and nearly the same inserted twist to make the twisted yarn (2,580 turns/m for cone spinning and 2,530 turns/m for dual-Archimedean spinning, when normalized to sheet length), the diameters of the twisted yarns and the yarn densities were different for the cone-spun yarn (140 μm and 1.293 g/cm^3) and the dual-Archimedean yarn (168 μm and 1.203 g/cm^3). For measurements of torsional energy harvesting on both yarns, the inserted twist and removed twist during torsional energy harvesting was 357 turns/m and the twist insertion and removal speed was 60 rpm. Use of such slow twisting speeds resulted in low power densities. Upon twist insertion, the capacitance of the cone-spun yarn decreased from 5.99 F/g to 4.91 F/g, corresponding to a capacitance change of 18%. The corresponding capacitances for the dual-Archimedean yarn are 6.56 F/g and 5.88 F/g, which provide 10.3% change of capacitance during twist insertion.

Figure S25 shows that the average power and peak voltage during twist insertion and twist removal were much higher for the cone spun yarn than for the dual-Archimedean-spun yarn. Despite the similar CNT weight per yarn length for the cone-spun yarn (199 $\mu\text{g/cm}$) and the dual-Archimedean yarn (267 $\mu\text{g/cm}$), the load resistance that maximized power output was about two times higher for the cone-spun yarn than the dual-Archimedean yarn.

Upon increasing the twisting speed for twist insertion and twist removal from 60 rpm to 1,800 rpm for the above cone-spun yarn, operated isobarically using a 43 g load, the average output power increased from 0.38 W/kg to 6.0 W/kg (Fig. S22A). When using 0.6 M NaCl as the electrolyte, the average output power for this cone-spun yarn was 0.2 W/kg at 60 rpm and 4.39 W/kg at 1,800 rpm (Fig. S22B). A motor acceleration of 12,500 turns/s² was used, so these rotation speeds were realized effectively instantaneously (within 4.8 ms for 60 rpm and 144 ms for 1,800 rpm).

6. Dual Harvesting Electrode Twistrons, Bath-Free Twistrons, and Twistron Applications

6.1. A seesaw configuration for utilizing twistron harvesters for both anode and cathode

Figure S26 illustrates the “seesaw” configuration, which enables increase in power output per total electrode weight by using identical twistron yarns for both electrodes, and stretching and releasing these electrodes 180° out-of-phase. Figure S27 shows that 180°-out-of-phase stretching of both electrodes generates a maximum open-circuit, inter-electrode voltage of about 257 mV, which is about two times larger than when only one electrode is mechanically stretched (132.4 mV). Figure S28 shows that 180°-out-of-phase stretching generates a short-circuit current of about 327 A/kg, which is two times larger than when only one electrode is mechanically stretched (162 A/kg). Based on the total weight of both electrodes, the average output power is ~3.4 times higher for stretching both yarns out-of-phase, versus stretching only a single yarn. This increase is smaller than the theoretically predicted factor of 4, potentially because of the existence of some yarn snarling.

6.2. Performance and textile application of gel electrolyte used for making a solid-state harvester yarn that comprises both working and counter electrodes

Except for harvesting the mechanical energy of ocean waves or organs within the body, elimination of the electrolyte bath is important for most applications of the twistron yarns. Ideally, both device electrodes should be twistron yarns that are combined in a single yarn that is a solid-state harvester, like for the devices of Fig. 2D and Fig. 4A. In order to electronically insulate the opposite electrode yarns, while keeping them ionically connected, we overcoated these yarns with polyvinyl alcohol gel that contains the 0.1 M HCl electrolyte. Figure S29 shows that such yarn coating does not significantly affect the CV curve for the coiled yarn or the dependence of peak power and peak output voltage on load resistance. To mitigate the water evaporation that can occur in low humidity environments with such PVA/HCl electrolytes, we also produced harvester yarns that used a hygroscopic LiCl gel electrolyte (10 wt% PVA/4.5 M LiCl) (Fig. 4B), as well as harvester yarns that were coated with a thin layer of polyurethane (Fig. S30).

6.3. A dual-electrode twistron harvester comprising a self-coiled MWNT yarn that generates electrical energy and a MWNT yarn counter electrode

Figure S30 is a SEM micrograph of a dual-electrode tensile energy harvester yarn in which a polyurethane-coated, non-coiled, twisted MWNT yarn was wrapped around a self-coiled MWNT yarn, which does the energy harvesting. The deployed polyurethane (PU) (Hydromed D4, from AdvanSource Biomaterials) is hydrophilic. Though this PU is not ionically conducting in the dry state, it expands as it absorbs up to 50 wt% water, allowing the free flow of ions, like expected for a hydrogel.

6.4. Self-powered tensile strain sensor for monitoring breathing

Figure S31 and Movie S1 show the application of a dual-electrode harvester as a self-powered sensor for monitoring breathing. Unlike for the dual-electrode yarn of Section 6.03, one electrode is homochiral and the other is heterochiral, so both contribute to harvesting the mechanical energy of chest expansion. The preparation of this harvester is described in Section 1. The harvester electrodes were sewn into a sports shirt, purchased from Ellesse, and then overcoated with a 10 wt% PVA/HCl electrolyte, where the HCl concentration was 0.1 M. This self-powered sensor provides a 16 mV voltage change when stretched by ~10% during breathing.

6.5. Environmental thermal or chemical energy harvesting using twistron yarns

Figure 4E shows that thermal energy can be harvested as electrical energy by attaching a thermally powered nylon artificial muscle to a coiled twistron harvester, and torsionally and translationally tethering opposite device ends. Since coiled hybrid CNT muscles can provide large reversible tensile strokes (depending upon the yarn guest) when heated or exposed to chemicals or humidity, the coiled nylon muscle can be replaced with a coiled hybrid CNT muscle in order to harvest energy from temperature changes, humidity fluctuations, or chemical waste streams (21, 41, 42). Upscaling can be conveniently accomplished by operating many of these harvesters in parallel.

Our torsional energy twistron harvesters are uniquely capable of operating as self-powered sensors of torsional motion, but would be difficult to upscale by increasing the number of harvesting yarns, since each twistron yarn must be twisted. Even here there is

an opportunity for upscaling to harvest the energy from fluctuations in ambient temperature or humidity, since each twistron harvester in a harvester array could be driven by a hybrid carbon nanotube yarn muscle or a polymer fiber muscle that converts ambient temperature or humidity fluctuations to mechanical torsional energy.

7. Structural, Density, and Capacitance Data for Twistron Yarns and Precursor CNT Sheets

TEM images of axial cross-sections of twisted yarns (Figs. S32-S35 and Fig. 5A and B) show that the bundled MWNTs in twistron yarns partially collapse in an unexpected way. One would normally anticipate, as is observed for other CNTs (33, 34), that large-diameter MWNTs having sufficiently small number of walls would individually collapse to gain van der Waals energy for the inner wall of the inner-most nanotube. While this process occurs to some extent, we found that nanotubes in the MWNT bundles primarily deform so that they can increase inter-nanotube van der Waals energy (Figs. S32-S35 and Fig. 5A and B), and that such deformation occurs even in non-twisted yarn. Despite the associated decrease in void space within bundles, analysis of these TEM micrographs (Section 8) will show that sufficient void space exists, even in these relatively well ordered bundles, for hydrated H₃O⁺ ions, and that the associated capacitance (assuming that this void-space is electrochemically accessible) is significant.

Yarn density and yarn diameter were measured as a function of inserted twist for a constant load applied during twist insertion (6 g, which corresponds to an engineering stress of 31.2 MPa for the highly-twisted 49-μm-diameter yarn). As inserted twist increased from 1,107 to 5,093 turns/m, yarn density increased from 0.64 to 1.28 g/cm³ and yarn diameter decreased from 62 to 49 μm. For isometric twist insertion, Fig. S36 shows the dependence of percent volume change and yarn diameter on inserted twist (in 0.1 M HCl) for a cone-spun yarn that was twisted to below the point where yarn fracture occurs. Subsequent untwist reversed volume and yarn diameter to original values without substantial hysteresis.

8. Structure-Based Analysis of Capacitance and Twist-Induced Capacitance Changes for Twistron Yarns

8.1. Calculation goals and issues

We want to understand the origin of the electrochemical capacitance of the carbon nanotube yarns and the twist-induced changes in this capacitance. In efforts to accomplish this, we will first use TEM, STEM, and SEM microscopy to characterize the structure of individual MWNTs and the ratio of total bundle area to total bundle volume. From this information, we will calculate the gravimetric capacitance that would result if the MWNTs were completely non-bundled, as well as the gravimetric capacitance predicted if the only surface area contributing to capacitance was the surface area of nanotube bundles.

In order to calculate electrochemical capacitance of a twistron harvester yarn from the structurally-derived surface area of non-bundled MWNTs, bundled MWNTs, and intra-bundle void space, we used the reported areal capacitance of the basal plane of graphite (~4 μF/cm²) (29, 30), which is expected to be similar to that of MWNTs.

The measured areal capacitance of the basal plane of graphite in 0.9 M NaF at the potential of zero charge (PZC) is ~3 μF/cm² and that value linearly increases up to ~4 μF/cm² at the potential around +0.4 V with respect to the PZC (29). Similar capacitances are also observed for the basal plane of graphite in 0.5 M H₂SO₄ and 1 M NaOH (30). The

measured areal capacitance of carbon single wall nanotubes in 1 M NaCl is $\sim 5 \mu\text{F}/\text{cm}^2$ (31). The measured areal capacitance of 5-layer graphene in 6 M KOH at the potential of zero charge (PZC) is $\sim 3 \mu\text{F}/\text{cm}^2$ and that value linearly increases up to $\sim 4 \mu\text{F}/\text{cm}^2$ for a +0.4 V potential with respect to the PZC (43).

It is not surprising that the above-reported electrochemical capacitances of carbon electrodes in aqueous solution do not significantly depend on the types of ions, since the sizes of hydrated ions are all similar. For example, the radii of hydrated H_3O^+ , Na^+ , OH^- , and Cl^- are 2.82 Å, 3.58 Å, 2.46 Å, and 3.32 Å, respectively (44). Considering that the operation voltage of a twistron harvester ranges from ~ 0.3 V to ~ 0.7 V with respect to PZC, assuming that the areal capacitance of MWNTs is $\sim 4 \mu\text{F}/\text{cm}^2$ is a reasonable approximation.

We first hypothesized that yarn capacitance predominantly arose from the external surface area of CNT bundles and that the capacitance change upon twist-insertion resulted from compressing together the electrochemical double layers on CNT bundles. While we will show that yarn capacitance predominantly arises from the external surface area of CNT bundles, a problem arises in this explanation for the origin of capacitance change, since the CNT bundles in the yarns are typically separated by a much larger distance than the thickness of an electrochemical double layer (~ 1.3 nm for 0.1 M HCl and ~ 0.7 nm for 0.6 M NaCl) (45).

8.2. Capacitance calculated for the hypothetical case where MWNTs are non-bundled and well separated

The gravimetric surface area was calculated for hypothetical, isolated, non-bundled MWNTs by using TEM images along the yarn direction to provide the numerical distribution of MWNTs that have a specific outer diameter and number of walls. Exploiting this distribution and calculated results for the surface area and weight of MWNTs (46), the weight-averaged density of the MWNTs is $1.595 \text{ g}/\text{cm}^3$, the volume-averaged surface-to-volume ratio of the MWNTs is $370 \text{ m}^2/\text{cm}^3$, and the gravimetric surface area of non-bundled nanotubes is $242 \text{ m}^2/\text{g}$. As for all of the following calculations, the areal capacitance for the basal plane of graphite ($\sim 4 \mu\text{F}/\text{cm}^2$), which is similar to the $\sim 5 \mu\text{F}/\text{cm}^2$ of single-wall carbon nanotubes, was used to convert gravimetric surface area to gravimetric capacitance. The result obtained was surprising – the calculated gravimetric capacitance for isolated MWNTs (9.7 F/g) was of similar size to, albeit larger than, the capacitance shown in Fig. S21 for untwisted MWNT yarn. These results suggest that the largely bundled MWNTs in the yarns are able to access high gravimetric capacitances by providing a combination of high gravimetric bundle surface area (due to non-circular cross sections) and intra-bundle capacitances.

8.3. Gravimetric capacitance due to MWNT bundle surfaces

Although we will later show that this approach seriously underestimates this capacitance, the volumetric capacitance due to the total surface area of MWNT bundles in the twistron yarns was initially estimated from measurements of bundle diameter and length from SEM micrographs of MWNT sheets that are precursor to the nanotube yarns. The approximation was made that the bundle size for the sheet (which was densified by ethanol absorption and evaporation) was the same as for bundles in the twisted yarns. If $F(d_i)$ is the length-weighted fraction of MWNT bundles that have a particular projected

diameter (d_i) and the bundles were cylindrical, the total bundle area per total bundle volume becomes $4\sum d_i F(d_i)/\sum d_i^2 F(d_i)$, where summations are over the observed bundle diameters. The corresponding total bundle area per total bundle weight is then $(4/\rho_{\text{bundle}})\sum d_i F(d_i)/\sum d_i^2 F(d_i)$, where ρ_{bundle} is the ratio of the weight of a bundle to its volume, which we approximate by the above-derived weight-average MWNT density (1.595 g/cm³). From lateral SEM images of forest-drawn sheets, this analysis provides a gravimetric surface area of 36.6 m²/g for MWNT bundles. Using the capacitance per surface area that is experimentally measured for graphite, the electrochemical double layer capacitance predicted from the surface area of MWNT bundles is 1.46 F/g.

Since we know from present TEM and STEM microscopy (Figs. S32-S35) and previous results (47) that the bundles in forest-spun MWNT yarns are far from cylindrical, the above evaluation provides a lower bound on volumetric surface area and on the thereby derived gravimetric capacitance. Hence, we can more reliably determine the ratio of total bundle surface area to bundle volume by using TEM images to analyze 150-nm-thick cross-sections normal to the yarn axis. Using this volumetric surface area (178 m²/cm³), the weight-average gravimetric surface area for these bundles that is obtained from TEM micrographs (assuming an intra-bundle density of 1.595 g/cm³) is 112 m²/g. This gravimetric surface area provides a capacitance contribution of 4.48 F/g if an areal capacitance of ~4 μF/cm² is used (corresponding to the areal capacitance of the basal plane of graphite).

Since the STEM images have sufficient resolution for excluding the core volume of the deformed MWNTs in the bundles, another estimate for the density within a bundle can be obtained from the total bundle volume that is occupied by carbon and the density of graphite (2.26 g/cm³), which provides an average bundle density of 0.58 g/cm³. Using the volumetric surface area obtained from these images (178 m²/cm³), the calculated gravimetric surface area and gravimetric capacitance are 78.8 m²/g and 3.15 F/g, respectively.

8.4. Gravimetric capacitance due to intra-bundle porosity

In order to experimentally evaluate the possibility that intra-bundle porosity contributes to gravimetric capacitance, we examined the cross-section of a twistron yarn that had been cycled 40 times between 0.3 and 0.6 V by using cyclic voltammetry. This yarn was then frozen with liquid nitrogen and subsequently freeze-dried to lock-in the salt distribution, while preventing the aggregation of large salt crystals. Results obtained from high-angle annular dark field (HAADF) STEM images (Fig. S33), which are especially sensitive to atomic number differences between carbon and sodium/chlorine, show a degree of sodium chloride penetration between MWNTs in bundles, as well as accumulation at the corners of MWNTs. Evidence that the penetrating material includes Cl⁻ is found by electron energy loss spectroscopy (Fig. S34).

We next theoretically estimated the capacitance changes during twist insertion/deinsertion due to changes in electrochemically accessible surface area of void space within MWNT bundles. To accomplish this, empirical force field molecular dynamics simulations were used to model the cross-section of MWNT bundles. The interatomic interaction was described by the adaptive intermolecular reactive empirical bond order potential, modified with a Morse potential (48). In these isothermal-isobaric molecular dynamics simulations, the temperature was maintained at around 300 K, as

implemented in LAMMPS code (49). We considered a unit cell that consists of thirty-four vertically (z -axis) aligned multi-walled carbon nanotubes with periodic boundary conditions. For realistic representation of twistron yarns, we used the distribution of diameter and number of walls from a TEM image of a yarn cross section (Fig. S35). The constituent MWNTs have outer diameters ranging from 6.3 nm to 11.7 nm (9.0 nm in number average) and inner diameters ranging from 1.9 nm to 9.1 nm (4.4 nm in number average), with the number of walls ranging from 6 to 10 (7.9 in number average). Figure S37A and Fig. S37B show bundle structures obtained by molecular dynamics simulations for a twist-induced 50 MPa lateral pressure and zero applied pressure, respectively.

Intra-bundle pores that are sufficiently large to accommodate electrolyte ions can contribute to the electric double-layer capacitance, as long as these pores are ionically connected to the bulk electrolyte. In order to estimate the intra-bundle surface area that is accessible to hydronium ions for the investigated bundle, we used a probing sphere of radius 4.5 Å (which corresponds to the sum of the carbon van der Waals radius, 1.7 Å, and the solvated hydronium ion radius, 2.8 Å). Using projections of MWNT structure in the yarn direction and thereby derived van der Waals surfaces, this probing sphere indicated that there was 65.9 m²/g of intra-bundle surface area that could be occupied by solvated hydronium ions. Using the areal capacitance of the basal plane of graphite (~4 µF/cm²), this gravimetric surface area provides 2.6 F/g of capacitance. Using the dimensions for solvated Cl⁻, analogous calculations provide a gravimetric capacitance contribution of 2.3 F/g.

During operation of a twistron harvester, the MWNT bundles in the twistron yarn are under tensile and torsional loads, generating compressive pressures on MWNTs inside the yarn. We here approximate the compressive pressure to be biaxial and perpendicular to the axis of the MWNT bundle. The increase of the lateral pressure on MWNT bundles by twisting or stretching the yarns can lead to decrease of capacitance due to the decreased intra-bundle porosity. In our molecular dynamics simulations, the intra-bundle surface area of MWNT bundle, estimated by a probing sphere of radius 4.5 Å, decreases from 65.9 m²/g to 47.2 m²/g, as the compressive lateral pressure on the bundle increases from 0 to 50 MPa (Fig. S37). At least, for small MWNT bundles containing around 9 MWNTs, where computational times were tractable, this decrease in capacitance occurred reversibly. Using the areal capacitance of the basal plane of graphite (~4 µF/cm²), the estimated gravimetric capacitance from the intra-bundle surface area decreases from 2.6 F/g to 1.9 F/g as the lateral stress increases from 0 to 50 MPa (Fig. S38). Using the dimensions for solvated Cl⁻, analogous calculations provide a gravimetric capacitance contribution of 2.3 F/g at 0 MPa and 1.5 F/g at 50 MPa of lateral pressure.

The next calculations show that the lateral stress on MWNTs during twistron harvester operation can even exceed the above 50 MPa. The relationship between the internal pressure and the tensile and torsional loads on the yarns can be approximated by using a simple helix model for the yarn geometry. The bias angle (the angle between yarn length and nanotube orientation direction) for the yarn is $\alpha = \tan^{-1}(2\pi rt)$, where r is the distance from yarn center and t is the inserted twist in turns per yarn length (called the twist density). Using this equation, the average bias angle (α_{ave}) along the radius is:

$$\alpha_{ave} = \int_0^{R_0} \tan^{-1}(2\pi rt) dr / R_0 , \quad (S1)$$

where R_0 is the radius of the yarn. The tensile stress σ and shear stress τ in the yarn cross-section under tensile force S and torque T is $\sigma = S/\pi R^2/2$ and $\tau = \tau_{\max}r/R$, respectively, where $\tau_{\max} = 2T/\pi R^3/3$. Thus, two forces, $F_1 = \sigma d_0^2$ and $F_2 = \tau d_0^2$, contribute to the tensile force $F = F_1 \cos \alpha_{\text{ave}} + F_2 \sin \alpha_{\text{ave}}$ on nanofiber bundles in the yarn, where d_0 is effective diameter of the bundles. An element of the bundle at radius r with length $r\theta$, where θ is infinitesimal, is used for further analysis. The tensile force F in this element, shown in Fig. S39, has a lateral force component in the radial direction of the yarn of:

$$2F \sin \theta = 2d_0^2 [\sigma \cos \alpha_{\text{ave}} + (r/R)\tau_{\max} \sin \alpha_{\text{ave}}] \sin \theta. \quad (\text{S2})$$

Upon integration of Eqn. S2 from R_0 to r , the total lateral force at radius r is:

$$F_{\text{total}} = 2[\sigma \cos \alpha_{\text{ave}} + 0.5(r/R+1)\tau_{\max} \sin \alpha_{\text{ave}}] \sin \theta d_0^2 (R-r)/d_0. \quad (\text{S3})$$

The effective area that total lateral force acts upon at radius r is $A = 2r\theta d_0$. Hence, the lateral pressure is:

$$\sigma(r) = F_{\text{total}} / A | \theta \rightarrow 0 = [\sigma \cos \alpha_{\text{ave}} + 0.5(r/R+1)\tau_{\max} \sin \alpha_{\text{ave}}] \times \frac{(R-r)}{r} \quad (\text{S4})$$

and the volume-average lateral pressure is:

$$\sigma_{\text{lateral}}^{\text{ave}} = \int_0^V \sigma(r) dV / V = \sigma \cos \alpha_{\text{ave}} + \frac{2}{3} \tau_{\max} \sin \alpha_{\text{ave}}. \quad (\text{S5})$$

In order to evaluate Eqn. S5, we used experimental measurements of yarn torque as a function of twist density. Using a typical yarn diameter of 36 μm and a typical applied engineering stress of 30 MPa, the dependence of average lateral pressure on twist density was obtained (Fig. S39). As shown here, the average lateral pressure in the yarn can exceed 50 MPa.

The observed highly-reversible changes in yarn capacitance likely result from elastic deformation of yarn structure across hierarchical scales, ranging from deformation of MWNT cross-sections and rearrangement of MWNTs within bundles to bundle coalescence. Bundle densification might be facilitated by mismatched lengths of different MWNTs within bundles and the observed forking and recombination of MWNT bundles having different lengths. Additionally, the MWNTs in large bundles are so irregularly packed that an individual MWNT likely meanders from side-to-side in a bundle. Twist-induced tension in a bundle might increase the packing density by decreasing this meandering, thereby decreasing the accessible intra-bundle capacitance.

8.5. Fraction of mechanically induced capacitance change that is used for mechanical energy harvesting

Conservation of effective charge at zero strain, $Q(0)$, on a mechanically twisted or stretched twistron yarn would mean that $Q(0) = V_m(0)C_m(0) = V_c(\varepsilon)C_m(\varepsilon)$, where $V_m(0)$ and $V_c(\varepsilon)$ are the measured and calculated open-circuit voltages (relative to the PZC) at 0 strain and strain ε , respectively, and $C_m(0)$ and $C_m(\varepsilon)$ are the measured gravimetric capacitances at 0 strain and strain ε , respectively. The ratio of the measured open-circuit voltage to the calculated open-circuit voltage provides the fraction of the strain induced capacitance change that is being used for energy harvesting.

Depending upon the particular CNT forest and twist-insertion method used for yarn preparation, only a fraction of the mechanically-induced capacitance change is used for harvesting electrical energy. Using OCVs relative to the PZC, this fraction is the ratio of

the product of OCV and the capacitance after twistron deformation to this product before deformation. Based on the OCV and capacitance data in Fig. 2C and Fig. 1D, the fraction of capacitance change that is useful for energy harvesting varies from 79.0% to 99.5% for torsional and tensile energy harvesters. This up to 21.0% of non-productive capacitance change is likely due to counter ions being trapped in void spaces that lose contact with the bulk electrolyte during twist, which prevents their associated charge from redistributing onto electrochemically-accessible surfaces to increase electrode voltage.

Using the experimental data in Section 5.01 for twist insertion and removal for twistron yarns that are operated isometrically and isobarically, the fraction of capacitance change that can be used for energy harvesting is 97.1% for isometric harvesting and 88.2% for isobaric harvesting.

9. Performance Comparison for Mechanical Energy Harvesters

We here compare the performance of twistron energy harvesters with other mechanical-to-electrical conversion technologies reported in literature, including piezoelectric, electrostatic, triboelectric, and dielectric-elastomeric harvesters. Only material-based harvesters are compared in Table S2 and in Fig. 5C and D, since the performance of electromagnetic generators (basically motors operated in reverse) degrades when scaled down to small weights and dimensions (and cost per Watt becomes prohibitive for many applications).

Data in the literature on mechanical energy harvesters frequently does not provide device mass (or volume and density) or specific power and specific energy, and the power and energy densities reported are often areal rather than volumetric or gravimetric. Also, many publications do not differentiate between peak power density and average power density or only provide peak power densities. Since so few publications provide average output power, Table S2 reports for literature results only harvester weight, maximum specific power, the frequency at which maximum power was realized, and the ratio of peak power to the frequency at which this peak power was realized. Since device performance depends on frequency and displacement, and sometimes temperature, we have taken the highest peak power density reported for a given architecture in the cited publication. For the rare publications in which average power was provided, but not peak power, we estimated peak power by multiplying average power by a factor of 2, which is theoretically predicted for sinusoidal waveforms if root-mean-square voltage and current were reduced from peak values by a factor of $2^{1/2}$.

Using the Table S2 results, as well as a curve that is a represents the low frequency triboelectric data of Zhang's group (36), Figs. 5C and 5D show peak power and frequency-normalized peak power, respectively, versus the frequency at which this peak power was obtained. For comparison, our twistron harvesters produce up to ~250 W/kg for the frequency range from 18 to 30 Hz, and can be operated at frequencies below 1 Hz. Both the specific energy per cycle and the peak specific power are higher than has been obtained for any microscale or macroscale material-based harvester device that is operated between a few Hz and 600 Hz.

10. Maximizing Power Output by Matching the Complex Impedance of the Harvester

Since all power measurements used a purely resistive load, maximum power was harvested when this resistive load (R_{load}) matched the harvester's impedance, $R_{load} = [R_{internal}^2 + 1/(\omega C)^2]^{1/2}$. However, since harvester capacitance causes a phase shift between OCV and SCC, the output electrical energy could be increased by matching the complex impedance of the harvester, instead of matching just its resistive component. This is challenging at low frequencies ($f = \omega/2\pi$) because the optimum inductance goes as $(4\pi^2 f^2 C)^{-1}$, and this inductance to counter the electrochemical capacitance (C) of short twistron yarn lengths can exceed tens of Henrys. Impedance matching through high-frequency, active power factor correcting circuits is fundamentally possible, but commercially-available integrated circuits cannot accommodate the voltages and currents provided by our harvesters. Since the measured phase angle between short-circuit current and open-circuit voltage was $\sim 73^\circ$ at 0.1 Hz and $\sim 61^\circ$ at 1 Hz for a coiled harvester during tensile stretch to 15% strain, power increases of 2.2 and 1.5 times, respectively, are predicted if improved electronic circuits for complex impedance matching were developed.

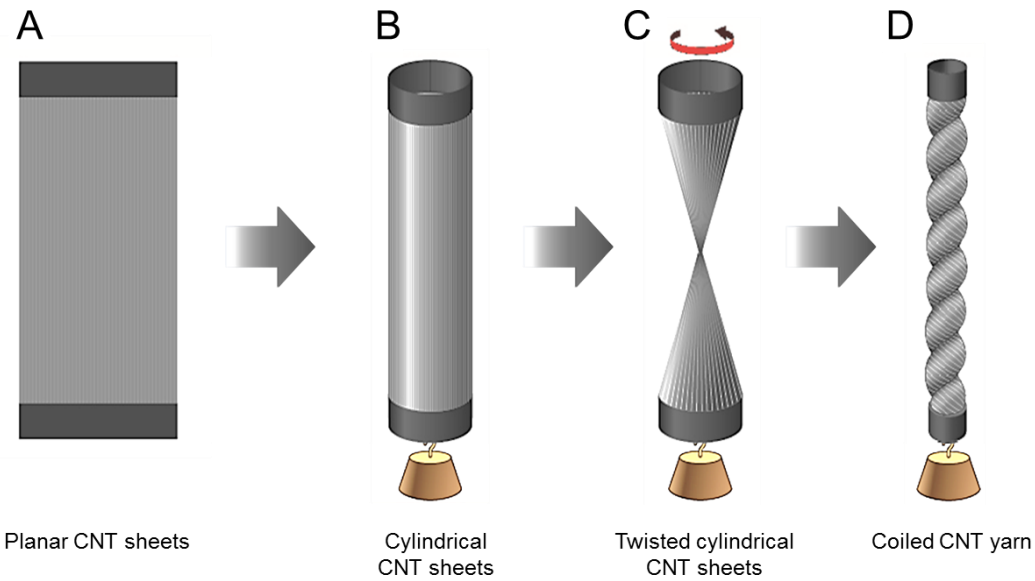


Fig. S1.

A stack of forest-drawn CNT sheets (**A**) was rolled into a cylinder (**B**) and twisted (**C**) under an applied load to produce a twisted yarn, which was subsequently twisted under the same applied load to produce a coiled twistron harvester (**D**).

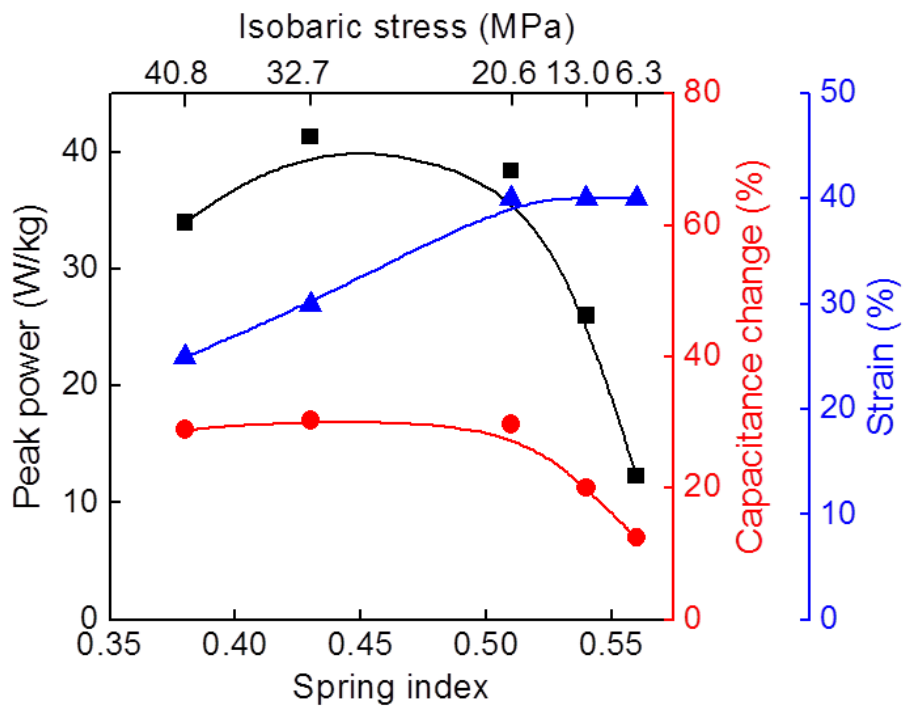


Fig. S2.

Peak output power (black squares), maximum measured capacitance change (red circles) and maximum reversible tensile strain (blue triangles) during tensile energy harvesting as a function of spring index and the applied isobaric stress (during the twist insertion that was used to obtain the spring index). These measurements (up to the maximum indicated strain for each spring index) were performed for 1 Hz stretching in 0.1 M HCl using coiled, cone-spun CNT yarns having a diameter of 58 μm prior to coiling. The coiled yarn having a spring index of 0.43 after fabrication provided the highest peak power (41.3 W/kg) and capacitance change (30.3%).

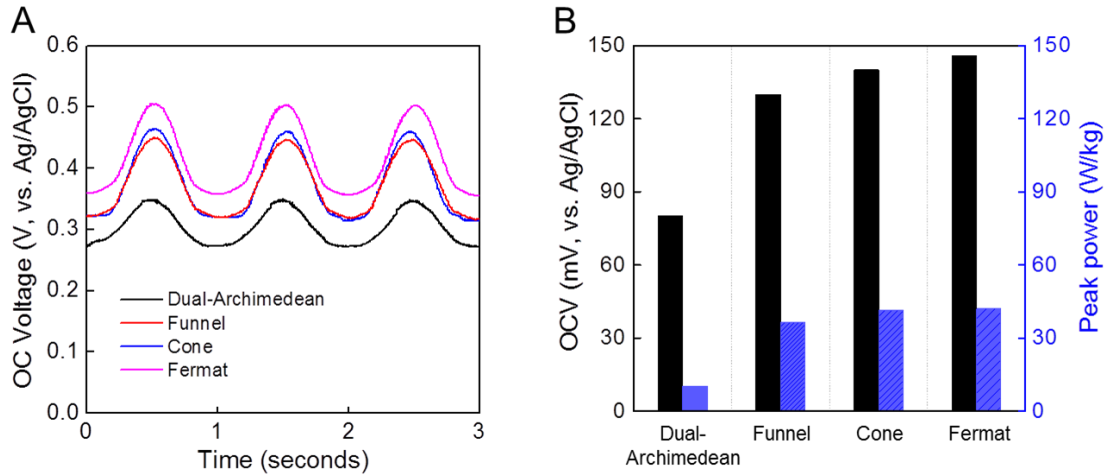


Fig. S3.

Comparison of the performance of differently spun coiled yarns when stretched to 30% at 1 Hz in 0.1 M HCl. **(A)** The time dependence of dual-Archimedean (black), funnel (red), cone (blue), Fermat (magenta), and wet-densified tow-spun (green) coiled yarns. **(B)** Comparison of the peak-to-peak open circuit voltage and the impedance-matched peak power for these different coiled yarns during stretch by 30% in 0.1 M HCl.

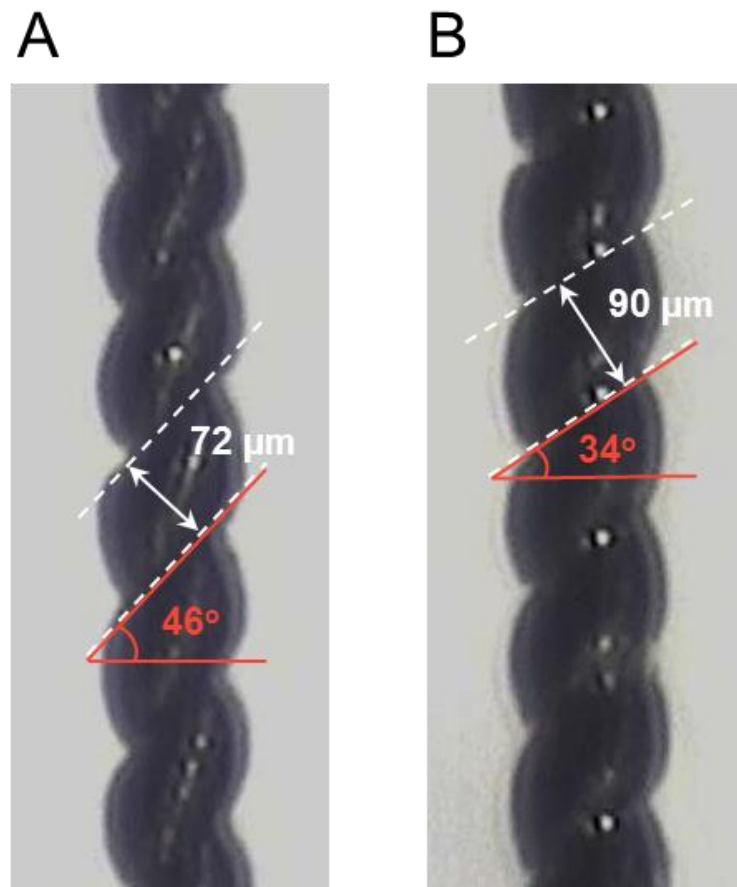


Fig. S4.

Photographs of a two-end positionally and torsionally tethered, coiled CNT yarn before (A) and after (B) immersion in 0.1 M HCl electrolyte. These photographs show that immersion in the electrolyte caused swelling, which increased the CNT yarn diameter (shown in white) from 72 μm to 90 μm and decreased the coil bias angle (shown in red) from 46° to 34° .

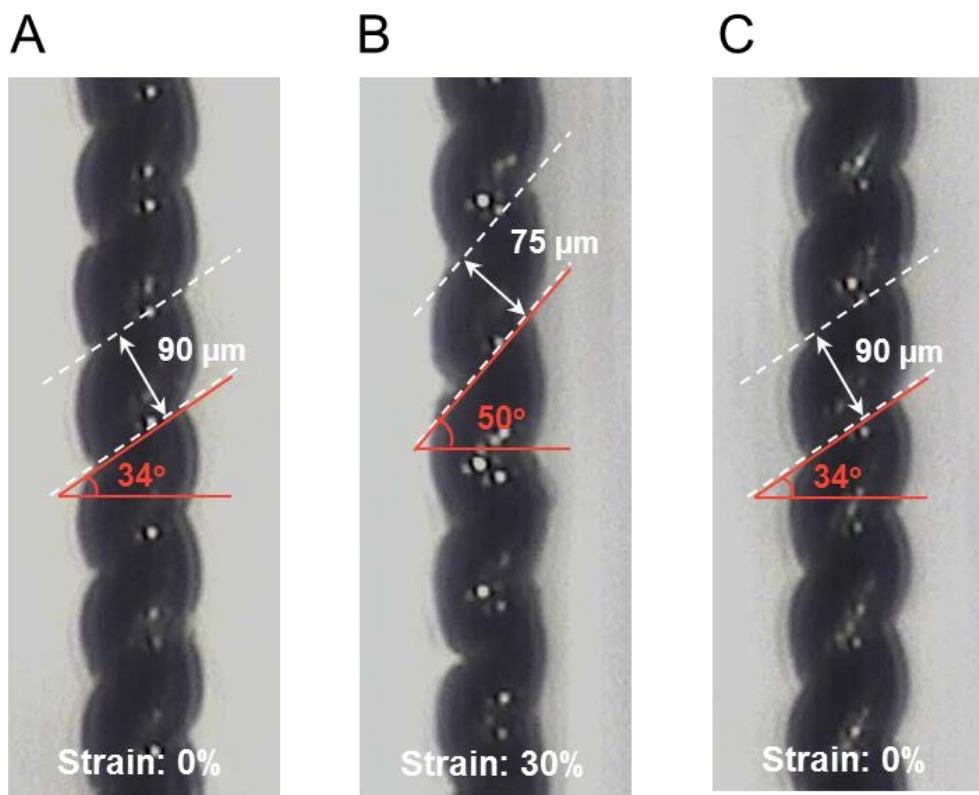


Fig. S5.

Photographs of a torsionally tethered, coiled CNT yarn during cycling in 0.1 M HCl between 0% and 30% applied tensile strain. Comparison of (A) and (B) show that 30% strain increases the coil bias angle from 34° to 50° and decreases the yarn diameter from 90 μm to 75 μm . (C) shows that the original yarn diameter and coil bias angle are obtained upon strain release.

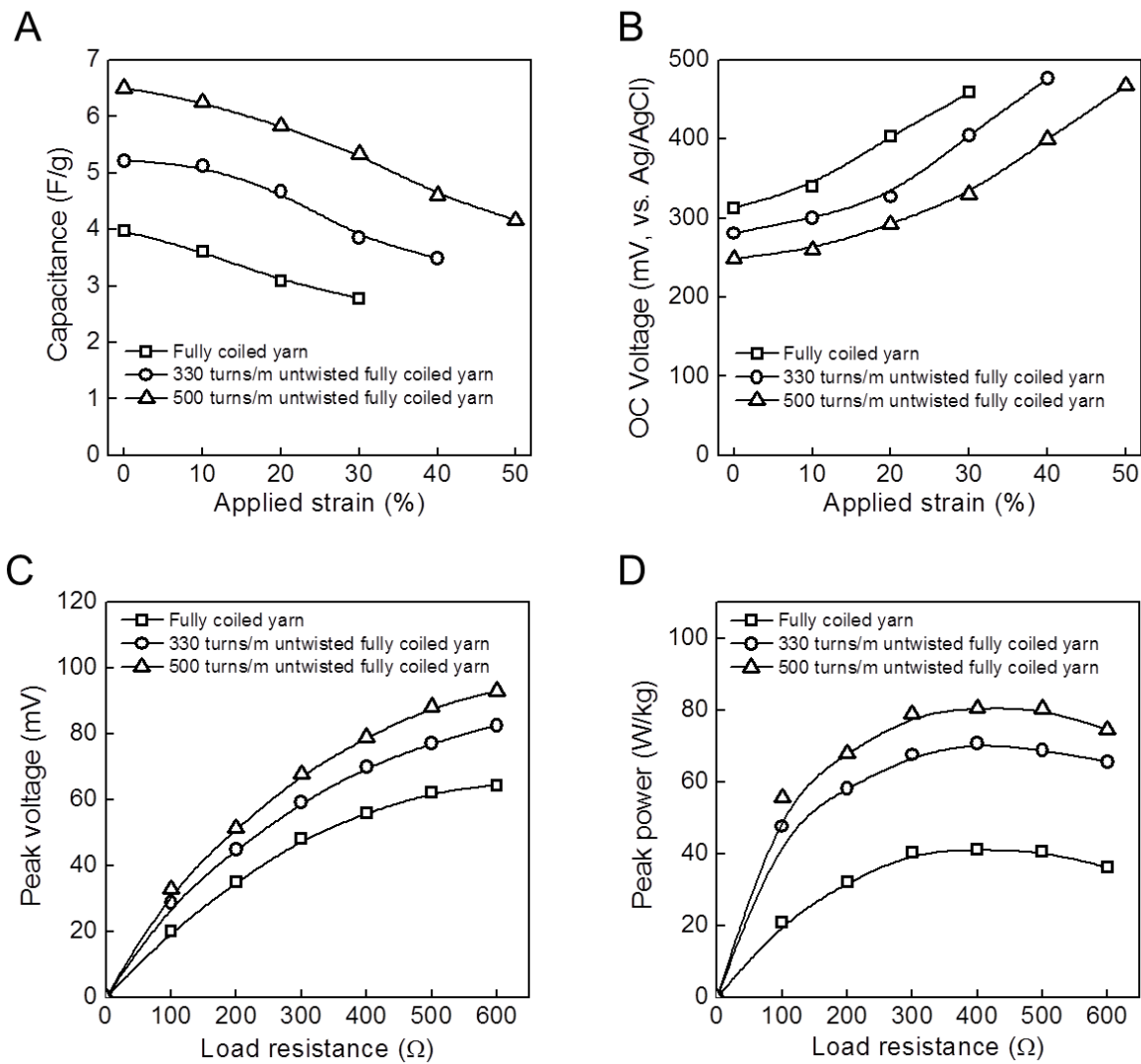


Fig. S6.

Comparison of the performance of fully coiled yarns that are fully twisted, untwisted by 300 turns/m, and untwisted by 500 turns/m. **(A)** Capacitance change versus applied strain, **(B)** OCV versus applied strain, **(C)** peak voltage versus load resistance and **(D)** peak power versus load resistance for fully twisted coiled yarn (open squares), 330 turns/m untwisted coiled yarn (open circles), and 500 turns/m untwisted coiled yarn (open triangles). The initial fully-twisted coiled yarn was 20 mm long, 67 μ m in yarn diameter, and had a spring index of 0.43. The frequency of the applied strain was 1 Hz, and the strain amplitude in (C) and (D) was the maximum reversible strain.

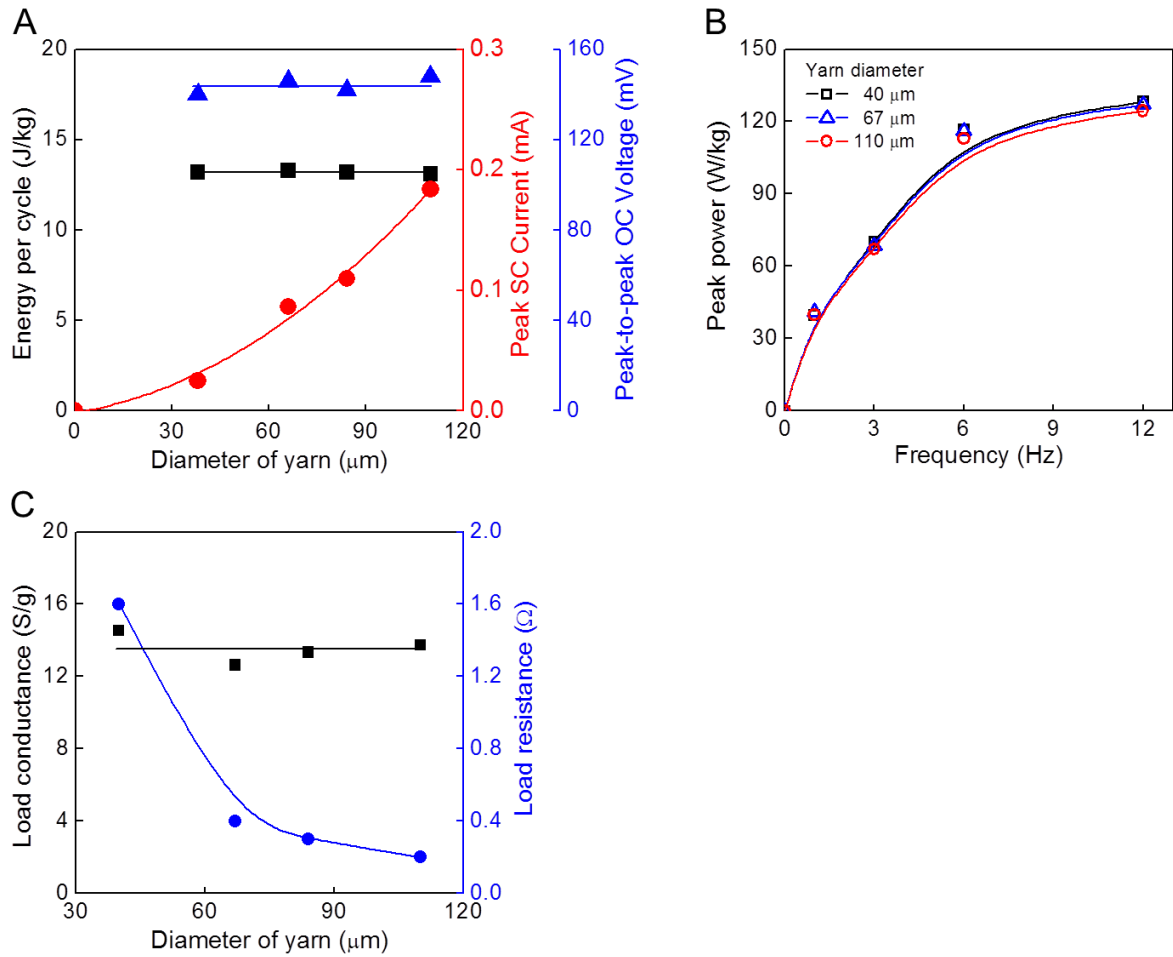


Fig. S7.

The effects of twistrion yarn diameter on harvesting the energy of 30% tensile strain, where yarns having different yarn diameters were coiled analogously, so that they have the same spring index (0.43). (A) Measurements for 1 Hz stretch showing that the generated per-cycle gravimetric energy (black squares) and the peak-to-peak open circuit voltage (blue triangles) were independent of yarn diameter. While the peak short-circuit current (red circles) quadratically increased with yarn diameter, the current per yarn cross-sectional area was independent of yarn diameter. (B) Measurements showing that the frequency dependence of peak gravimetric output power is independent of yarn diameter in the investigated range of yarn diameters (from 40 μm to 110 μm). (C) Measurements for 1 Hz stretch showing the diameter dependence of the load impedance that maximizes output power (blue circles) and the corresponding gravimetric load conductance (when normalized to the weight of the coiled twistrion yarn). For all of these measurements, the stretched electrode was a coiled 2-cm-long CNT yarn and the electrolyte was 0.1 M HCl.

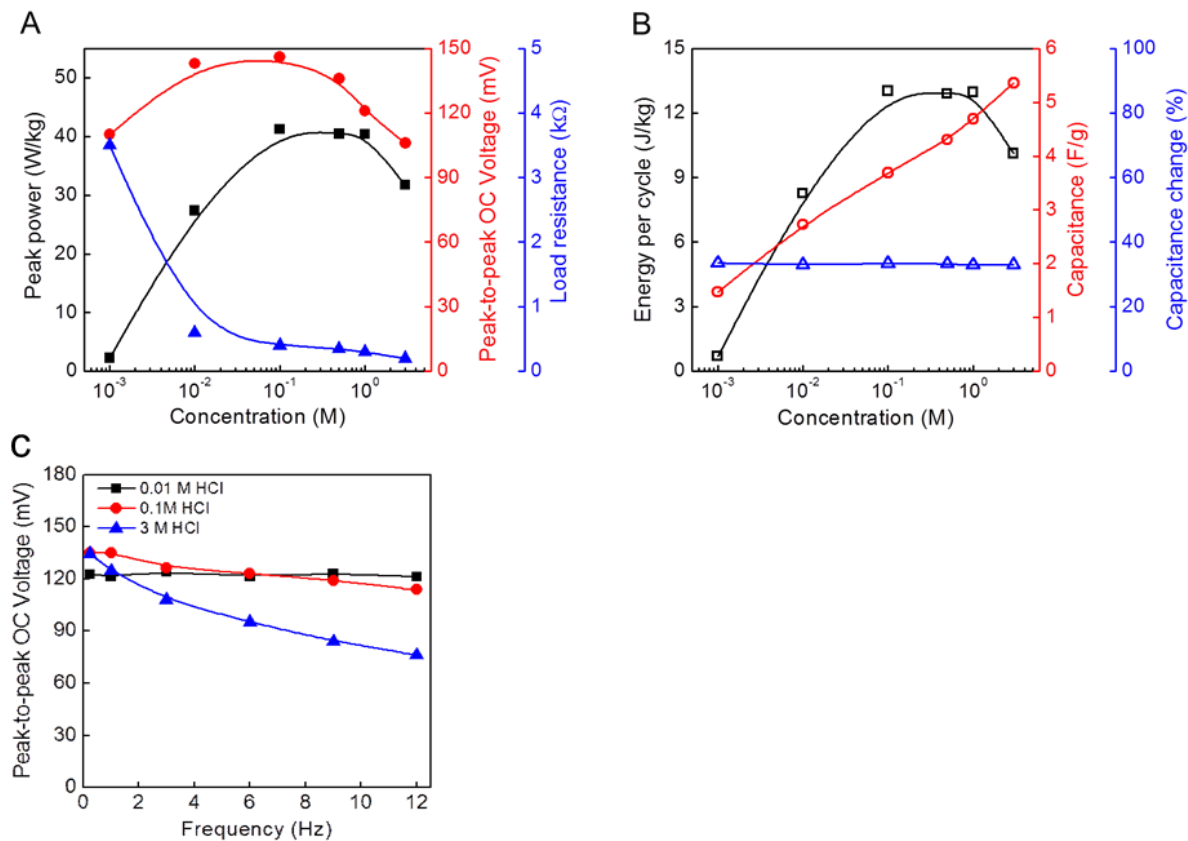


Fig. S8.

The effects of HCl solution concentration on the performance of a coiled tensile harvester during 1 Hz stretch to 30% strain. **(A)** Peak power (filled black squares), peak-to-peak OC voltage (filled red circles) and the impedance-matching load resistance (filled blue triangles) versus HCl concentration. **(B)** Energy per cycle (open black squares), capacitance at zero strain (open red circles) and percent capacitance change during 30% stretch (open blue triangles) versus HCl concentration. **(C)** The dependence of peak-to-peak OC voltage on cycle frequency for 0.01, 0.1, and 3 M HCl electrolyte. The diameter of the CNT yarn was 70 μm and the length of the coiled CNT yarn was 2 cm. The capacitance and capacitance changes are from CV scans at 50 mV/s.

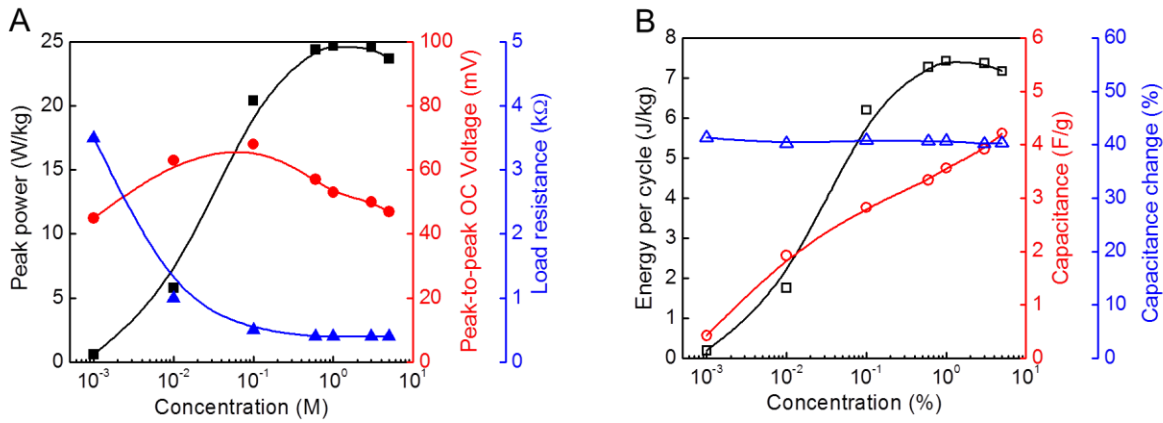


Fig. S9.

The effects of NaCl solution concentration on the performance of a coiled tensile harvester during 1 Hz stretch to 30% strain. **(A)** Peak power (filled black squares), peak-to-peak OC voltage (filled red circles), and the impedance-matching load resistance (filled blue triangles) versus NaCl concentration. **(B)** Energy-per-cycle (open black squares), capacitance (open red circles), and capacitance change (open blue triangles) during 30% stretch versus NaCl concentration. The diameter of the CNT yarn was 70 μm and the length of the coiled CNT yarn was 2 cm.\|

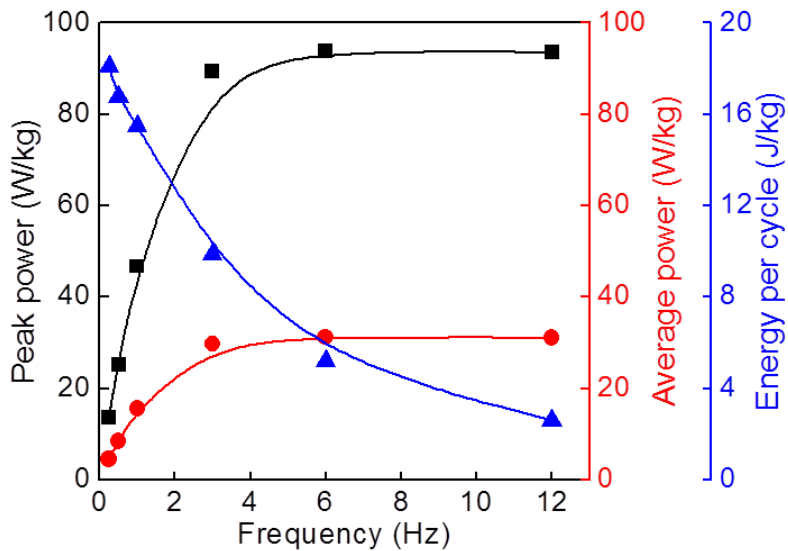


Fig. S10.

Peak power (squares), average power (circles) and electrical energy per cycle (triangles) as a function of sinusoidal deformation frequency to 30% tensile strain for energy harvesting in 0.6 M NaCl electrolyte. The harvesting electrode was a 64- μm -diameter coiled MWNT yarn that was 2 cm long and the counter electrode was Pt mesh/MWNT buckypaper.

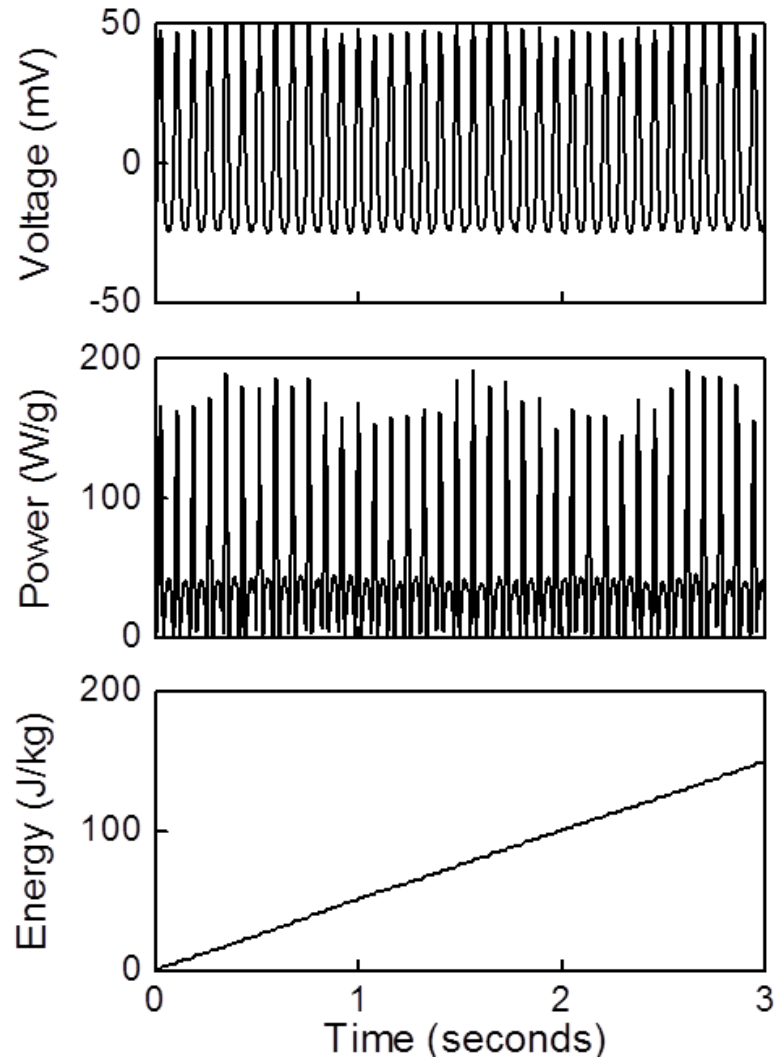


Fig. S11.

The time dependence of generated voltage, instantaneous power and total harvested energy from a coiled twistron harvester when stretched by 50% at 12 Hz in 0.1 M HCl. Using an impedance matched external resistance of 80 ohms and no externally applied bias voltage, the twistron harvester generated an average power of 49.7 W/kg. The diameter of the 20-mm-long, cone-spun, coiled yarn was 54 μm . The harvested electrical energy increased to 149.2 J/kg over the 3 seconds of energy harvesting.

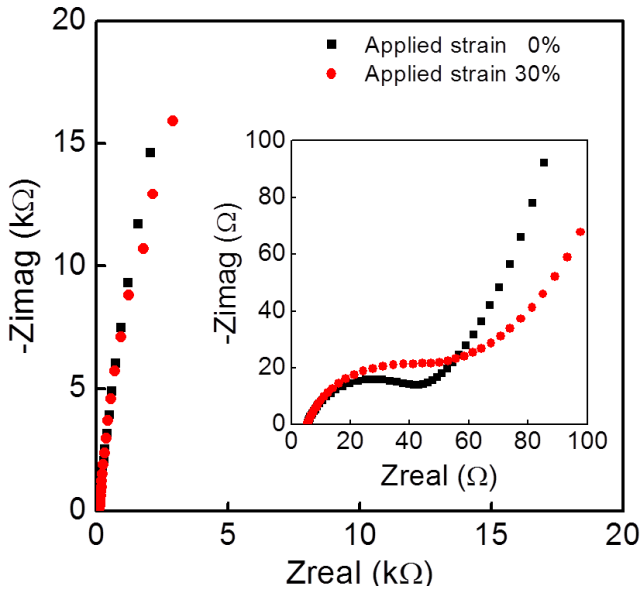


Fig. S12.

Potentiostatic electrochemical impedance spectroscopy (EIS) of a coiled CNT yarn. The coiled CNT yarn was made by cone spinning 4 layers of CNT sheets (4 cm wide and 30 cm long). About 5,900 turns/m of twist was inserted. A three electrode system consisting of the coiled CNT yarn working electrode, a Pt mesh/MWNT buckypaper counter electrode, and a Ag/AgCl reference electrode was immersed in a 0.1 M HCl solution and scanned from 0.01 Hz to 100,000 Hz.

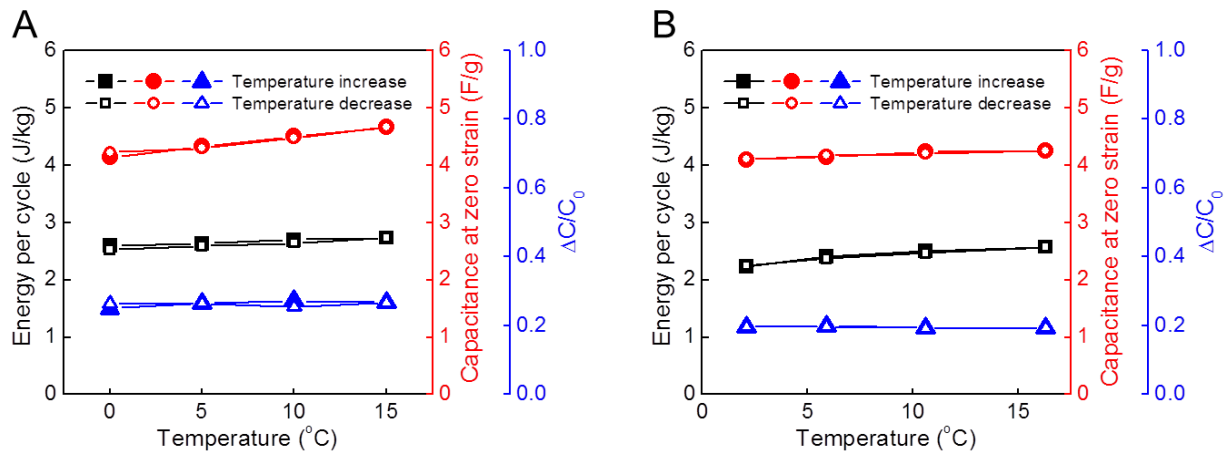


Fig. S13.

Per-cycle harvested energy (black squares), capacitance at zero strain (red circles), and fractional capacitance change (blue triangles) for tensile energy harvesting in (A) 0.6 M NaCl and in (B) 0.1 M HCl. A 1 Hz sinusoidal stretch to 10% tensile strain was applied. Increasing temperature data points (filled symbols) and decreasing temperature data points (open symbols) so closely overlap that the former is largely obscured.

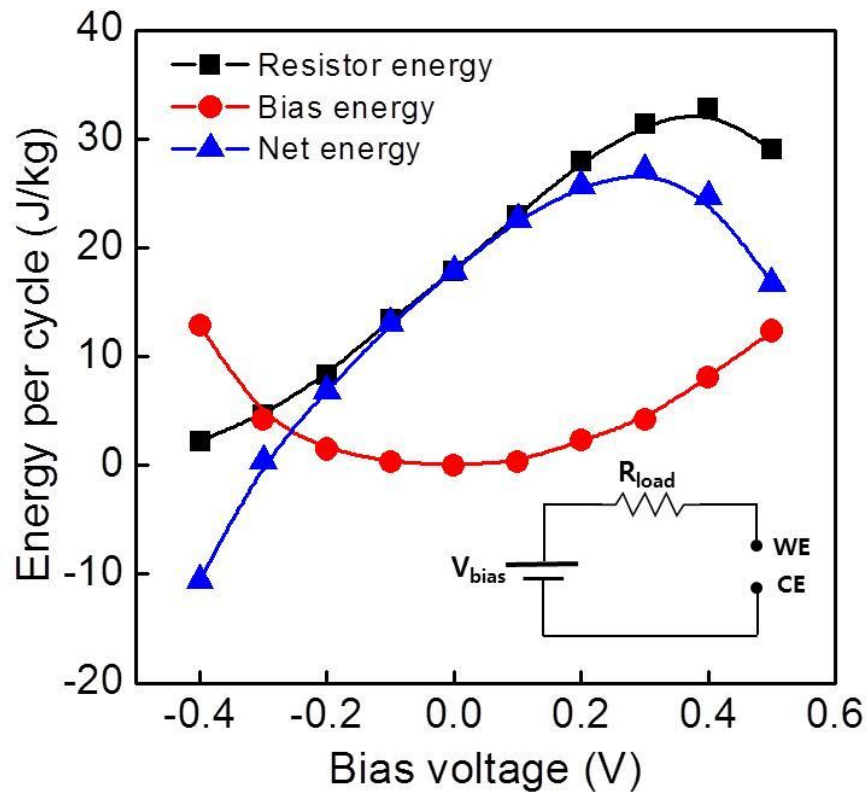


Fig. S14.

The effect of an externally applied bias potential on tensile energy harvesting by a coiled MWNT yarn. This figure shows the energy delivered to an external resistive load (black squares), the energy consumed in providing the external bias voltage (red squares), and the net energy harvested (blue triangles) as a function of the externally applied bias voltage. These results are for a coiled twistron harvester stretched by a 0.2 Hz square-wave deformation to 20% in 0.1 M HCl. A bias potential was applied between the working and counter electrodes, as illustrated in the inset, and an 800 ohm load resistor was used for impedance matched energy harvesting. These results show that the per-cycle net-output electrical energy increased from 17.9 J/kg with no externally applied bias to 27.1 J/kg when an additional 300 mV bias was applied.

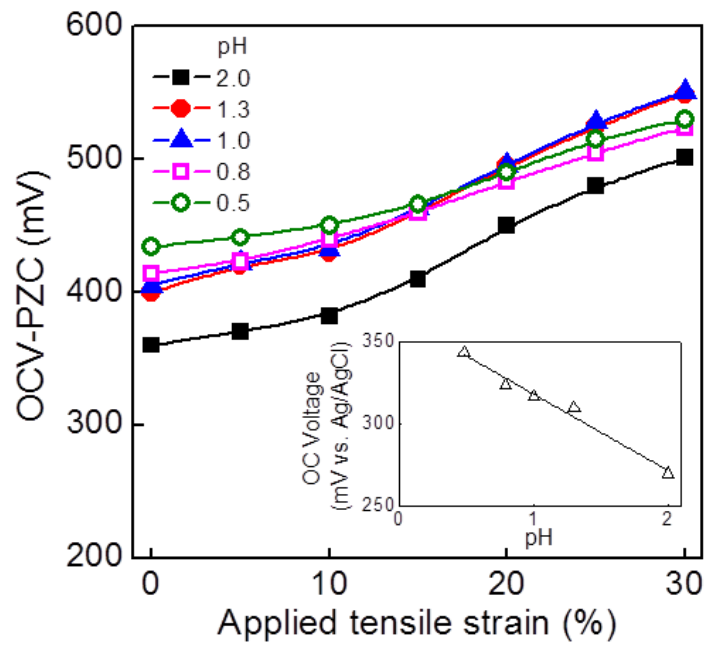


Fig. S15.

The effect of HCl electrolyte pH on the strain dependence of the difference between the OC voltage and the potential of zero charge (PZC). The inset shows that the OCV at zero strain decreases linearly with increasing pH of the electrolyte.

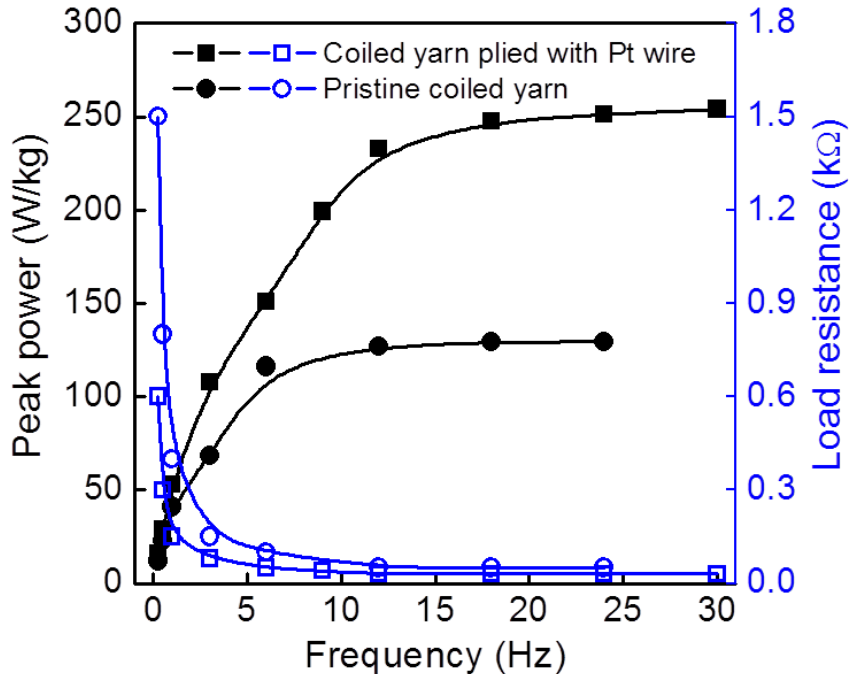


Fig. S16.

The effect of plying a 25- μm -diameter Pt wire with a coiled MWNT yarn on the frequency dependence of peak power and the load resistance that maximizes output power. Results for the Pt-wire-plied CNT harvester and the neat harvester are represented by square and circle symbols, respectively. Peak power and load resistances correspond to black and blue symbols, respectively. These results are for a tensile strain cycle to 30% strain in 0.1 M HCl electrolyte. The twistron electrode was a 2-cm-long coiled MWNT yarn and the counter electrode was a MWNT-buckypaper-wrapped Pt mesh. At 24 Hz, the Pt-plied twistron harvester had a 1.91 times higher peak power and a 0.6 times lower optimal load resistance compared with the pristine coiled yarn.

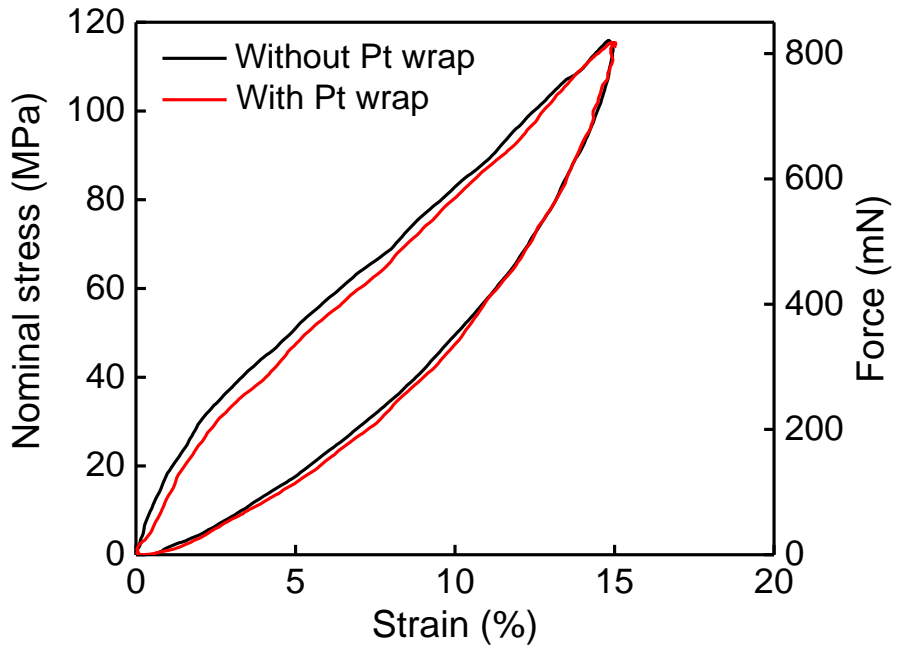


Fig. S17.

Stress-strain curve (left) and corresponding force measured for coiled twistron yarns during 0.2 Hz sinusoidal stretching in 0.1 M HCl electrolyte with (red) and without (black) Pt wire wrapping. These coiled twistron yarns were made by twisting a 95- μm -diameter, highly twisted but non-coiled carbon nanotube yarn, with and without 25-micron-diameter Pt wire under 41 MPa of load until fully coiled. The nominal stress was normalized to the diameter of the precursor highly twisted carbon nanotube yarn.

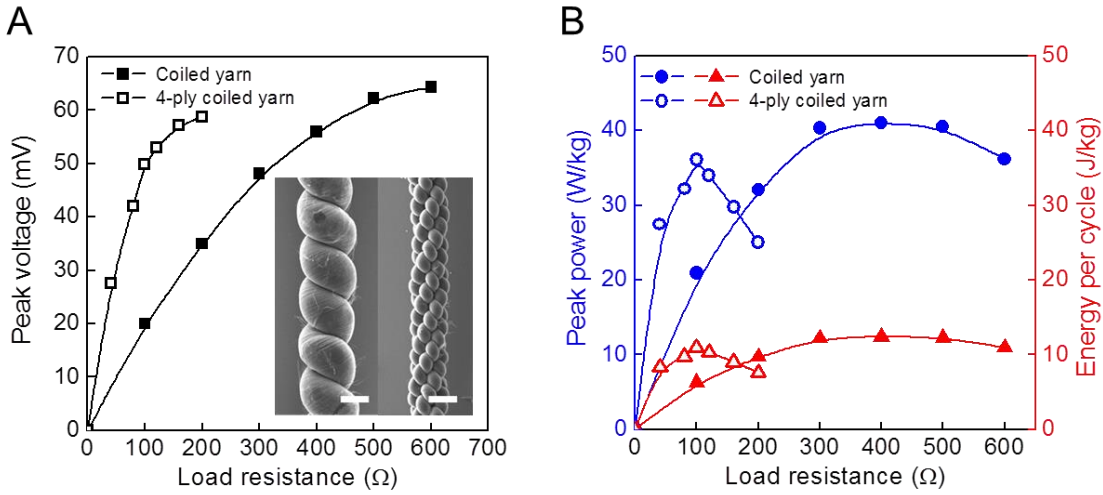


Fig. S18.

Comparison of (A) peak voltage (black symbols) and (B) peak power (blue symbols) and output energy per cycle (red symbols) versus load resistance for a coiled yarn (filled symbols) and a 4-ply coiled yarn tensile harvester (open symbols), when deformed at 1 Hz by 30% strain in 0.1 M HCl. The inset of (A) shows SEM images of the coiled CNT yarn (scale bar: 50 μm) and the 4-ply coiled CNT yarn (scale bar: 100 μm). All of the coiled CNT yarns have the same yarn diameter (70 μm), coiled CNT yarn length (2 cm) and coiled CNT yarn weight ($\sim 192 \mu\text{g}$).

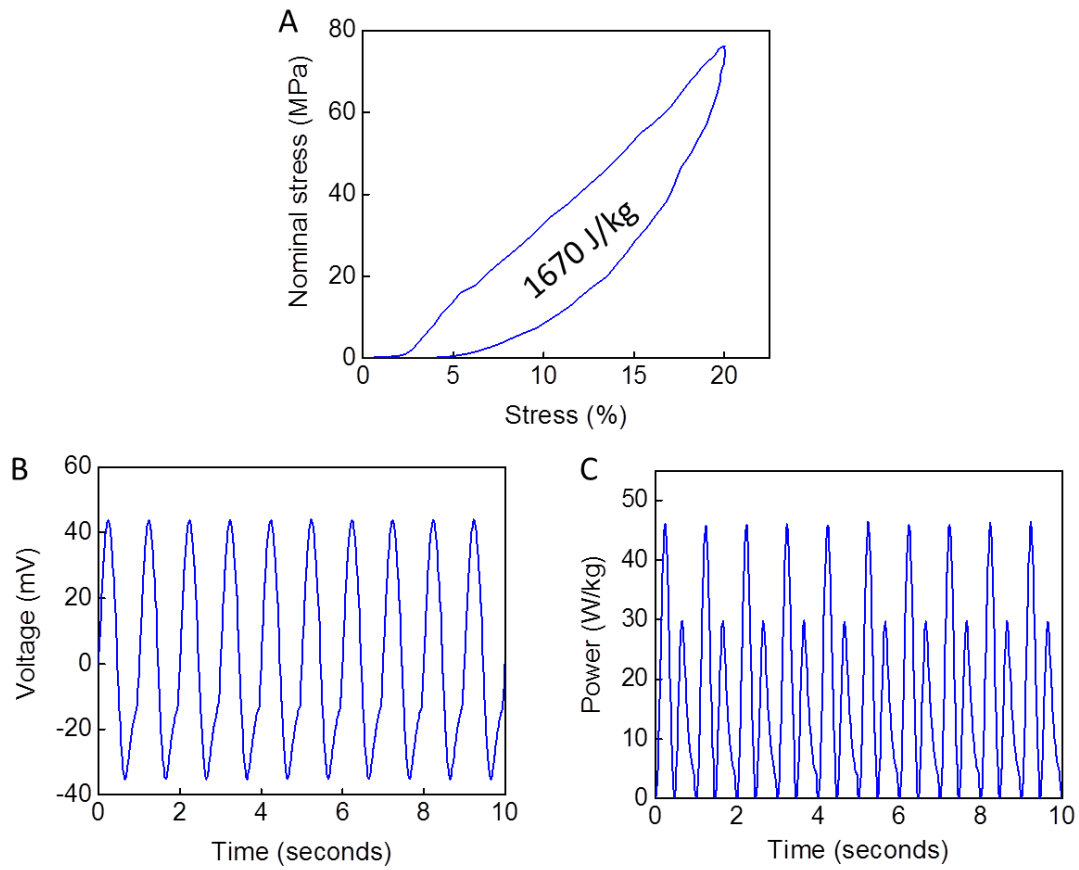


Fig. S19.

Efficiency of a coiled CNT yarn harvester that was untwisted by 8.5% of the twist required to fully coil. (A) The stress strain curve of the coiled yarn when sinusoidally stretched to 20% strain at 1 Hz in 0.1 M HCl. The mechanical energy lost between stretch and release during one cycle was 1670 Joules per kg of yarn. (B) The voltage generated on a 68 ohm load during the cyclical stretching in (A). (C) The instantaneous generated power during the cyclical stretching in (A). The electrical energy generated per cycle was 17.6 J/kg, corresponding to a conversion efficiency of 1.05%.

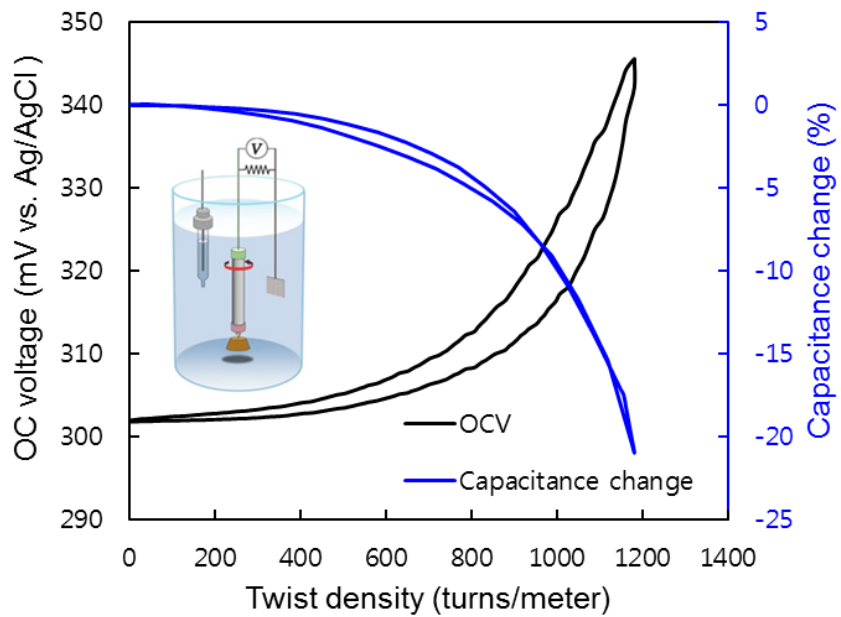


Fig. S20.

The dependence of open circuit voltage and capacitance change on twist and untwist for a non-coiled, 16-mm-long, 208- μm -diameter, cone-spun yarn, under an isobaric load (~20 MPa). The inset illustrates the experimental apparatus. These results are for comparison with the isometric load results of Fig. 2C. The twist insertion frequency (corresponding to the inverse time for complete twist insertion and removal) was 67 mHz for the OC voltage measurements and 4.2 mHz (corresponding to a potential scan rate of 100 mV/s) for the capacitance measurements. If this frequency for complete twist insertion and removal is reduced for the OC voltage measurements, the hysteresis in OC voltage largely disappears.

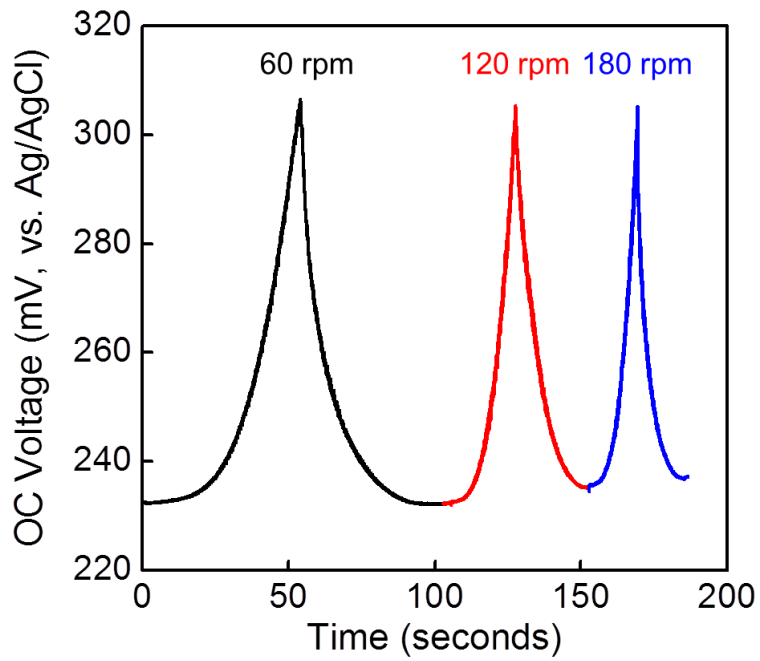


Fig. S21.

The open-circuit voltage of a non-coiled, 170- μm -diameter, 2.5-cm-long MWNT yarn during torsional energy harvesting by twisting and untwisting under an isobaric load (43 g) using different twisting speeds (revolutions per minute). The maximum inserted twist, which is below the twist needed for coiling this diameter yarn, was 2,000 turns/m and the twist minimum was 0 turns/m. The potential of the non-coiled yarn in the 0.1 M HCl electrolyte was measured using a three electrode system.

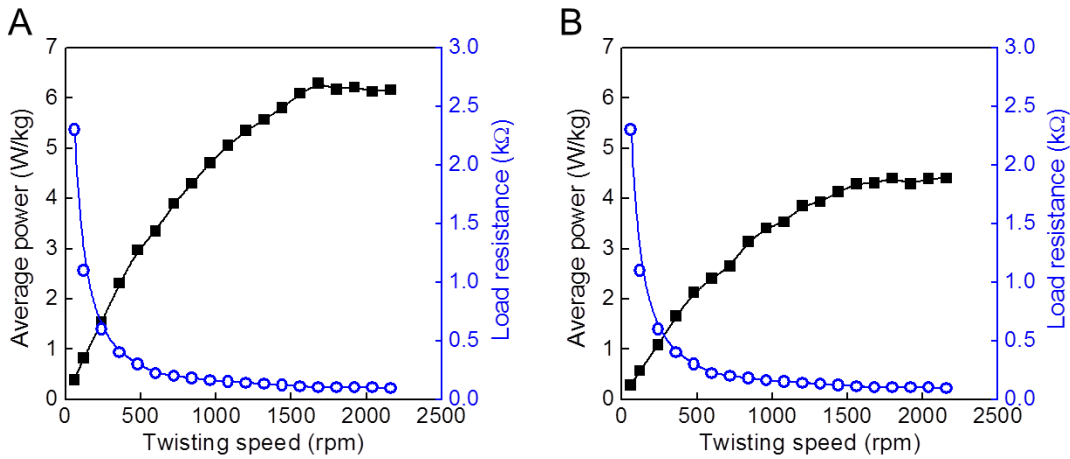


Fig. S22.

Torsional energy harvesting under isobaric load using a cone-spun, 140- μm -diameter, non-coiled CNT yarn immersed in 0.1 M HCl (**A**) and 0.6 M NaCl (**B**), respectively. As the twisting speed increased, the average power (filled black symbols) increased, while the impedance matching load resistance (open blue symbols) decreased.

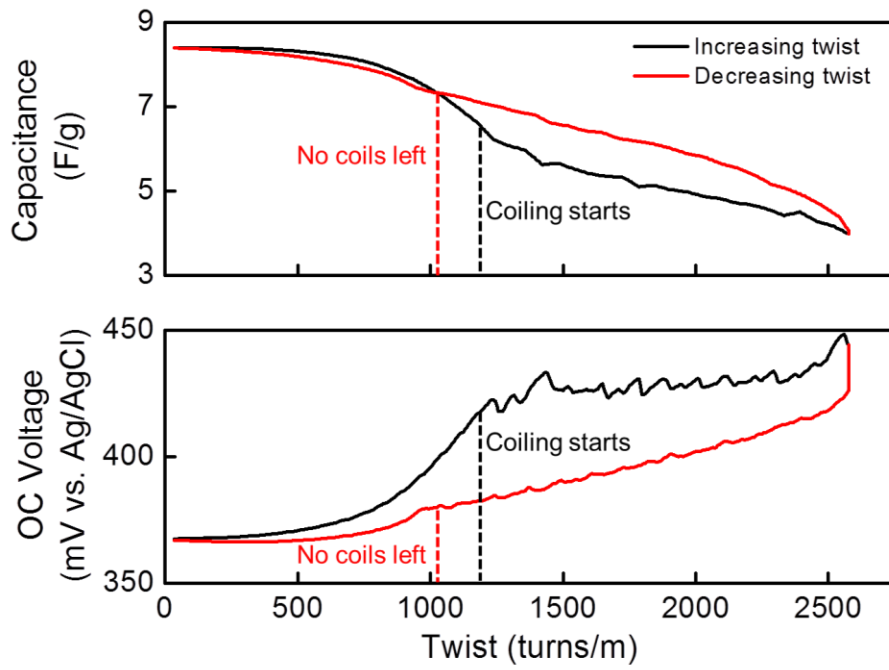


Fig. S23.

Capacitance and open-circuit voltage as a function of twist for a MWNT yarn when twisted and untwisted under a 20 MPa load between a non-twisted and a fully-coiled state. Vertical dashed lines indicate the points where coiling nucleates during up-twisting, and where all coils are removed during untwisting.

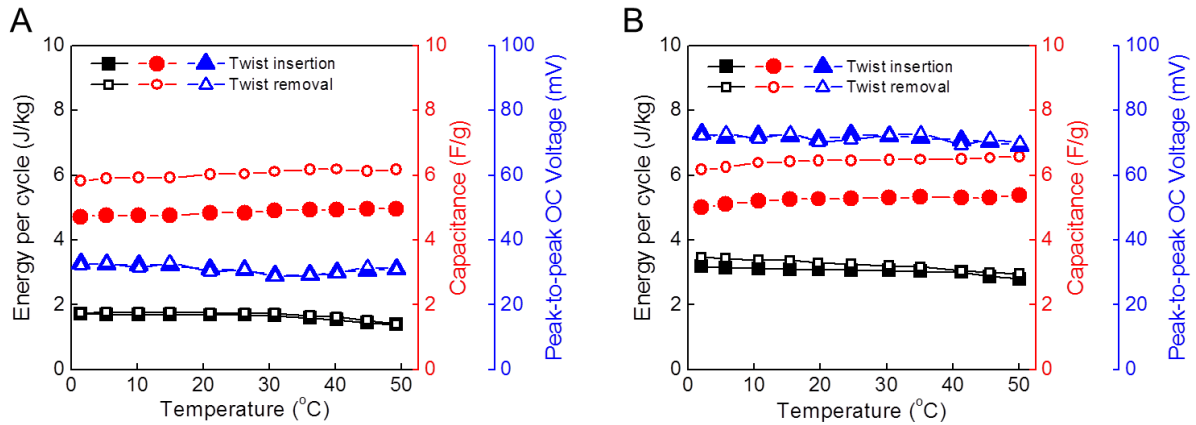


Fig. S24.

The effects of temperature on harvested energy per cycle (black squares) and peak-to-peak OC voltage (blue triangles) during the insertion (filled symbols) and removal (open symbols) of 1,500 turns/m of twist into a 28-mm-long, 140- μm -diameter, non-coiled, cone-spun twistron harvester in (A) 0.6 M NaCl electrolyte and in (B) 0.1 M HCl. Capacitances for the highly twisted state (filled red circles) and non-twisted state (open red circles) were obtained at a scan rate of 50 mV/s for a scan range of 0.3 V to 0.6 V. The frequency of a twist insertion and twist removal cycle was 0.024 Hz.

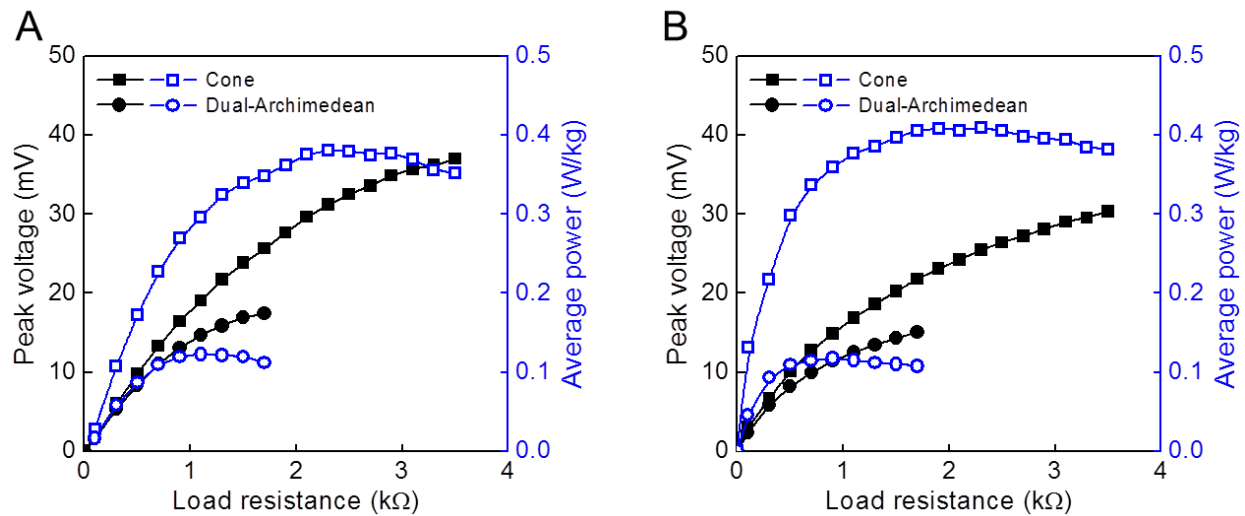


Fig. S25.

For energy harvesting by twist insertion and twist removal at 0.05 Hz, the effect of cone spinning (squares) and dual-Archimedean spinning (circles) on the dependence of peak voltage (black filled symbols) and average power (blue open symbols) on load resistance. The results in (A) are for twist insertion to just below the twist needed for coiling and those in (B) are for subsequent twist removal from the yarn to 357 turns/m twist. The initial length of the twistron harvester was 28 mm.

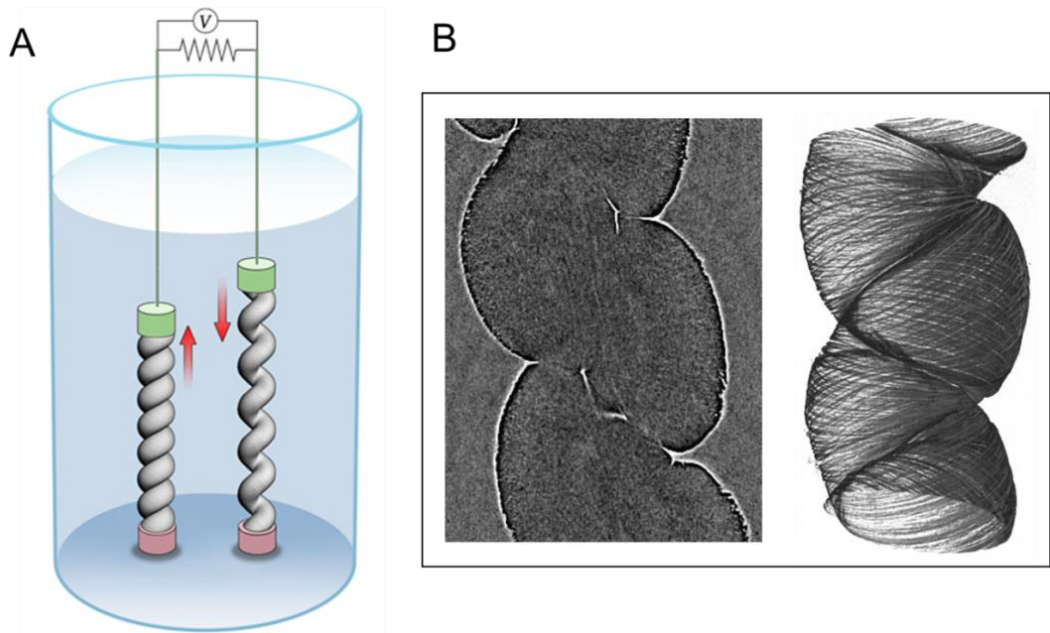


Fig. S26.

(A) Illustration of a two-electrode, dual-yarn energy harvester configuration to approximately double the output voltage and output current. This ‘seesaw’ configuration consists of two coiled CNT yarns which are stretched and released out-of-phase with respect to each other. (B) Phase-contrast x-ray tomography images of the coiled twistron yarn used for this harvester.

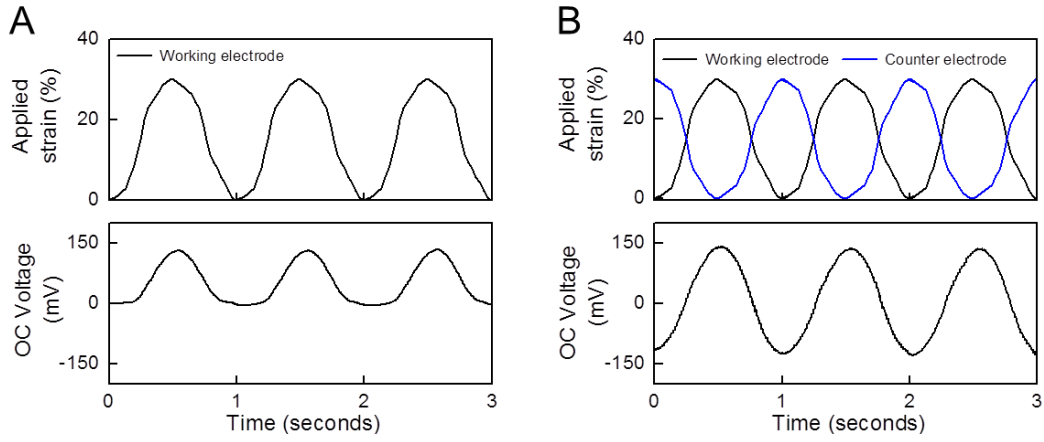


Fig. S27.

Open-circuit, inter-electrode voltage for one stretched electrode and for two stretched electrodes operated using the seesaw structure of Fig. S24. **(A)** The time dependence of applied strain and open-circuit, inter-electrode voltage when only one electrode is sinusoidally stretched at 1 Hz. **(B)** The time dependence of applied strain and open-circuit, inter-electrode voltage when both working and counter electrodes are sinusoidally stretched 180° out-of-phase at 1 Hz. The coiled MWNT yarn electrodes were 2 cm long and the yarn diameter was 70 μm . The seesaw structure, wherein the two electrodes are stretched 180° out-of-phase, generates a maximum open-circuit, inter-electrode voltage of about 257 mV which is about two times the voltage when only one electrode is mechanically stretched (132.4 mV).

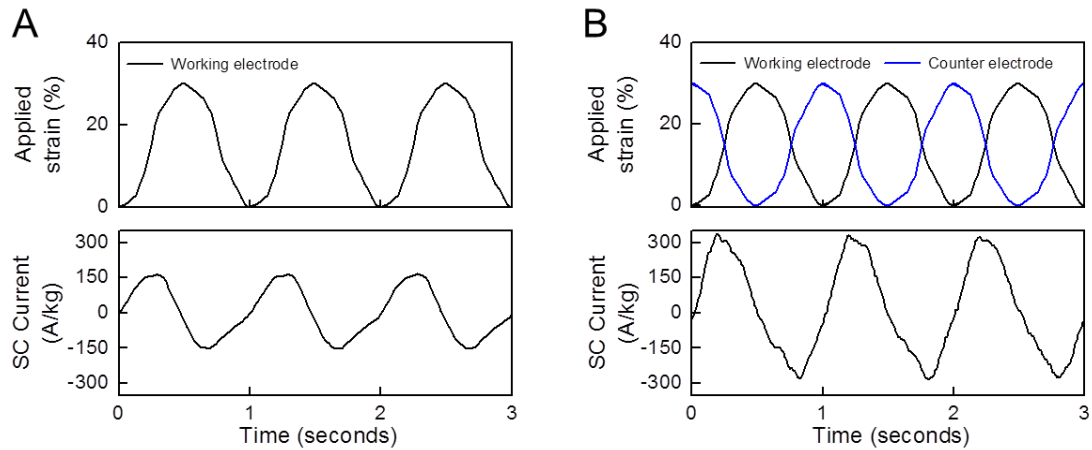


Fig. S28.

Short-circuit current for one stretched electrode and for two stretched electrodes operated using the seesaw structure of Fig. S24. These results are for the same harvester as in Fig. S27. **(A)** The time dependence of applied strain and short-circuit current when only one electrode is sinusoidally stretched at 1 Hz. **(B)** The time dependence of applied strain and short-circuit current when both working and counter electrodes are sinusoidally stretched 180° out-of-phase at 1 Hz. Based on the total weight of both electrodes, the seesaw structure, wherein the two electrodes are stretched 180° out-of-phase, generates a short-circuit current of about 327 A/kg, which is twice the current when only one electrode is stretched (162 A/kg). Based again on the total weight of the two electrodes, the average output power was 2.82 W/kg when one electrode was stretched, and 9.72 W/kg when both electrodes were stretched in the seesaw configuration. Also, the load resistance that optimized power output was unchanged in going from one harvesting electrode and an equivalent non-stretched counter electrode to two harvesting out-of-phase electrodes.

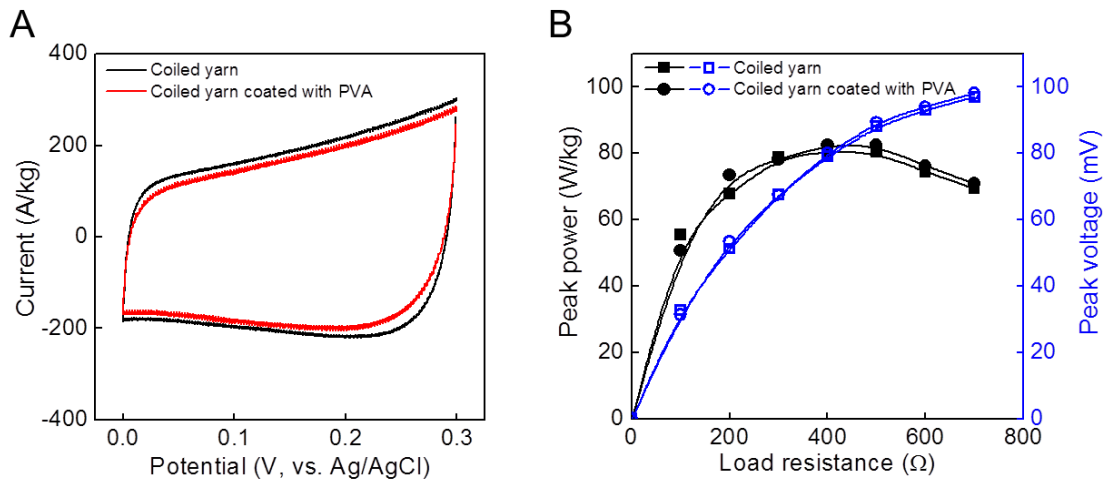


Fig. S29.

Comparison of the electrochemical performance of a coiled CNT yarn in a bath of 0.1 M HCl before and after coating the coiled yarn with polyvinyl alcohol (PVA). **(A)** CV curves (at a scan rate of 50 mV/s) before (black) and after (red) coating a coiled twistron harvester yarn with PVA. **(B)** Peak power (filled black symbols) and peak voltage (open blue symbols) versus load resistance for a coiled yarn before (circle symbols) and after (square symbols) coating with PVA (when a 1 Hz sinusoidal stretch of 50% was applied). As shown here, the cyclic voltammetry curves, the peak power, and peak voltage were little affected by the PVA.

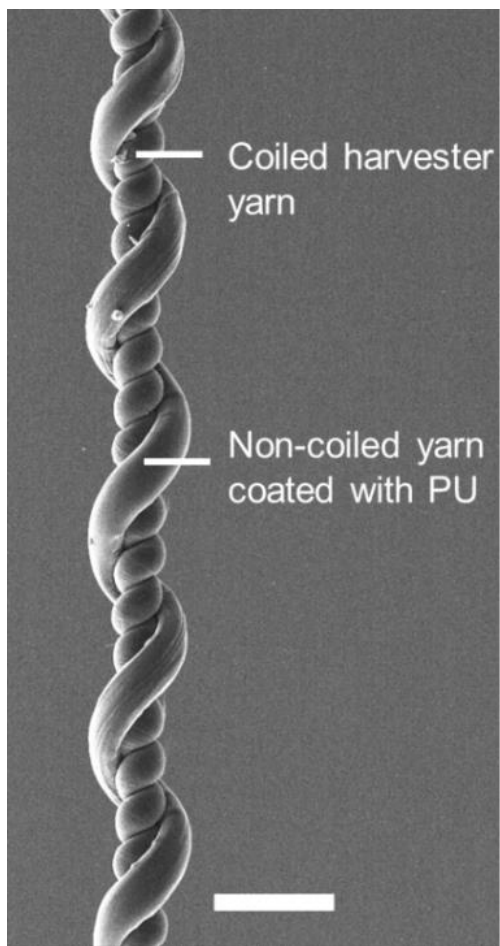


Fig. S30.

SEM image of a dual-electrode twistron harvester comprising a self-coiled MWNT yarn that generates electricity and a MWNT yarn counter electrode. The polyurethane coating on the non-coiled yarn prevented inter-electrode shorting. When swelled by 0.1 M HCl, which was incorporated into the yarn electrodes, this polyurethane became ionically conducting. The scale bar is 300 μm .

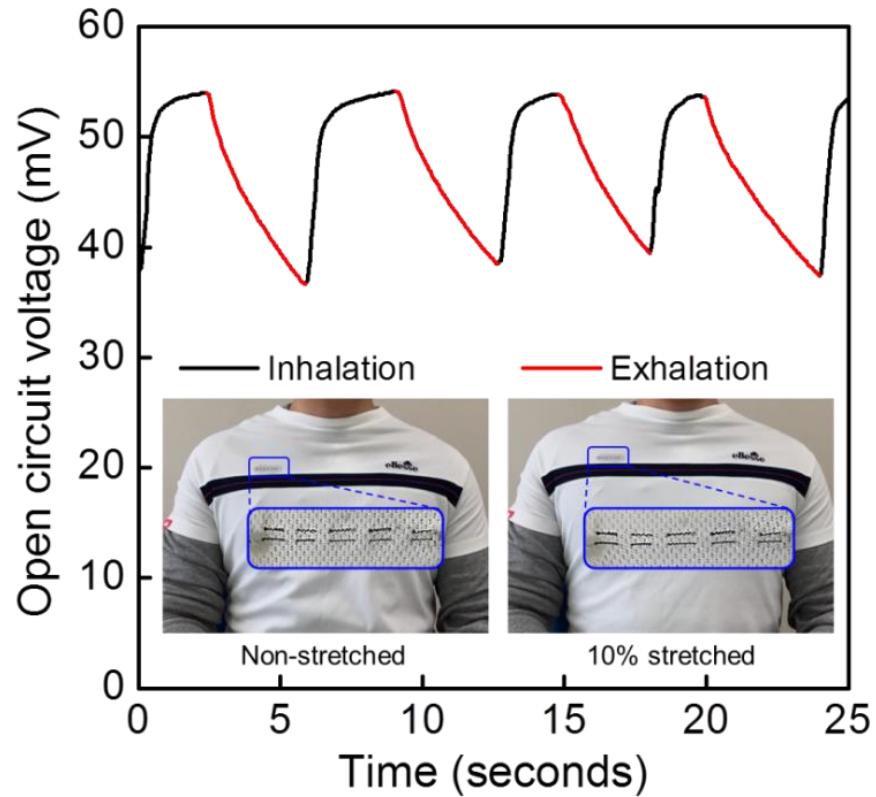


Fig. S31.

Self-powered twistrion strain sensor woven into a shirt and used for monitoring breathing. When periodically strained by about 10% during breathing, this four-cm-long twistrion sensor generated a periodic, peak-to-peak, open-circuit voltage of 16 mV. The inset shows (at two levels of magnification) the harvester woven into a shirt and used to monitor breathing. The yarn electrodes were 4 cm long and 250 μm in diameter. In the close-up image, the top twistrion harvester electrode is a homochiral coiled MWNT yarn and the bottom twistrion harvester electrode is a heterochiral coiled MWNT yarn.

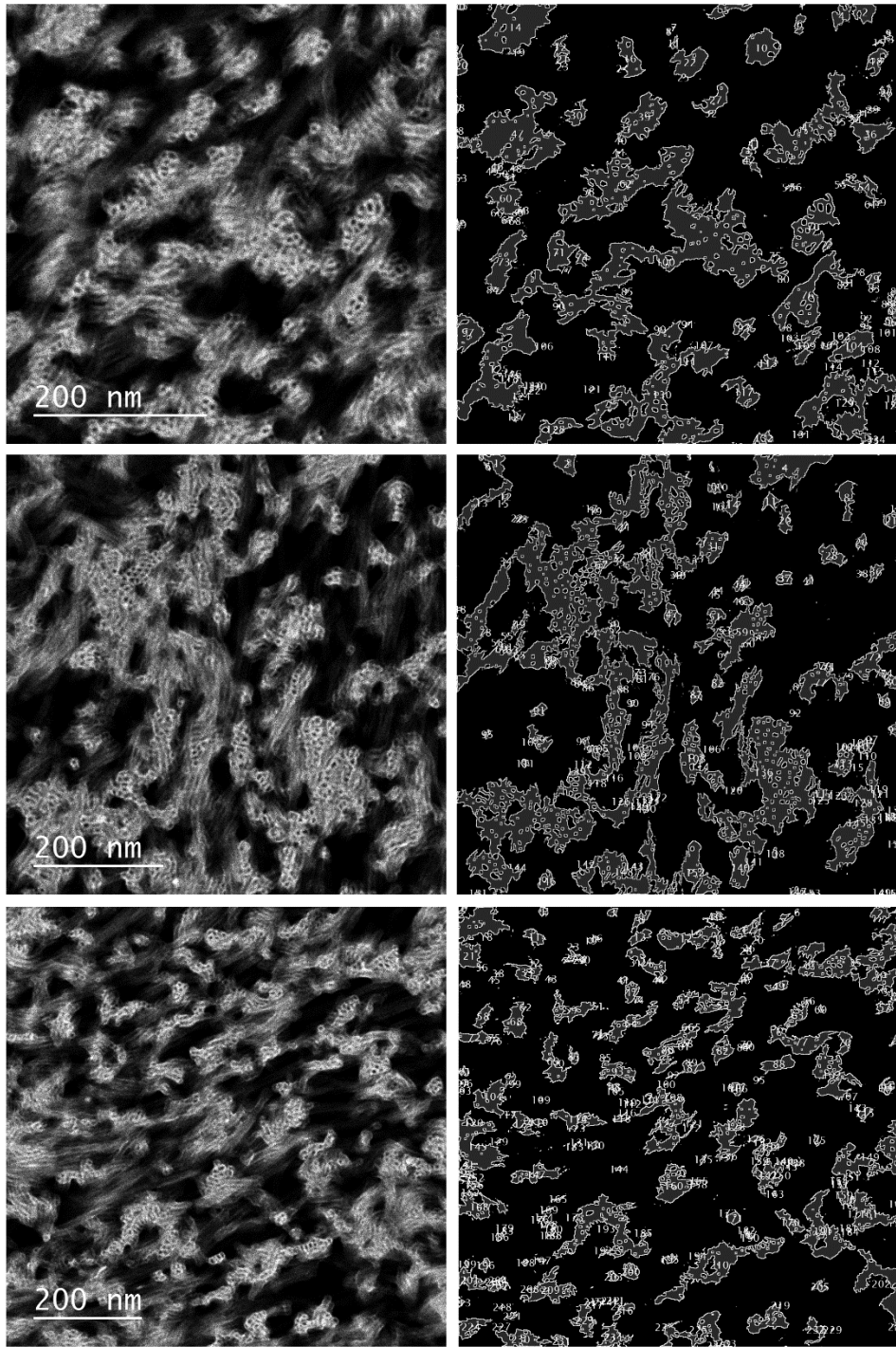


Fig. S32.

Analysis of surface-to-volume ratio for MWNT bundles within a twistron yarn. Using the particles analysis package included in Gatan's GMS software, the surface-to-volume ratio of bundles in a twistron yarn was evaluated from STEM-HAADF (High-Angle Annular Dark Field) images of the twistron yarn's cross section. Left: STEM-HAADF images of CNT bundles. Right: Mapped CNT bundle areas and perimeters. A total of 229 bundles were included in the analysis.

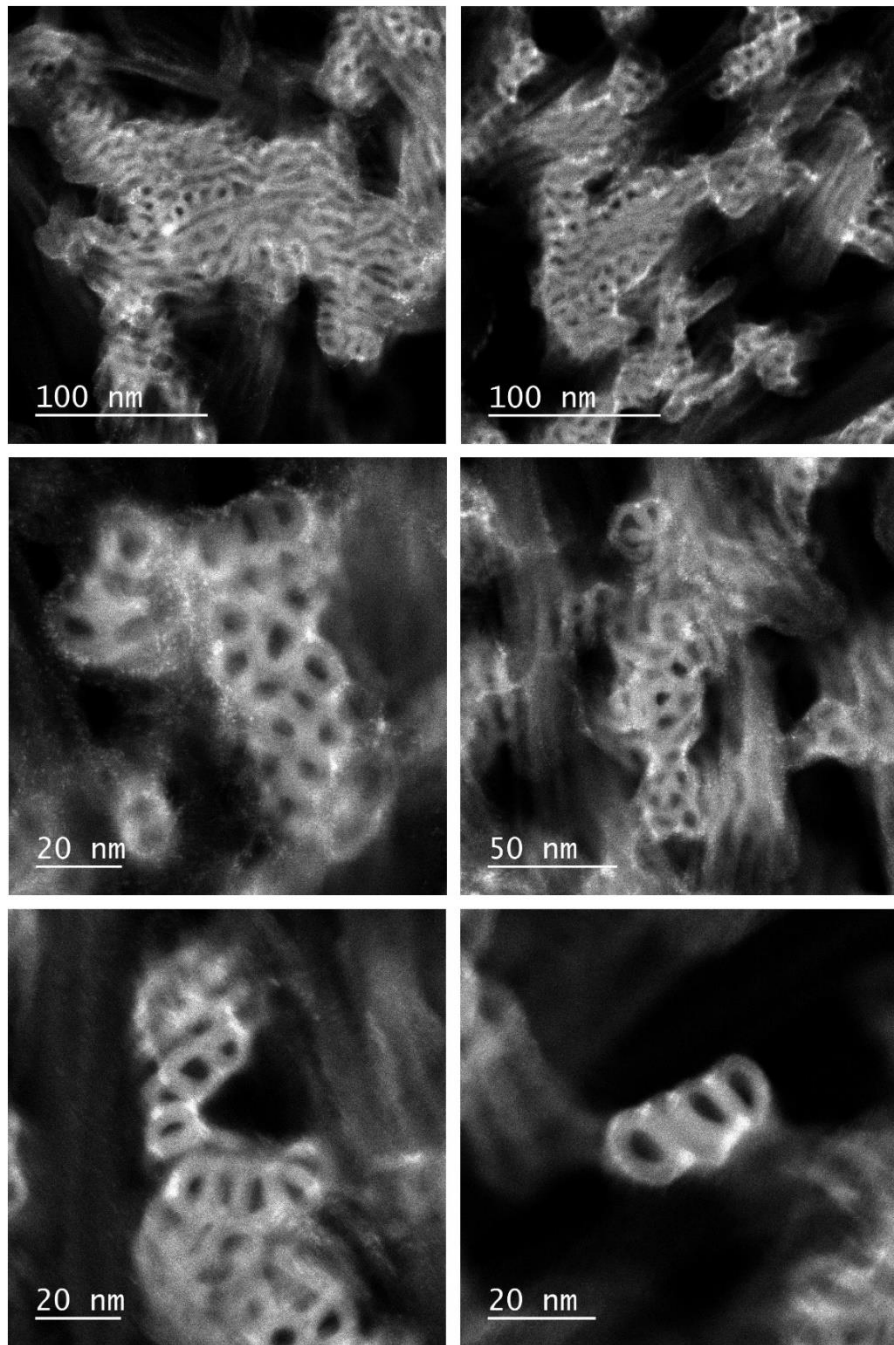


Fig. S33.

STEM High-Angle Annular Dark Field cross-section images of different size CNT bundles in a twistron harvester yarn after electrochemical cycling in 0.6 M NaCl. Since STEM-HAADF, also known as “Z-contrast imaging”, reveals the mass-density content, these images show the distribution of NaCl (bright spots) on the exterior and interior surfaces of CNT bundles. These images indicate that the Na^+ and Cl^- ions accumulate at the corners of nanotube junctions, and also follow tortuous paths within the intra-bundle space of larger bundles.

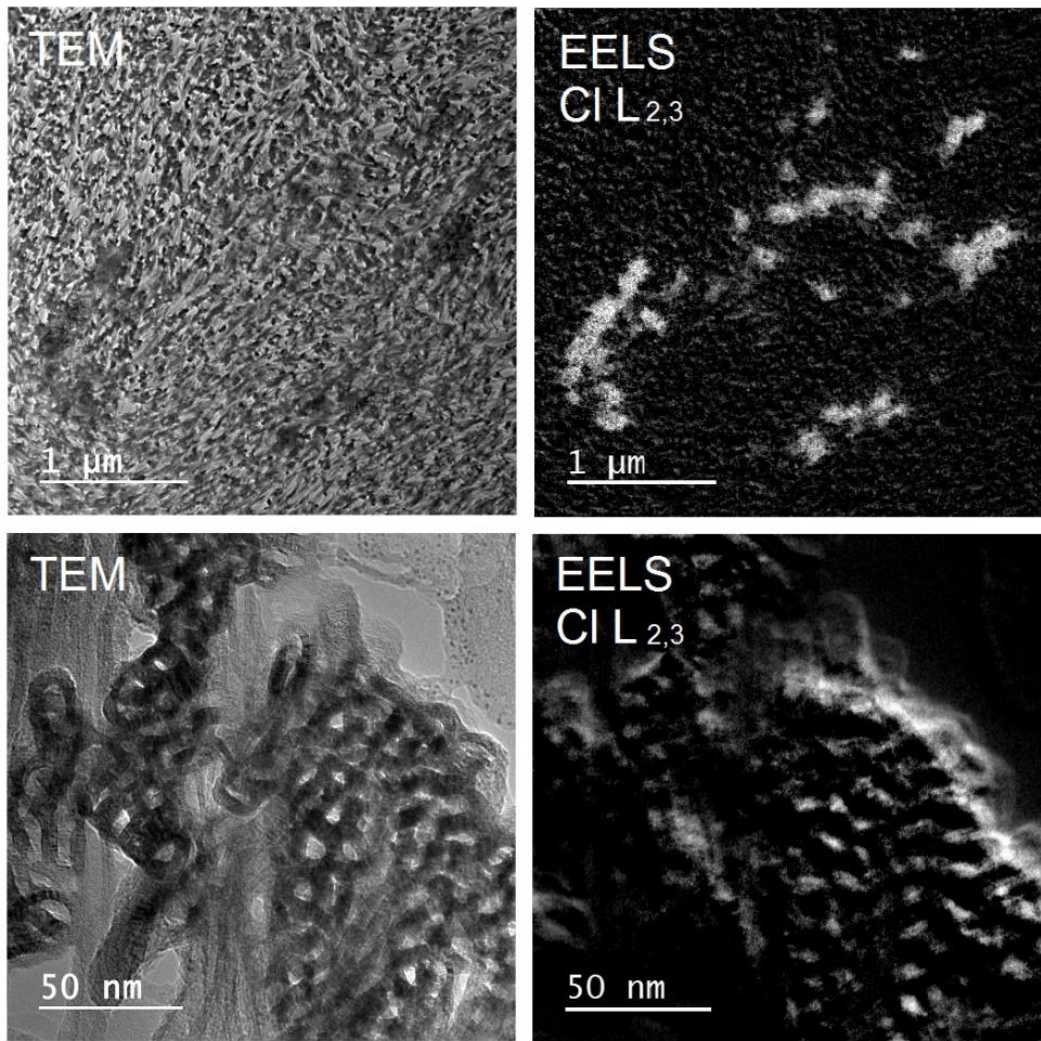


Fig. S34.

Electron energy loss spectroscopy images of a cross-section of a twistron yarn that had been electrochemically cycled in 0.6 M NaCl. Using a slit to select the Cl L_{2,3} edge (~200 eV) reveals the distribution of Cl within the cross-section of the twistron yarn. These images show the presence of Cl within a bundle, as well as in large salt deposits that are external to the bundle.

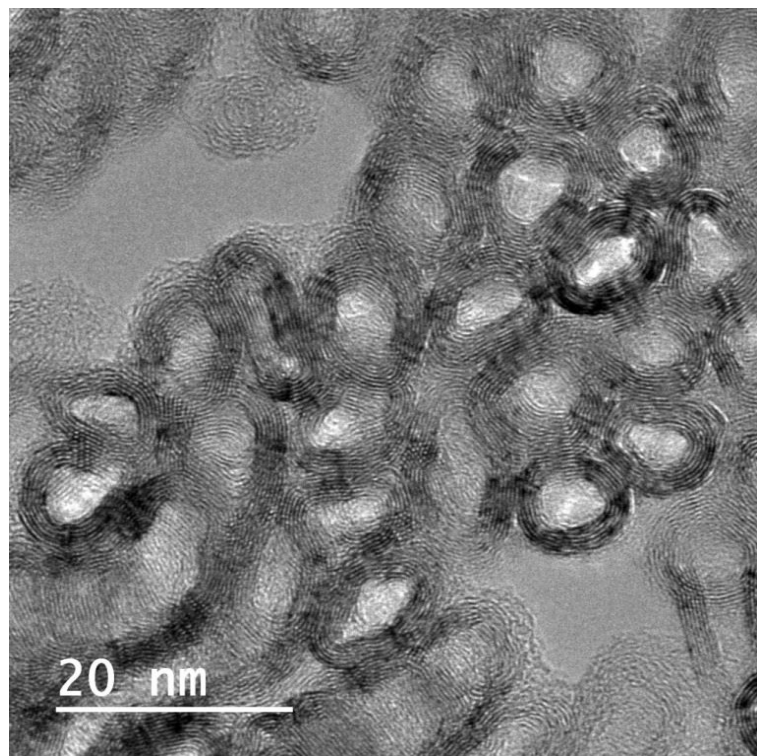


Fig. S35.

TEM image of a MWNT bundle, when viewed down the axis of a twistron yarn. This image was obtained by imaging a 100-nm-thick disk cut from the yarn using focused ion beam milling.

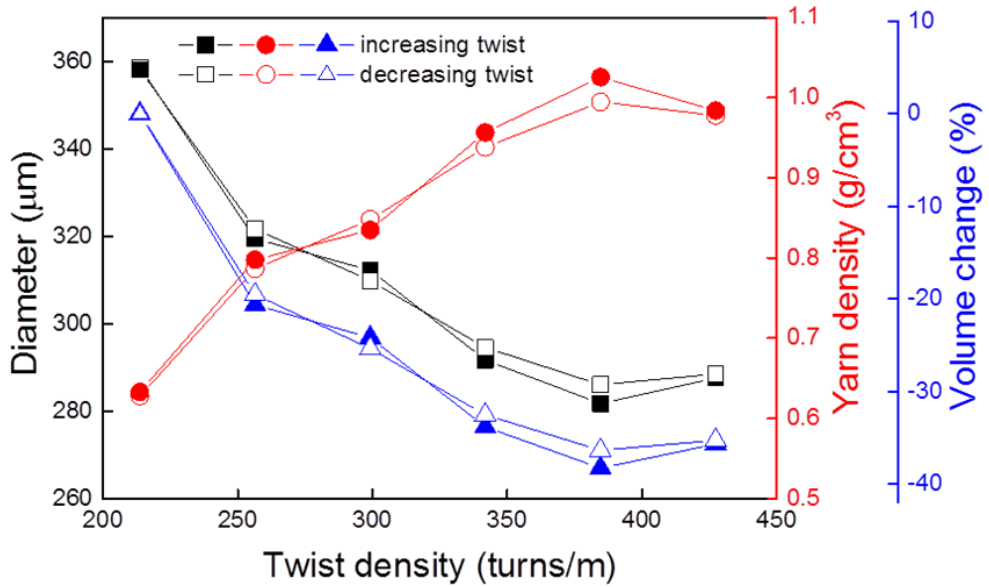


Fig. S36.

The twist dependence of the percent volume change (relative to yarn volume for 213 turns/m of twist) and yarn diameter for a cone-spun, non-coiled, twisted MWNT yarn during twisting and untwisting between 213 and 427 turns/m of twist, while the yarn was held at constant length in 0.1 M HCl.

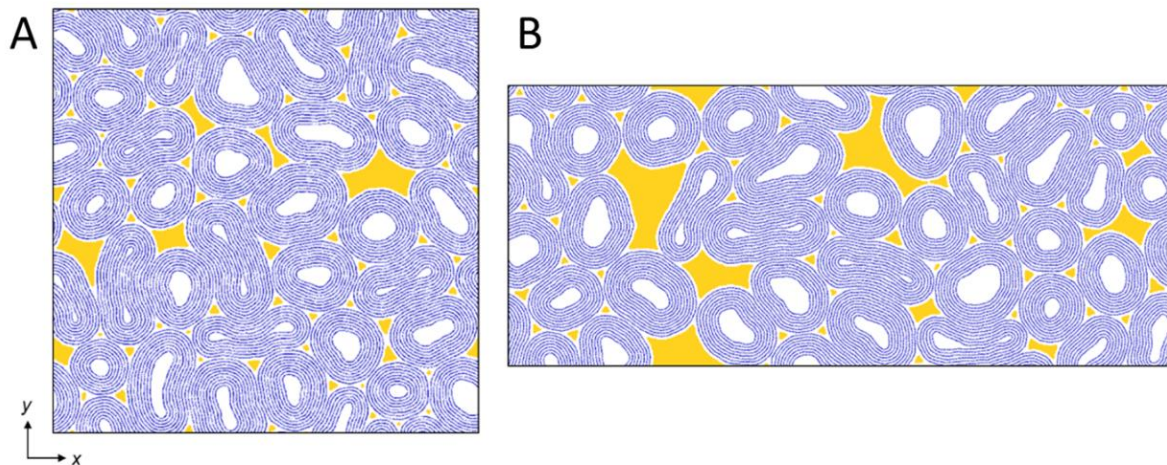


Fig. S37.

Molecular dynamics simulations to model the effect of twist-induced pressure on the electrochemically accessible void space within MWNT bundles. (A) Cross-sectional view of a simulated MWNT bundle when under a 50 MPa compressive stress along x- and y- directions. (B) Cross-sectional view of simulated MWNT bundle at zero pressure. Pores that are accessible by hydronium ions are shown in yellow.

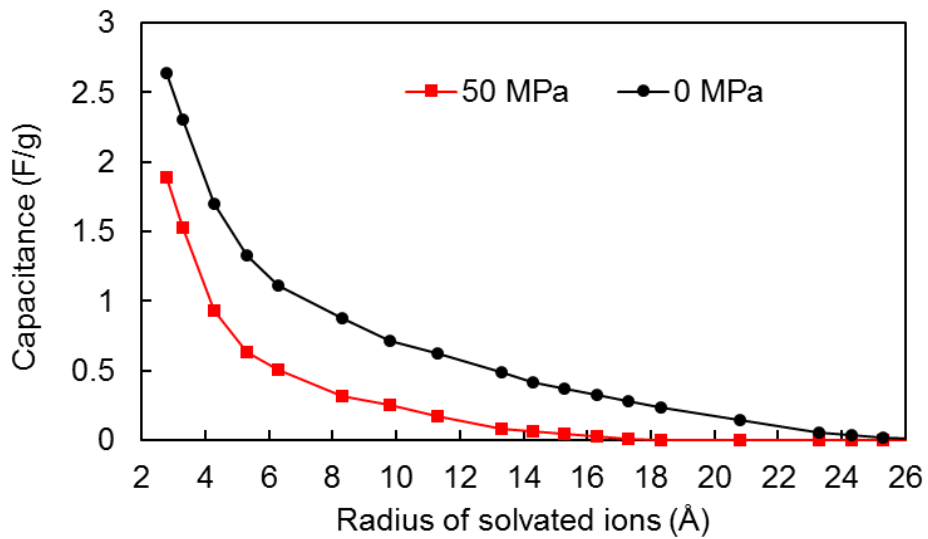


Fig. S38.

The calculated capacitance due to intra-bundle surface area as a function of the radius of the solvated ion. This capacitance decreases as the pressure induced by inserted twist increases from 0 to 50 MPa.

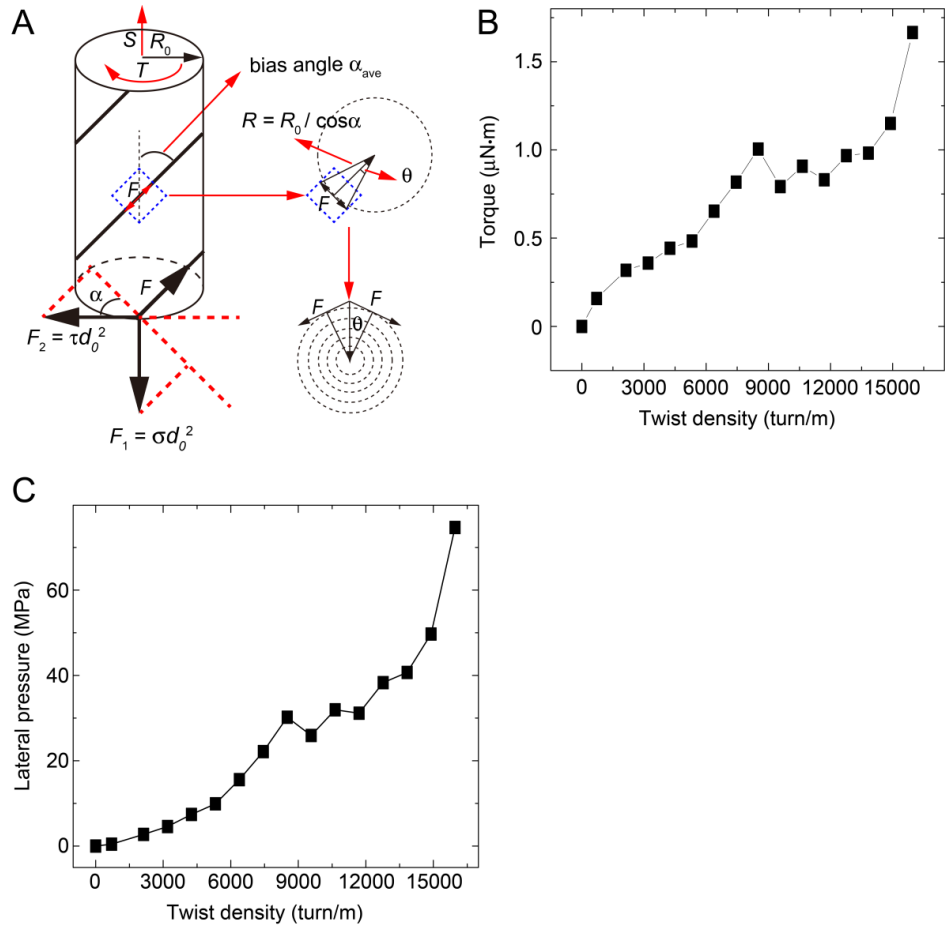


Fig. S39

(A) Illustration of the helix model used for calculating the average lateral pressure on MWNTs inside a twistron yarn. (B) The measured dependence of yarn torque on twist density for an applied tensile load of 30 MPa for a 36-μm-diameter forest-drawn MWNT yarn. (C) The calculated volume-averaged lateral pressure on MWNTs in a twistron yarn as a function of the twist density.

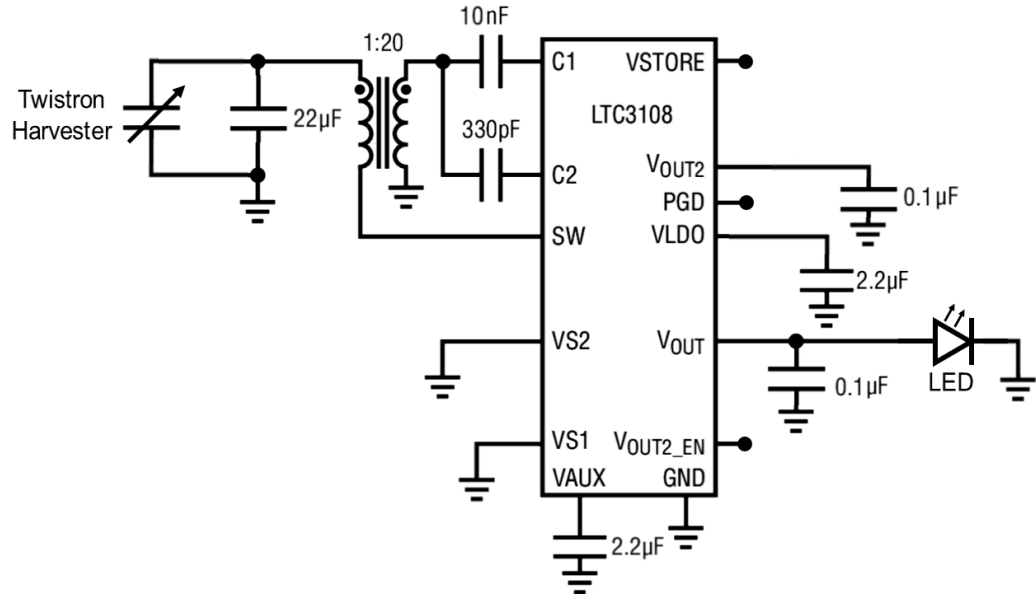


Fig. S40.

Schematic diagram of the boost converter circuit, based on a Linear Technologies LTC3108 integrated circuit, which increased the output voltage of the twistron harvester. This circuit was used for powering the green LED in Movie S2 when the harvester was stretched.

Table S1.

Comparison of structure and performance for yarns twist-spun using different methods. Measurements were conducted in 0.1 M HCl using a 1 Hz sinusoidal tensile strain of 30%

	Dual-Archimedean	Cone-spun	Funnel-spun	Fermat-spun	Tow-spun
Diameter (μm)	58	67	66	44	67
Spring index	0.43	0.43	0.43	0.44	0.44
Capacitance (F/g)	5.2	4.2	3.5	3.9	3.2
Capa. change (%)	19	30	38	37	40
OCV (mV)	80	140	130	146	104
Power (W/kg)	10.2	41.3	36.4	42.0	32.4
Density (g/cm^3)	1.21	1.29	1.30	1.32	1.36

Table S2.

Twistron performance compared with that for other solid-state mechanical energy harvesters. When power is reported without indication of whether it is peak power or average power, it is assumed to be peak power. If only average power is reported (72, 73, 76, 77), peak power was estimated by multiplying average power by a factor of 2 (and the estimated peak power and the thereby derived peak power/frequency are listed in parentheses). This calculation is equivalent to assuming a 50% duty cycle.

Ref.	Harvester Type	Harvester Weight	Frequency	Peak Power	Peak Power/Frequency
		(kg)	(Hz)	(W/kg)	(J kg ⁻¹ /cycle)
<i>Twistron</i>	CNT	$2.00 \cdot 10^{-7}$	30	250	8.33
<i>Twistron</i>	CNT	$2.00 \cdot 10^{-7}$	10	200	20
<i>Twistron</i>	CNT	$2.00 \cdot 10^{-7}$	6	150	25
<i>Twistron</i>	CNT	$2.00 \cdot 10^{-7}$	1.25	50	40
(50)	Piezoelectric	$1.95 \cdot 10^{-5}$	0.3	60.9	203
(51)	Piezoelectric	$1.27 \cdot 10^{-14}$	0.5	4.37	8.74
(52)	Piezoelectric	$2.71 \cdot 10^{-2}$	30	1.94	$6.46 \cdot 10^{-2}$
(53)	Piezoelectric	$4.00 \cdot 10^{-3}$	147	1.42	$9.63 \cdot 10^{-3}$
(54)	Piezoelectric	$1.04 \cdot 10^{-2}$	52	0.97	$1.86 \cdot 10^{-2}$
(55)	Piezoelectric	$5 \cdot 10^{-4}$	0.4	0.5	1.25
(56)	Piezoelectric	$4.00 \cdot 10^{-3}$	600	0.23	$3.75 \cdot 10^{-4}$
(57)	Piezoelectric	$7.71 \cdot 10^{-2}$	9	0.23	$2.50 \cdot 10^{-2}$
(58)	Piezoelectric	$9.52 \cdot 10^{-3}$	30	$9.50 \cdot 10^{-2}$	$3.15 \cdot 10^{-3}$
(59)	Piezoelectric	$3.39 \cdot 10^{-3}$	68.1	$3.40 \cdot 10^{-2}$	$5.00 \cdot 10^{-4}$
(60)	Piezoelectric	$9.56 \cdot 10^{-4}$	0.3	$1.50 \cdot 10^{-2}$	$5.00 \cdot 10^{-2}$
(61)	Piezoelectric	$1.98 \cdot 10^{-16}$	0.7	$1.25 \cdot 10^{-2}$	$1.78 \cdot 10^{-2}$
(62)	Electrostatic	$5.00 \cdot 10^{-3}$	50	$1.41 \cdot 10^{-2}$	$2.82 \cdot 10^{-4}$
(63)	Electrostatic	$1.04 \cdot 10^{-1}$	50	$1.01 \cdot 10^{-2}$	$2.02 \cdot 10^{-4}$
(64, 65)	Electrostatic	$5.80 \cdot 10^{-3}$	2	$6.90 \cdot 10^{-3}$	$3.45 \cdot 10^{-3}$
(66)	Electrostatic	$6.00 \cdot 10^{-5}$	180	$5.42 \cdot 10^{-4}$	$3.03 \cdot 10^{-6}$
(67)	Triboelectric	$8.8 \cdot 10^{-4}$	1	265	265
(68)	Triboelectric-Piezoelectric Hybrid	$1.58 \cdot 10^{-3}$	5	59	11.8

(69)	Triboelectric	$2.60 \cdot 10^{-4}$	0.33	7.44	22.6
(70)	Triboelectric	$7.00 \cdot 10^{-3}$	10	0.6	0.06
(71)	Triboelectric	$6.51 \cdot 10^{-4}$	3	0.35	0.12
(36)	Triboelectric		0.1-3	$(5.72 \cdot 10^{-3}$ to 0.113)	$(3.71 \cdot 10^{-2}$ to $7.9 \cdot 10^{-2}$)
(72)	Triboelectric	$5.33 \cdot 10^{-2}$	10	$2.63 \cdot 10^{-3}$	$2.63 \cdot 10^{-4}$
(73)	Dielectric Elastomer	$6.00 \cdot 10^{-4}$	0.5	(560)	(1120)
(74)	Dielectric Elastomer		0.22	(340)	(1545)
(15, 75)	Dielectric Elastomer	$4.00 \cdot 10^{-2}$	0.3	40.5	135
(76)	Dielectric Elastomer	$3.50 \cdot 10^{-4}$	3	37.8	12.6
(77)	Dielectric Elastomer	$4.83 \cdot 10^{-5}$	1	(12)	(12)
(78)	Dielectric Elastomer	$3.20 \cdot 10^{-4}$	1.6	(11.3)	(7.06)
(79)	Dielectric Elastomer		2		0.39

Movie S1.

Application of a twistron harvester for monitoring breathing. A pair of homochiral and heterochiral carbon nanotube harvester yarns were sewn into a shirt, and overcoated with gel electrolyte of 10 wt% PVA in 0.1M HCl. During breathing, the sensor stretched by 10%, producing 16 mV of voltage.

Movie S2.

Stretching a coiled CNT yarn (weighing 19.2 mg) to 13% strain at 0.5 Hz, using a 20% duty square wave, powers a voltage boost converter (fig. S40), which enables the harvester yarn to drive a green light-emitting diode.

References and Notes

1. S. Beeby, T. O'Donnell, "Electromagnetic energy harvesting" in *Energy Harvesting Technologies*, S. Priya, D. Inman, Eds. (Springer, 2009).
2. L. Persano, C. Dagdeviren, Y. Su, Y. Zhang, S. Girardo, D. Pisignano, Y. Huang, J. A. Rogers, High performance piezoelectric devices based on aligned arrays of nanofibers of poly(vinylidenefluoride-co-trifluoroethylene). *Nat. Commun.* **4**, 1633 (2013).
[doi:10.1038/ncomms2639](https://doi.org/10.1038/ncomms2639) [Medline](#)
3. Z. L. Wang, J. Song, Piezoelectric nanogenerators based on zinc oxide nanowire arrays. *Science* **312**, 242–246 (2006). [doi:10.1126/science.1124005](https://doi.org/10.1126/science.1124005) [Medline](#)
4. S. Niu, X. Wang, F. Yi, Y. S. Zhou, Z. L. Wang, A universal self-charging system driven by random biomechanical energy for sustainable operation of mobile electronics. *Nat. Commun.* **6**, 8975 (2015). [doi:10.1038/ncomms9975](https://doi.org/10.1038/ncomms9975) [Medline](#)
5. W. Tang, J. Tian, Q. Zheng, L. Yan, J. Wang, Z. Li, Z. L. Wang, Implantable self-powered low-level laser cure system for mouse embryonic osteoblasts' proliferation and differentiation. *ACS Nano* **9**, 7867–7873 (2015). [doi:10.1021/acsnano.5b03567](https://doi.org/10.1021/acsnano.5b03567) [Medline](#)
6. J. Yin, X. Li, J. Yu, Z. Zhang, J. Zhou, W. Guo, Generating electricity by moving a droplet of ionic liquid along graphene. *Nat. Nanotechnol.* **9**, 378–383 (2014).
[doi:10.1038/nnano.2014.56](https://doi.org/10.1038/nnano.2014.56) [Medline](#)
7. S. Ghosh, A. K. Sood, N. Kumar, Carbon nanotube flow sensors. *Science* **299**, 1042–1044 (2003). [doi:10.1126/science.1079080](https://doi.org/10.1126/science.1079080) [Medline](#)
8. J. W. Liu, L. M. Dai, J. W. Baur, Multiwalled carbon nanotubes for flow-induced voltage generation. *J. Appl. Phys.* **101**, 064312 (2007). [doi:10.1063/1.2710776](https://doi.org/10.1063/1.2710776)
9. T. Park, C. Park, B. Kim, H. Shin, E. Kim, Flexible PEDOT electrodes with large thermoelectric power factors to generate electricity by the touch of fingertips. *Energy Environ. Sci.* **6**, 788–792 (2013). [doi:10.1039/c3ee23729j](https://doi.org/10.1039/c3ee23729j)
10. S. Kim, S. J. Choi, K. Zhao, H. Yang, G. Gobbi, S. Zhang, J. Li, Electrochemically driven mechanical energy harvesting. *Nat. Commun.* **7**, 10146 (2016).
[doi:10.1038/ncomms10146](https://doi.org/10.1038/ncomms10146) [Medline](#)
11. M. Aureli, C. Prince, M. Porfiri, S. D. Peterson, Energy harvesting from base excitation of ionic polymer metal composites in fluid environments. *Smart Mater. Struct.* **19**, 015003 (2010). [doi:10.1088/0964-1726/19/1/015003](https://doi.org/10.1088/0964-1726/19/1/015003)
12. T. Krupenkin, J. A. Taylor, Reverse electrowetting as a new approach to high-power energy harvesting. *Nat. Commun.* **2**, 448 (2011). [doi:10.1038/ncomms1454](https://doi.org/10.1038/ncomms1454) [Medline](#)
13. J. K. Moon, J. Jeong, D. Lee, H. K. Pak, Electrical power generation by mechanically modulating electrical double layers. *Nat. Commun.* **4**, 1487 (2013).
[doi:10.1038/ncomms2485](https://doi.org/10.1038/ncomms2485) [Medline](#)

14. R. Pelrine *et al.*, Dielectric elastomers: Generator mode fundamentals and applications. *Proc. SPIE* **4329**, 148 (2001).
15. S. Chiba, M. Waki, R. Kornbluh, R. Pelrine, Innovative power generators for energy harvesting using electroactive polymer artificial muscles. *Proc. SPIE* **2008**, 692715 (2008). [doi:10.1117/12.778345](https://doi.org/10.1117/12.778345)
16. T. Mirfakhrai, J. Y. Oh, M. Kozlov, S. L. Fang, M. Zhang, R. H. Baughman, J. D. Madden, Carbon nanotube yarns as high load actuators and sensors. *Adv. Sci. Tech.* **61**, 65–74 (2008). [doi:10.4028/www.scientific.net/AST.61.65](https://doi.org/10.4028/www.scientific.net/AST.61.65)
17. M. Zhang, K. R. Atkinson, R. H. Baughman, Multifunctional carbon nanotube yarns by downsizing an ancient technology. *Science* **306**, 1358–1361 (2004).
[doi:10.1126/science.1104276](https://doi.org/10.1126/science.1104276) [Medline](#)
18. M. Zhang, S. Fang, A. A. Zakhidov, S. B. Lee, A. E. Aliev, C. D. Williams, K. R. Atkinson, R. H. Baughman, Strong, transparent, multifunctional, carbon nanotube sheets. *Science* **309**, 1215–1219 (2005). [doi:10.1126/science.1115311](https://doi.org/10.1126/science.1115311) [Medline](#)
19. X. Lepró, R. Ovalle-Robles, M. D. Lima, A. L. Elías, M. Terrones, R. H. Baughman, Catalytic twist-spun yarns of nitrogen-doped carbon nanotubes. *Adv. Funct. Mater.* **22**, 1069–1075 (2012). [doi:10.1002/adfm.201102114](https://doi.org/10.1002/adfm.201102114)
20. S. Priya *et al.*, A review on piezoelectric energy harvesting: Materials, methods and circuits. *Energy Harvesting Syst.* **4**, 3–39 (2017).
21. M. D. Lima, S. Fang, X. Lepró, C. Lewis, R. Ovalle-Robles, J. Carretero-González, E. Castillo-Martínez, M. E. Kozlov, J. Oh, N. Rawat, C. S. Haines, M. H. Haque, V. Aare, S. Stoughton, A. A. Zakhidov, R. H. Baughman, Biscrolling nanotube sheets and functional guests into yarns. *Science* **331**, 51–55 (2011). [doi:10.1126/science.1195912](https://doi.org/10.1126/science.1195912) [Medline](#)
22. See supplementary materials.
23. M. D. Lima, N. Li, M. Jung de Andrade, S. Fang, J. Oh, G. M. Spinks, M. E. Kozlov, C. S. Haines, D. Suh, J. Foroughi, S. J. Kim, Y. Chen, T. Ware, M. K. Shin, L. D. Machado, A. F. Fonseca, J. D. W. Madden, W. E. Voit, D. S. Galvão, R. H. Baughman, Electrically, chemically, and photonically powered torsional and tensile actuation of hybrid carbon nanotube yarn muscles. *Science* **338**, 928–932 (2012). [doi:10.1126/science.1226762](https://doi.org/10.1126/science.1226762) [Medline](#)
24. C. S. Haines, M. D. Lima, N. Li, G. M. Spinks, J. Foroughi, J. D. W. Madden, S. H. Kim, S. Fang, M. Jung de Andrade, F. Göktepe, Ö. Göktepe, S. M. Mirvakili, S. Naficy, X. Lepró, J. Oh, M. E. Kozlov, S. J. Kim, X. Xu, B. J. Swedlove, G. G. Wallace, R. H. Baughman, Artificial muscles from fishing line and sewing thread. *Science* **343**, 868–872 (2014). [doi:10.1126/science.1246906](https://doi.org/10.1126/science.1246906) [Medline](#)
25. M. Kosmulski, pH-dependent surface charging and points of zero charge. IV. Update and new approach. *J. Colloid Interface Sci.* **337**, 439–448 (2009).
[doi:10.1016/j.jcis.2009.04.072](https://doi.org/10.1016/j.jcis.2009.04.072) [Medline](#)

26. L. H. Shao, J. Biener, D. Kramer, R. N. Viswanath, T. F. Baumann, A. V. Hamza, J. Weissmüller, Electrocapillary maximum and potential of zero charge of carbon aerogel. *Phys. Chem. Chem. Phys.* **12**, 7580–7587 (2010). [doi:10.1039/b916331j](https://doi.org/10.1039/b916331j) Medline
27. E. McCafferty, Relationship between the isoelectric point (pHpzc) and the potential of zero charge (Epzc) for passive metals. *Electrochim. Acta* **55**, 1630–1637 (2010). [doi:10.1016/j.electacta.2009.10.040](https://doi.org/10.1016/j.electacta.2009.10.040)
28. Y. Tanaka, Y. Hirana, Y. Niidome, K. Kato, S. Saito, N. Nakashima, Experimentally determined redox potentials of individual (n,m) single-walled carbon nanotubes. *Angew. Chem. Int. Ed.* **48**, 7655–7659 (2009). [doi:10.1002/anie.200902468](https://doi.org/10.1002/anie.200902468) Medline
29. J. P. Randin, E. Yeager, Differential capacitance study of stress/annealed pyrolytic graphite electrodes. *J. Electrochem. Soc.* **118**, 711–714 (1971). [doi:10.1149/1.2408151](https://doi.org/10.1149/1.2408151)
30. J. P. Randin, E. Yeager, Differential capacitance study on the basal plane of stress-annealed pyrolytic graphite. *J. Electroanal. Chem. Interfacial Electrochem.* **36**, 257–276 (1972). [doi:10.1016/S0022-0728\(72\)80249-3](https://doi.org/10.1016/S0022-0728(72)80249-3)
31. J. N. Barisci, G. G. Wallace, D. Chattopadhyay, F. Papadimitrakopoulos, R. H. Baughman, Electrochemical properties of single-wall carbon nanotube electrodes. *J. Electrochem. Soc.* **150**, E409–E415 (2003). [doi:10.1149/1.1593045](https://doi.org/10.1149/1.1593045)
32. J. Chmiola, G. Yushin, Y. Gogotsi, C. Portet, P. Simon, P. L. Taberna, Anomalous increase in carbon capacitance at pore sizes less than 1 nanometer. *Science* **313**, 1760–1763 (2006). [doi:10.1126/science.1132195](https://doi.org/10.1126/science.1132195) Medline
33. M. Motta, A. Moisala, I. A. Kinloch, A. H. Windle, High performance fibres from ‘dog bone’ carbon nanotubes. *Adv. Mater.* **19**, 3721–3726 (2007). [doi:10.1002/adma.200700516](https://doi.org/10.1002/adma.200700516)
34. M. F. Yu, M. J. Dyer, R. S. Ruoff, Structure and mechanical flexibility of carbon nanotube ribbons: An atomic-force microscopy study. *J. Appl. Phys.* **89**, 4554–4557 (2001). [doi:10.1063/1.1356437](https://doi.org/10.1063/1.1356437)
35. S. H. Kim, M. D. Lima, M. E. Kozlov, C. S. Haines, G. M. Spinks, S. Aziz, C. Choi, H. J. Sim, X. Wang, H. Lu, D. Qian, J. D. W. Madden, R. H. Baughman, S. J. Kim, Harvesting temperature fluctuations as electrical energy using torsional and tensile polymer muscles. *Energy Environ. Sci.* **8**, 3336–3344 (2015). [doi:10.1039/C5EE02219C](https://doi.org/10.1039/C5EE02219C)
36. Y. Zi, H. Guo, Z. Wen, M.-H. Yeh, C. Hu, Z. L. Wang, Harvesting low-frequency (<5 Hz) irregular mechanical energy: A possible killer application of triboelectric nanogenerator. *ACS Nano* **10**, 4797–4805 (2016). [doi:10.1021/acsnano.6b01569](https://doi.org/10.1021/acsnano.6b01569) Medline
37. C. S. Haines, N. Li, G. M. Spinks, A. E. Aliev, J. Di, R. H. Baughman, New twist on artificial muscles. *Proc. Natl. Acad. Sci. U.S.A.* **113**, 11709–11716 (2016). [doi:10.1073/pnas.1605273113](https://doi.org/10.1073/pnas.1605273113) Medline

38. W. R. Heinzelman, A. Chandrakasan, H. Balakrishnan, “Energy-efficient communication protocol for wireless microsensor networks,” in *Proceedings of the 33rd Hawaii International Conference on System Sciences* (IEEE, 2000), p. 8020.
39. G. Zhu, Y. S. Zhou, P. Bai, X. S. Meng, Q. Jing, J. Chen, Z. L. Wang, A shape-adaptive thin-film-based approach for 50% high-efficiency energy generation through micro-grating sliding electrification. *Adv. Mater.* **26**, 3788–3796 (2014). [doi:10.1002/adma.201400021](https://doi.org/10.1002/adma.201400021) [Medline](#)
40. N. Fujishiro, J. Hatae, H. Kawata, A program for calculation of the proton activity coefficient. *Comput. Biol. Med.* **24**, 221–228 (1994). [doi:10.1016/0010-4825\(94\)90018-3](https://doi.org/10.1016/0010-4825(94)90018-3) [Medline](#)
41. M. D. Lima, M. W. Hussain, G. M. Spinks, S. Naficy, D. Hagenasr, J. S. Bykova, D. Tolly, R. H. Baughman, Efficient, absorption-powered artificial muscles based on carbon nanotube hybrid yarns. *Small* **11**, 3113–3118 (2015). [doi:10.1002/smll.201500424](https://doi.org/10.1002/smll.201500424) [Medline](#)
42. P. Chen, Y. Xu, S. He, X. Sun, S. Pan, J. Deng, D. Chen, H. Peng, Hierarchically arranged helical fibre actuators driven by solvents and vapours. *Nat. Nanotechnol.* **10**, 1077–1083 (2015). [doi:10.1038/nnano.2015.198](https://doi.org/10.1038/nnano.2015.198) [Medline](#)
43. H. Ji, X. Zhao, Z. Qiao, J. Jung, Y. Zhu, Y. Lu, L. L. Zhang, A. H. MacDonald, R. S. Ruoff, Capacitance of carbon-based electrical double-layer capacitors. *Nat. Commun.* **5**, 3317 (2014). [doi:10.1038/ncomms4317](https://doi.org/10.1038/ncomms4317) [Medline](#)
44. R. Rado, Ed., *Chemical Transformations of Polymers* (Elsevier, 2013).
45. J. N. Israelachvili, *Intermolecular and Surface Forces* (Elsevier, ed. 3, 2011).
46. C. Laurent, E. Flahaut, A. Peigney, The weight and density of carbon nanotubes versus the number of walls and diameter. *Carbon* **48**, 2994–2996 (2010).
[doi:10.1016/j.carbon.2010.04.010](https://doi.org/10.1016/j.carbon.2010.04.010)
47. S. Y. Jeon, J. Jang, B. W. Koo, Y. W. Kim, W. R. Yu, A predictive model of the tensile strength of twisted carbon nanotube yarns. *Nanotechnology* **28**, 015703 (2017).
[doi:10.1088/0957-4484/28/1/015703](https://doi.org/10.1088/0957-4484/28/1/015703) [Medline](#)
48. T. C. O’Connor, J. Andzelm, M. O. Robbins, AIREBO-M: A reactive model for hydrocarbons at extreme pressures. *J. Chem. Phys.* **142**, 024903 (2015).
[doi:10.1063/1.4905549](https://doi.org/10.1063/1.4905549) [Medline](#)
49. S. Plimpton, Fast parallel algorithms for short-range molecular-dynamics. *J. Comput. Phys.* **117**, 1–19 (1995). [doi:10.1006/jcph.1995.1039](https://doi.org/10.1006/jcph.1995.1039)
50. G. T. Hwang, H. Park, J.-H. Lee, S. Oh, K.-I. Park, M. Byun, H. Park, G. Ahn, C. K. Jeong, K. No, H. Kwon, S.-G. Lee, B. Joung, K. J. Lee, Self-powered cardiac pacemaker enabled by flexible single crystalline PMN-PT piezoelectric energy harvester. *Adv. Mater.* **26**, 4880–4887 (2014). [doi:10.1002/adma.201400562](https://doi.org/10.1002/adma.201400562) [Medline](#)

51. W. Wu, L. Wang, Y. Li, F. Zhang, L. Lin, S. Niu, D. Chenet, X. Zhang, Y. Hao, T. F. Heinz, J. Hone, Z. L. Wang, Piezoelectricity of single-atomic-layer MoS₂ for energy conversion and piezotronics. *Nature* **514**, 470–474 (2014). [doi:10.1038/nature13792](https://doi.org/10.1038/nature13792) [Medline](#)
52. K. H. Cho, H. Y. Park, J. S. Heo, S. Priya, Structure-performance relationships for cantilever-type piezoelectric energy harvesters. *J. Appl. Phys.* **115**, 204108 (2014). [doi:10.1063/1.4879876](https://doi.org/10.1063/1.4879876)
53. <http://info.mide.com/piezo-products/download-piezo-products-datasheets>
54. www.piezo.com/catalog8.pdf%20files/Cat8.20&21.pdf
55. G. T. Hwang, V. Annapureddy, J. H. Han, D. J. Joe, C. Baek, D. Y. Park, D. H. Kim, J. H. Park, C. K. Jeong, K.-I. Park, J.-J. Choi, D. K. Kim, J. Ryu, K. J. Lee, Self-powered wireless sensor node enabled by an aerosol-deposited PZT flexible energy harvester. *Adv. Energy Mater.* **6**, 1600237 (2016). [doi:10.1002/aenm.201600237](https://doi.org/10.1002/aenm.201600237)
56. www.cornestech.co.jp/images/uploads/file/products/pdf/bolt.pdf
57. K. B. Kim, C.-I. Kim, Y. H. Jeong, Y.-J. Lee, J.-H. Cho, J.-H. Paik, S. Nahm, Performance of unimorph cantilever generator using Cr/Nb doped Pb(Zr_{0.54}Ti_{0.46})O₃ thick film for energy harvesting device applications. *J. Eur. Ceram. Soc.* **33**, 305–311 (2013). [doi:10.1016/j.jeurceramsoc.2012.09.001](https://doi.org/10.1016/j.jeurceramsoc.2012.09.001)
58. H. A. Sodano, G. Park, D. J. Inman, Estimation of electric charge output for piezoelectric energy harvesting. *Strain* **40**, 49–58 (2004). [doi:10.1111/j.1475-1305.2004.00120.x](https://doi.org/10.1111/j.1475-1305.2004.00120.x)
59. N. Sharpes, A. Abdelkefi, S. Priya, Two-dimensional concentrated-stress low-frequency piezoelectric vibration energy harvesters. *Appl. Phys. Lett.* **107**, 093901 (2015). [doi:10.1063/1.4929844](https://doi.org/10.1063/1.4929844)
60. C. K. Jeong, K. I. Park, J. Ryu, G. T. Hwang, K. J. Lee, Large-area and flexible lead-free nanocomposite generator using alkaline niobate particles and metal nanorod filler. *Adv. Funct. Mater.* **24**, 2620–2629 (2014). [doi:10.1002/adfm.201303484](https://doi.org/10.1002/adfm.201303484)
61. Y. Hu, C. Xu, Y. Zhang, L. Lin, R. L. Snyder, Z. L. Wang, A nanogenerator for energy harvesting from a rotating tire and its application as a self-powered pressure/speed sensor. *Adv. Mater.* **23**, 4068–4071 (2011). [doi:10.1002/adma.201102067](https://doi.org/10.1002/adma.201102067) [Medline](#)
62. S. Boisseau, G. Despesse, T. Ricart, E. Defay, A. Sylvestre, Cantilever-based electret energy harvesters. *Smart Mater. Struct.* **20**, 105013 (2011). [doi:10.1088/0964-1726/20/10/105013](https://doi.org/10.1088/0964-1726/20/10/105013)
63. G. Despesse *et al.*, Fabrication and characterization of high damping electrostatic micro devices for vibration energy scavenging. Proc. Design, Test, Integration and Packaging of MEMS and MOEMS, 386–390 (2005); <https://hal.archives-ouvertes.fr/hal-00748983>.
64. Y. Naruse, N. Matsubara, K. Mabuchi, M. Izumi, S. Suzuki, Electrostatic micro power generation from low-frequency vibration such as human motion. *J. Micromech. Microeng.* **19**, 094002 (2009). [doi:10.1088/0960-1317/19/9/094002](https://doi.org/10.1088/0960-1317/19/9/094002)

65. A. Crovetto, F. Wang, O. Hansen, Modeling and optimization of an electrostatic energy harvesting device. *J. Microelectromech. Syst.* **23**, 1141–1155 (2014). [doi:10.1109/JMEMS.2014.2306963](https://doi.org/10.1109/JMEMS.2014.2306963)
66. A. Crovetto, F. Wang, O. Hansen, An electret-based energy harvesting device with a wafer-level fabrication process. *J. Micromech. Microeng.* **23**, 114010 (2013). [doi:10.1088/0960-1317/23/11/114010](https://doi.org/10.1088/0960-1317/23/11/114010)
67. D. Kim, S.-B. Jeon, J. Y. Kim, M.-L. Seol, S. O. Kim, Y.-K. Choi, High-performance nanopattern triboelectric generator by block copolymer lithography. *Nano Energy* **12**, 331–338 (2015). [doi:10.1016/j.nanoen.2015.01.008](https://doi.org/10.1016/j.nanoen.2015.01.008)
68. W. S. Jung, M.-G. Kang, H. G. Moon, S.-H. Baek, S.-J. Yoon, Z.-L. Wang, S.-W. Kim, C.-Y. Kang, High output piezo/triboelectric hybrid generator. *Sci. Rep.* **5**, 9309 (2015). [doi:10.1038/srep09309](https://doi.org/10.1038/srep09309) [Medline](#)
69. F.-R. Fan, Z.-Q. Tian, Z. L. Wang, Flexible triboelectric generator. *Nano Energy* **1**, 328–334 (2012). [doi:10.1016/j.nanoen.2012.01.004](https://doi.org/10.1016/j.nanoen.2012.01.004)
70. P. Bai, G. Zhu, Z.-H. Lin, Q. Jing, J. Chen, G. Zhang, J. Ma, Z. L. Wang, Integrated multilayered triboelectric nanogenerator for harvesting biomechanical energy from human motions. *ACS Nano* **7**, 3713–3719 (2013). [doi:10.1021/nn4007708](https://doi.org/10.1021/nn4007708) [Medline](#)
71. J. W. Zhong, Q. Zhong, F. Fan, Y. Zhang, S. Wang, B. Hu, Z. L. Wang, J. Zhou, Finger typing driven triboelectric nanogenerator and its use for instantaneously lighting up LEDs. *Nano Energy* **2**, 491–497 (2013). [doi:10.1016/j.nanoen.2012.11.015](https://doi.org/10.1016/j.nanoen.2012.11.015)
72. C. Zhang, W. Tang, C. Han, F. Fan, Z. L. Wang, Theoretical comparison, equivalent transformation, and conjunction operations of electromagnetic induction generator and triboelectric nanogenerator for harvesting mechanical energy. *Adv. Mater.* **26**, 3580–3591 (2014). [doi:10.1002/adma.201400207](https://doi.org/10.1002/adma.201400207) [Medline](#)
73. J. S. Huang, S. Shian, Z. G. Suo, D. R. Clarke, Maximizing the energy density of dielectric elastomer generators using equi-biaxial loading. *Adv. Funct. Mater.* **23**, 5056–5061 (2013). [doi:10.1002/adfm.201300402](https://doi.org/10.1002/adfm.201300402)
74. S. Shian, J. Huang, S. Zhu, D. R. Clarke, Optimizing the electrical energy conversion cycle of dielectric elastomer generators. *Adv. Mater.* **26**, 6617–6621 (2014). [doi:10.1002/adma.201402291](https://doi.org/10.1002/adma.201402291) [Medline](#)
75. M. Waki, S. Chiba, R. Kombluh, R. Pelrine, U. Kunihiko, “Electric power from artificial muscles,” in *Proceedings of Oceans 2008 - MTS/IEEE Kobe Techno-Ocean* (IEEE, 2008), pp. 375–377.
76. T. Mckay, B. O’Brien, E. Calius, I. Anderson, An integrated, self-priming dielectric elastomer generator. *Appl. Phys. Lett.* **97**, 062911 (2010). [doi:10.1063/1.3478468](https://doi.org/10.1063/1.3478468)
77. C. Jean-Mistral, T. Vu Cong, A. Sylvestre, Advances for dielectric elastomer generators: Replacement of high voltage supply by electret. *Appl. Phys. Lett.* **101**, 162901 (2012). [doi:10.1063/1.4761949](https://doi.org/10.1063/1.4761949)

78. T. G. McKay, S. Rosset, I. A. Anderson, H. Shea, Dielectric elastomer generators that stack up. *Smart Mater. Struct.* **24**, 015014 (2015). [doi:10.1088/0964-1726/24/1/015014](https://doi.org/10.1088/0964-1726/24/1/015014)
79. T. Vu-Cong, C. Jean-Mistral, A. Sylvestre, Electrets substituting external bias voltage in dielectric elastomer generators: Application to human motion. *Smart Mater. Struct.* **22**, 025012 (2013). [doi:10.1088/0964-1726/22/2/025012](https://doi.org/10.1088/0964-1726/22/2/025012)